HAL
open science

Study of quarkonium production in ultra-relativistic nuclear collisions with ALICE at the LHC : and optimization of the muon identification algorithm

Gabriele Gaetano Fronze

To cite this version:

Gabriele Gaetano Fronze. Study of quarkonium production in ultra-relativistic nuclear collisions with ALICE at the LHC : and optimization of the muon identification algorithm. Nuclear Experiment [nucl-ex]. Ecole nationale supérieure Mines-Télécom Atlantique, 2019. English. NNT : 2019IMTA0132 . tel-02178802

HAL Id: tel-02178802

https://theses.hal.science/tel-02178802

Submitted on 10 Jul 2019

HAL is a multi-disciplinary open access archive for the deposit and dissemination of scientific research documents, whether they are published or not. The documents may come from teaching and research institutions in France or abroad, or from public or private research centers.

L'archive ouverte pluridisciplinaire **HAL**, est destinée au dépôt et à la diffusion de documents scientifiques de niveau recherche, publiés ou non, émanant des établissements d'enseignement et de recherche français ou étrangers, des laboratoires publics ou privés.

THESE DE DOCTORAT DE

L'ÉCOLE NATIONALE SUPERIEURE MINES-TELECOM ATLANTIQUE
BRETAGNE PAYS DE LA LOIRE - IMT ATLANTIQUE
COMUE UNIVERSITE BRETAGNE LOIRE
ECOLE DOCTORALE N° 596
Matière, Molécules, Matériaux
Spécialité : *Physique subatomique et instrumentation nucléaire*

en cotutelle avec

SCUOLA DI DOTTORATO "SCIENZE DELLA NATURA E TECNOLOGIE INNOVATIVE"
UNIVERSITÀ DEGLI STUDI DI TORINO
XXXI CICLO
Indirizzo in Fisica

Par
Gabriele Gaetano FRONZÉ

Study of quarkonium production in ultra-relativistic nuclear collisions with ALICE at the LHC
And optimization of the muon identification algorithm

Thèse présentée et soutenue à Torino (IT), le 29 Janvier 2019
Unité de recherche : Subatech IMT-Atlantique Nantes (F), INFN Torino (IT), CERN (CH)
Thèse Nº : 2019IMTA0132

Rapporteurs avant soutenance :

Giuseppe BRUNO	Professore Associato, Politecnico di Bari (IT)
Ruben SHAHOYAN	Senior Applied Physicist, CERN (CH)

Composition du Jury :

Président :	Giuseppe BRUNO	Professore associato, Politecnico di Bari (IT)
Examinateurs :	Ruben SHAHOYAN	Senior Applied Physicist, CERN (CH)
Dir. de thèse :	Gines MARTINEZ GARCIA	Directeur de Recherche, IMT-Atlantique, Université de Nantes
	Martino GAGLIARDI	Professore Associato, Università degli Studi di Torino

Invités :

Co-Encadrant :	Diego STOCCO	Chargé de Recherche, IMT-Atlantique, CNRS-IN2P3

Study of quarkonium production in ultra-relativistic nuclear collisions with ALICE at the LHC

and optimization of the muon identification algorithm

Gabriele Gaetano Fronzé

Supervisors: Prof. M. Gagliardi
Dr. G. Martinez

Co-supervisor: Dr. D. Stocco

Università degli Studi di Torino and IMT-Atlantique

Dottorato di Ricerca in fisica e Astrofisica - XXXI ciclo

June 2019

Declaration

I hereby declare that except where specific reference is made to the work of others, the contents of this dissertation are original and have not been submitted in whole or in part for consideration for any other degree or qualification in this, or any other university. This dissertation is my own work and contains nothing which is the outcome of work done in collaboration with others, except as specified in the text and Acknowledgements.

Gabriele Gaetano Fronzé
June 2019

Plan of the thesis

The thesis reported in the following is organized as follows :

1. In Chapter 1 an introduction to the Quark Gluon Plasma and to the expected suppression of quarkonia resonances in the deconfined medium will be given, along with a brief overview of previous results obtained by RHIC and LHC experiments. In addition, the ALICE experimental setup will be introduced, with particular regard to the muon spectrometer and the other detectors involved in the analysis.
2. In Chapter 2 a new framework for the study of ALICE muon trigger performances, developed as one of the subjects of this thesis, will be presented. The measurements obtained through the application of newly introduced algorithms will be presented and the status of the Resistive Plate Chambers composing the muon trigger system will be discussed.
3. In Chapter 3 the measurement of Υ suppression in Pb-Pb collisions at $\sqrt{s_{\mathrm{NN}}} = 5.02$ TeV will be presented, with a detailed description of the analysis procedures and the comparison with theoretical models.
4. In Chapter 4 an introduction to the Online-Offline (O^2) ALICE upgrade will be given. Subsequently, a new online processing algorithm for the muon trigger data will be presented and its performances discussed by by means of the results of several tests.
5. In Chapter 5 some conclusions on the work carried out in the thesis will be presented.

Résumé

ALICE est l'expérience au Large Hadron Collider de Genève dédiée à l'étude d'un état de la matière nucléaire dans lequel les quarks et les gluons ne sont plus confinés dans les hadrons, qui est appelé Quark Gluon Plasma (QGP). Pour bien comprendre le QGP il faut comprendre les caractéristiques de l'interaction nucléaire forte. Cette interaction fondamentale était formulée d'après les observations expérimentales en phénomènes de diffusion profondément inélastique dans lesquelles la collision entre le projectile et le nucléon cible montrait des particularités typiques d'une collision entre objets fondamentales. Cette observation était la première d'une série qui portait à la formulation de la Chromo Dynamique Quantique (QCD), une théorie formulée sur la base de l'Électro Dynamique Quantique (QED) mais avec bosons de médiation de l'interaction pas neutres. Le nombre quantique qui représente la charge associée à l'interaction nucléaire forte était appelé couleur. Les fermions de la théorie sont appelés quarks et présentent aussi une charge de couleur. Cette caractéristique, qui dérive du fait que la QCD n'est pas une théorie Abélienne, génère des termes d'auto-interaction dans l'Hamiltonienne des systèmes régis par la QCD. De cette manière la constante de couplage de l'interaction forte ne suit pas la même tendance de celle de la QED, mais, au contraire, sa valeur augmente avec la distance entre les particules colorées. La conséquence est que on ne peut pas observer des quarks ou gluons libres car, si on éloigne deux particules colorées les unes des autres, la création de nouvelles particules devient énergétiquement plus avantageuse que continuer à séparer les charges de couleur. Pour cette raison les quarks et les gluons sont confinés à l'intérieur de particules (dites hadrons) qui ont une charge totale de couleur nulle. Toutefois, quand deux noyaux lourds accélérés à énergies ultra relativistes entrent en collisions, la densité d'énergie du milieu produit est si haute que les quarks et les gluons se comportent comme s'ils étaient libres. Le milieu ainsi formé s'épand rapidement à cause de la forte pression et il se refroidisse. Le refroidissement a comme conséquence que les quarks et les gluons ne peuvent plus rester libres et commencent à se regrouper en hadrons en forme de mésons (composés par un quark et un anti-quark) et barions (composés par trois quarks). Les quarks lourds, comme les quarks charme ou beauté, sont produits lors de premiers instants de la collision et traversent le plasma pendant son évolution. Ces quarks peuvent se lier en mésons, dites quarkonium qui prennent le nom de charmonium si les

quarks liés sont des quarks charm ou bottomonium si quarks beauté. La formation de ces états liés est affectée par la présence du milieu. Notamment, la liaison peut être dissoute par un effet de réduction du potentiel d'interaction causée par la présence des charges de couleur libres (à la Debye). Le résultat est une réduction du nombre des états de quarkonium qui émergent du QGP. Cet effet dépend de la température du milieu et de l'énergie de liaison des différents états du quarkonium, et peut donc être utilisé comme thermomètre du QGP. Toutefois, aux énergies du LHC, un grand nombre de couples de quarks et anti-quarks lourds est produit dans la collision. Ceci donne lieu à un phénomène de régénération des quarkonia par recombinaison aléatoire des quarks d'un couple avec l'anti-quark d'un autre couple. Le phénomène est plus important pour les états de charmonium par rapport au bottomonium car le quark charme, plus léger, est plus abondante du quark beauté. Mon travail de thèse se focalise d'un côté sur l'analyse des données des collisions Pb-Pb et pp afin d'étudier les modifications de la production du méson Upsilon dans le canal de désintégration en deux muons. De l'autre côté, et avec l'objectif d'optimisation des résultats de l'analyse, un nouvel algorithme d'identification de muons était développé, pour se préparer à la troisième phase de prise des données d'ALICE, pendant lequel les spécifications de fonctionnement exigeront une reconstruction quasi en-ligne.

Un des résultats principals de cette thèse est la mesure des mésons Upsilon en collisions Pb-Pb collectées fin 2015. Le résultat principal était la mesure du facteur de modification nucléaire R_{AA}, défini comme le rapport entre le taux de production du méson Upsilon en collisions Pb-Pb divisé par la section efficace en collisions pp à la même énergie, normalisé par la fonction de recouvrement nucléaire. L'RAA nécessite en outre la mesure de la section efficace de production en collisions pp. Par contre, la statistique collectée en collisions pp à 5 TeV par ALICE n'était pas suffisante pour calculer la section efficace. Pour cette raison une interpolation des valeurs de section efficace mesurées par plusieurs expériences à de différentes énergies (2.76, 7 et 8 TeV) était nécessaire pour obtenir la valeur pour le calcul du facteur de modification nucléaire a 5.02 TeV. L'analyse de ces résultats permet d'observer la présence de suppression de production de Bottomonium par rapport à sa production en collisions proton-proton. En plus, la suppression augmente en passant des collisions plus périphériques à celles plus centrales. Aucune dépendance de la suppression de la rapidité ou de l'impulsion transverse de l'état du bottomonium était observée. La présence de régénération des états du bottomonium par quarks beauté libres dans le QGP était étudiée par la comparaison du R_{AA} avec des modelés théoriques comprenant ou pas des contributions de régénération. Toutefois, une conclusion claire sur la présence ou pas des phénomènes de régénération n'est pas possible avec les incertitudes actuelles.

Pendant mon travail de thèse, j'ai aussi contribué au monitorage de la performance du système de déclanchement du spectromètre à muons, notamment à travers le développement d'une suite de logiciels pour l'analyse des paramètres de fonctionnement des chambre RPCs. Ce système était développé sur la base de l'expérience acquise au début du doctorat et comprend un protocole de téléchargement et analyse des données très simple à utiliser. Cet aspect, avec la définition d'une manière pour décrire et pour créer automatiquement les histogrammes et les graphs nécessaires pour l'analyse, ira changer et rendre plus rapide l'étude de la condition opérative du système de déclenchement sur spectromètre à muons.

La dernière partie du travail the thèse porte sur le développement du système de trajectographie en ligne pour l'amèlioration du système de déclenchement du spectromètre à muon. Ce développement est nécessaire pour rendre ALICE capable de travailler avec les nouvelles conditions présentes dans les prochaines phases de récolte des donnés. En particulier le travail ici présenté concerne un set de logiciels indépendants qui peuvent masquer en ligne les canaux bruyants du système de déclanchement et, plus en général, calculer en ligne la fraction allumée du détecteur.

Table des matières

Table des figures **xiii**

Liste des tableaux **xxiii**

1 Introduction **1**

1.1 The physics of QGP 1

1.1.1 The strong interaction 1

1.1.2 Quark Gluon Plasma 4

1.1.3 Soft and hard probes 8

1.1.4 Centrality estimation : Glauber model 9

1.1.5 Nuclear modification factor 14

1.2 Bottomonium study 16

1.2.1 Rationale of bottomonium study 16

1.2.2 Previous results 19

1.3 The Large Hadron Collider 22

1.4 ALICE experimental setup 24

1.4.1 V0 and Zero Degree Calorimeters (ZDC) 25

1.4.2 Central barrel detectors 25

1.4.3 Muon spectrometer 31

2 Measurement and monitoring of Muon Trigger System performances **39**

2.1 History and main features of Resistive Plate Chambers 39

2.2 Ageing effects in RPC detectors 44

2.3 The ALICE muon trigger RPCs 46

2.4 MTR monitoring data sources 47

2.5 MTR integrated charge measurements 48

2.6 MTR performance analysis framework 50

2.7 Determination of dark current and dark rate and dark current interpolation procedure . . . 51
2.8 Performance analysis . . . 53
2.8.1 Dark current trend . . . 55
2.8.2 Net current and integrated charge trend . . . 56
2.8.3 Dark rate trend . . . 60
2.8.4 Correlations between rates and net current . . . 62
2.8.5 Chambers efficiency . . . 63

3 Study of bottomonium production in Pb-Pb collisions at $\sqrt{s_{NN}} = 5.02$TeV 69
3.1 Operational definition of nuclear modification factor . . . 69
3.2 Experimental apparatus and data sample . . . 69
3.3 Signal extraction . . . 70
3.4 Acceptance and efficiency correction . . . 73
3.5 Reference pp cross section . . . 75
3.6 Uncertainties . . . 80
3.7 Results . . . 84
3.8 Summary . . . 88

4 Development of a Muon Identification acquisition and reconstruction framework for ALICE RUN3 91
4.1 Motivation . . . 91
4.2 Common software efforts . . . 94
4.3 Data format . . . 96
4.4 Data Processing Layer . . . 99
4.5 Muon tagging algorithm . . . 100
4.6 From Muon TRigger to Muon IDentifier . . . 102
4.7 MID raw data format . . . 103
4.8 MID reconstruction pipeline . . . 106
4.9 MID reconstruction performances . . . 108
4.9.1 Cluster residuals . . . 108
4.9.2 Track residuals . . . 109
4.9.3 Tracking efficiency . . . 111
4.9.4 PID characterization . . . 112

5 Conclusions 117

Bibliographie **119**

Table des figures

1.1 Representation of the baryon decuplet (left) and octet (right) following the eightfold way approach for three kinds of quarks : up, down and strange. The horizontal levels represent the net strangeness number, while the diagonals (top left to bottom right) link baryons with the same electric charge. From [1] 2

1.2 Cartoon of a deep inelastic scattering process between a projectile of momentum k and $k'$and a parton of initial momentum p belonging to a nucleon of initial momentum P. The interaction is mediated through the exchange of a boson of momentum q. [source] 2

1.3 Plot of the running coupling constant of the strong interaction α_S. The band has been computed using the standard model and several experimental points, obtained measuring the coupling from different processes, are shown. . . . 3

1.4 Cartoon showing the main hadronic matter phases in a (T, μ_B) diagram. . . 4

1.5 Space-time evolution of the fireball originated from an heavy ion collision with (left) and without (right) QGP. 7

1.6 Schematic of the stages on a heavy ion collision surrounding the collision moment. At first (left side) the nuclei are relativistically contracted. After the collision (right side) the spectators proceed unperturbed while the participants generate a colour tube filled of free partons. 9

1.7 Woods-Saxon potential for Pb nucleus as the ratio of the $\rho(r)$ over ρ_0 as a function of the distance from the nucleus center (r). Displayed parameters are extensively described in paragraph 1.1.4 11

1.8 Schematic representation of the Optical Glauber Model geometry, with transverse (a) and longitudinal (b) views. From [2]. 12

1.9 Glauber Monte Carlo $Au-Au$ collision with impact parameter $b = 6$ fm seen in the trasverse plane (left) and along the beam axis (right). Nucleons area is equal to σ_{inel}^{NN}. From [2]. 13

1.10 A cartoon example of the correlation of the final state observable N_{ch} with Glauber calculated quantities (b, N_{part}). The plotted distribution and various values are illustrative and not actual measurements. From [2]. 14
1.11 Distribution of the sum of signal amplitudes from a centrality detector. The distribution is fitted with the NBD-Glauber fit shown as a red line. The centrality classes used in the analysis are indicated in the figure. The inset shows a zoom of the most peripheral region. From [3]. 15
1.12 Cartoon representation of the dissociation temperatures of several quarkonium states. The sequential suppression can provide information regarding the average kinetic energy of the formed QGP droplet, leading to a QGP thermometer. 17
1.13 J/ψ (red) and Υ(1S) (blue) nuclear modification factor as a function of y measured by ALICE in p-Pb collisions ($-4.46 < y < -2.96$ and $2.03 < y < 3.53$) at $\sqrt{s_{\mathrm{NN}}} = 5.02$ TeV. From [4] 18
1.14 Representation of possible feed-down patterns for bottomonium states as measured from BaBar collaboration and reported in [5]. The numbers refer to the masses as reported by the PDG. Splittings in the photon spectra for these cascades are due to the mass splittings in the intermediate states χ_{bJ} with J = 0, 1 or 2. From [5] 19
1.15 J/ψ nuclear modification factor measured by PHENIX (RHIC) at $\sqrt{s_{\mathrm{NN}}} =$ 200 GeV (open black) and by ALICE at the LHC at $\sqrt{s_{\mathrm{NN}}} = 2.76$ and 5.02 TeV (blue and red, respectively), as a function of the number of participant nucleons. The RHIC points appear systematically below ALICE ones for $< N_{part} >= 50$, indicating a much lower suppression at LHC in the most central collisions. The two ALICE series appear to be in agreement over the whole centrality spectrum despite a factor $\times 2$ in the center of mass energy. From [4] 20
1.16 Υ nuclear modification factor measured at the LHC by ALICE at $\sqrt{s_{\mathrm{NN}}} =$ 2.76 TeV. Two centrality bins are shown, referring to the quoted centrality distribution percentiles. From [6] 21
1.17 Υ(1S) nuclear modification factor as a function of $< N_{part} >$ (left) and y (right) measured by ALICE (red points, $2.5 < y < 4.0$) and CMS (blue points, $|y| < 2.4$) at $\sqrt{s_{\mathrm{NN}}} = 2.76$ TeV. From [6] 21
1.18 J/ψ (blue) and Υ(1S) (red) nuclear modification factor as a function of $< N_{part} >$ measured by ALICE at forward rapidity ($2.5 < y < 4.0$) at $\sqrt{s_{\mathrm{NN}}} =$ 2.76 TeV. From [6] 22

1.19 Schematic representation of the CERN accelerator complex. [source] 23
1.20 Schematic of ALICE detectors setup, with a maximised view of the innermost detectors. [source] 24
1.21 Schematic representation of the ZDC along the z-axis. The trasverse positions of the beam pipes, ZN and ZP are shown. From [7] 25
1.22 Schematic representation of one of the two V0 arrays ($V0_A$). 26
1.23 Schematic of the ALICE ITS. From [8] 27
1.24 Representation of the TPC with some details of the layout. From [9] 28
1.25 Schematic of the ALICE TRD with an highlight on the modular struture of the detector. [source] 28
1.26 Schematic of the ALICE TOF. A detector module is represented along with the support structure. From [10] 29
1.27 The HMPID layout. [source] 30
1.28 The PHOS layout (brown) along with the DCal detector arrays (blue and light blue). [source] 30
1.29 The EMCal layout. [source] 31
1.30 Schematic representation of ALICE with highlighted muon spectrometer components. [source] 32
1.31 Detailed reprensentation of the front absorber composition. 33
1.32 ALICE dipole magnet schematics. 34
1.33 Digital representation of the layout of the muon chambers and muon trigger system, shown in green. 35
1.34 Local Board segmentation of the ALICE Muon Trigger. 36

2.1 Spark chamber schematic with some details on the external trigger system and coincidence electronics.Extracted from [11] 40
2.2 Transition from an avalanche to a streamer in a gaseous detector. (a) creation of the initial avalanche due to ionization of the gas ; (b-c) acceleration of electrons due to the electric field ; (d) growth of the avalanche until the internal field compensated the applied field ; (e) recombination photons cause the production of additional electron-ion pairs which generate additional avalanches at the head of the ionized region ; (f) the process continues with the merging of avalanches and the growth of the streamer. 41
2.3 Schematic representation of an RPC structure from the side. 42
2.4 Current trend over time for single side oil coated and double oil coated RPCs. From [12]. 43

2.5 Resistivity trend over time for prototype ALICE RPCs. In the top panel a chamber provided with dry gas mixture is shown, while in the bottom panel the gas mixture is humidified. Different marker styles correspond to different testing positions. From [12]. 45
2.6 Grayed out ALICE with highlighted muon chambers and muon trigger chambers. 47
2.7 Cartoon representing the process of dark current readings flagging by combining OCDB and DCS data. The lines are represented on an arbitrary horizontal time axis. The first line represents the current readings stored in the DCS database. The frequency of those measurements is not fixed. The second line represents with boxes the duration of several runs. Gray boxes show physics runs, while the black box represents a run in nominal conditions without beam (cosmic run). The first line currents can be flagged either as i_{tot} if within a non-cosmic run or as i_{dark} otherwise. They are represented in the last two lines accordingly. 52
2.8 Cartoon representing the interpolation process. The green and blue points represent i_{tot} and i_{dark} readings, according to figure 2.7. The dashed vertical lines represent the projection on the time-axis of i_{tot} readings. The solid line connecting i_{dark} measurements represents the linear interpolation. The crossings between the i_{dark} interpolation curve and the vertical dashed lines, are the i_{dark} values attributed to i_{tot} measurements. Such values are highlighted with red crosses. 53
2.9 Average dark current trend computed with the described procedure using cosmic runs only. The trends are shown in four panels corresponding to the four detection planes (from top to bottom MT11, MT12, MT21, MT22). For improved readability for each plane only the maximum and minimum trends and the average plot are shown. Each point corresponds to a run. The y value is obtained via the average of all the RPCs dark currents, while the x value is the timestamp which corresponds to the end of run. 54
2.10 Dark current as a function of time for the FEERIC-equipped RPC. The FEERIC FEE has been installed in 2015, hence the first part of the plot refers to the same RPC equipped with the ADULT front-end. The dark current is measured during cosmic runs. 56

2.11 Net current trends for each RPC over the whole operation period. The trends are shown in four panels corresponding to the four detection planes (from top to bottom MT11, MT12, MT21, MT22). For each plane only the trends of the RPC with the maximum and minimum current are shown. Each point corresponds to a run. The y value is the difference between the average total and dark currents, while the x value is the timestamp which corresponds to the end of run. 57
2.12 Net current as a function of time for the FEERIC-equipped RPC. The dark current is measured during cosmic runs, while the total current is measured during physics runs. 58
2.13 Integrated net charge for each RPC as a function of time. The 72 trends are divided by plane (from top to bottom MT11, MT12, MT21, MT22). For each plane the average plot is shown. Each point corresponds to a run. 59
2.14 Integrated charge as a function of time for the FEERIC-equipped RPC. The y value is the integral of net current shown in 2.12. 60
2.15 Dark rates trends for each RPC over the whole operation period. The 72 trends are divided by plane (from top to bottom MT11, MT12, MT21, MT22). For each plane the average plot is shown. Each point corresponds to a run. The y value is the average rate during a given cosmic run, while the x value is the timestamp which corresponds to the end of run. 61
2.16 Dark rate trend for the FEERIC-equipped RPC. The y value is the average rate measured during a given run, while the x value is the timestamp which corresponds to the end of run. 63
2.17 Correlation plot between net current and average rate within a given run. The 72 correlation plots are divided by plane (from top to bottom MT11, MT12, MT21, MT22). Each point corresponds to a run. The y value is the average rate during a given run, while the x value is the average net current value measured during the run. 64
2.18 Average efficiency trend for MT11. Each point corresponds to a run. Bending and non bending planes are shown in black and red respectively. 65
2.19 Average efficiency trend for MT12. Each point corresponds to a run. Bending and non bending planes are shown in black and red respectively. 65
2.20 Average efficiency trend for MT21. Each point corresponds to a run. Bending and non bending planes are shown in black and red respectively. 66
2.21 Average efficiency trend for MT22. Each point corresponds to a run. Bending and non bending planes are shown in black and red respectively. 67

2.22 Efficiency trend for the FEERIC-equipped RPC. Each point corresponds to a run. Bending and non bending planes are shown in black and red respectively. 67

3.1 Dimuon invariant mass distribution (left) and combinatorial background subtracted distribution (right) in the mass region of bottomonium signals. Solid (dotted) lines correspond to signal (background) functions. The sum of the various functions is also shown as a solid line. 71

3.2 $A \times \varepsilon$ as a function of centrality (left), p_{T} (center), and y (right). The values have been computed using embedded Monte Carlo events. 74

3.3 Interpolation of reference σ_{pp} in p_{T} (top 4 graphs) and y (bottom 4 graphs) bins. The measured points are reported with an error bar that is the quadratic sum of the statistical and systematic uncertainties. 79

3.4 Scatter plot of muon pair candidates' p_{T} s for background candidates (left) and signal candidates (right). The cut at $p_{\mathrm{T}} = 2\mathrm{GeV/c}$ on both muons is represented as a red box. 81

3.5 Evolution of the N_{rec}/N_{gen} ratio versus run number (top). Different colors refer to different input distributions for $\Upsilon(1\mathrm{S})$ p_{T} and y values, represented with the same color code in the bottom panel. Please note that the systematic study as a function of rapidity adopts an inverted convention for rapidity values, with respect to that adopted in this thesis, hence rapidity values are quoted as negative. 82

3.6 On left panel the muon trigger response function as a function of y is shown. Trigger response is reweighted using Monte Carlo data (red) or real data (blue). Right panel shows the ratio of the two series as a function of y. . . . 83

3.7 On left panel the muon trigger $A \times \varepsilon$ as a function of y is shown. Trigger efficiency is evaluated as the standard Monte Carlo set (red) or the real one (blue). Right panel shows the ratio of the two series as a function of y. . . . 84

3.8 Inclusive $\Upsilon(1\mathrm{S})$ R_{AA} as a function of centrality (top), p_{T} (left) and y (right) at forward rapidity at $\sqrt{s_{\mathrm{NN}}} = 5.02$ TeV. The vertical error bars and the boxes represent the statistical and uncorrelated systematic uncertainties, respectively. The relative correlated uncertainty is shown as boxes at unity. . 86

3.9 Inclusive $\Upsilon(1\mathrm{S})$ R_{AA} compared to predictions from two transport models [13, 14] and one hydro-dynamical model [15] as a function of centrality (top), p_{T} (left) and y (right). See text for details on the models. While all models provide centrality dependence predictions, some of them do not provide p_{T} and/or y estimations. The plots report all the available information at the moment of writing. 89

4.1 Sketch of the conceptual structure of the O^2 framework. The detector electronics provides a continuous stream of raw data which is compressed, preprocessed and packed by the read-out logic. Partial information coming from different detectors and systems is aggregated. The full set of data is processed and reconstructed. Up to this step all the computation is performed synchronously. The processed data is then stored and retrieved later for the asynchronous reconstruction. From [16] 93

4.2 Software topology of the O^2 project. O^2 stands on several software, sets of libraries and tools. The green boxes represents the low level libraries which constitutes the basis of the software. Some of them are ZeroMQ as message passing protocol, CMake as project build and test manager, Geant4 as particles propagation engine. The orange boxes represents ALFA, developed between ALICE and FAIR. This tool contains a set of high level tools, such as data transportation routines and the dynamic deployment system for the dynamic devices management. The blue box represents FairROOT, an evolution of ROOT focused on improved usability for the end-users. It allows for easy data visualization, storage, offline analysis and more. The ALICE O^2 stands on all these elements alongside other collaborations software (Panda, Cbm). From [16] 95

4.3 Sketch representing the acquisition flow with two detectors, A and B. The detector data samples are retrieved by the read-out logic in a continuous fashion, with the addition of heartbeat triggers interleaving for time stamping purposes. At the FLP level each data stream is time sliced, obtaining several patches which are compressed by fast processing and packed in sub TFs. The sub TFs are sent to the EPN farm and then aggregated into global TFs. Each TF has a full set of information regarding a given time interval. A global compression of around $\times 14$ is achieved in the process. From [16] 97

4.4 Computing infrastructure layers with quoted required input and output bandwidths. An overall factor of compression of ≈ 14 is to be achieved in the process. The network topology is not yet defined by the O^2 Technical Design Report since the technology growth is fast enough to require a shorter term planning later during the upgrade. From [16] 98

4.5 In this picture the muon chamber and muon trigger planes are represented in yellow, the iron wall in purple and the dipole is shown in blue. The dashed line represents the true trajectory of the muon. The green line is the reconstructed track within the muon chambers, while the orange line is the tracklet reconstructed in the muon trigger. 101
4.6 The MTR planes are shown in grey, while the hit local board is highlighted in yellow. Two real trajectories are represented by the lines. The algorithm is tuned to select the less sloped track in case of ambiguity, hence only the solid blue track would be recorded. 102
4.7 Detailed sketch of a generic Common Readout Unit (CRU). The Front End Electronics (FEE) are connected to the CRU through 24 embedded GBT links. The green boxes are connected to the Central trigger Processor (CTP) and deliver timing information to time tag the raw data flow, performed by the detector specific logic. The raw data is translated in a binary format which can be processed by the FLP CPUs. The ouput of the CRU is performed by a standard PCI Express link. From [16] 104
4.8 Two CRU data format proposals. In the first option only one non bending pattern is sent from the CRU to the FLP, while the FEE sends to the CRU several copies of the same pattern since the horizontal strips are read by several local boards each. The CRU has to perform some operation in order to combine the multiple non bending plane patterns into a single one. The second format foresees to send to the FLP several non bending plane patterns, which are combined by the FLP itself. 105
4.9 Schema of the MID reconstruction workflow obtained from the DPL Graphic User Interface (GUI). This workflow is intended to be executed in the FLP. Each box represents a device and the arrows represent a data stream. The first device, called ColDataStreamer, is a random generator of fake CRU messages able to emulate the CRU behaviour for testing purposes. The upper branch represents the asynchronous mask computing stage of the workflow. The last device, called sink, represents the connection to the EPN nodes and the second online processing step. 107

4.10 Cluster residuals distribution as a function of the RPC ID. The y bins are continuous values, while each x axis bin represents a single RPC. The square shaped artifacts are related to the different strip pitches each RPC is equipped with. The RPCs equipped with strips down to 1 cm wide present the hot spots due to the superposition of the residuals distributions of 1, 2 and 4 cm wide strips. The y distribution presents smaller structures since the average strip size is smaller. Each RPC distribution is not normalized on its irradiation hence the colour palette is the same for all the RPCs. 110
4.11 Track residuals distribution of the horizontal coordinate. The y axis represents the residual expressed in centimeters, while the x axis is the generated momentum of the particle. The colour palette is in logarithmic scale. The core of the distribution is about 1 cm wide and very few outliers cross the ± 2 cm band. 111
4.12 Track residuals distribution of the vertical coordinate. The y axis represents the residual expressed in centimeters, while the x axis is the reconstructed momentum of the particle. The colour palette is in logarithmic scale. The core of the distribution is about 0.5 cm wide and like for the horizontal coordinate, very few outliers cross the ± 2 cm band. 112
4.13 Residuals of the vertical and horizontal slopes evaluation between the old MTR's algorithm and the new MID's one. The values are represented as residuals (y) divided by sigma as a function of the reconstructed particle momentum. The colour pallette is represented in logarithmic scale. 114
4.14 Tracking efficiency computed as the ratio between the numbers of reconstructed and generated tracks. 115

Liste des tableaux

3.1 Reference cross sections and corresponding uncertainties in different p_{T} intervals. $\sigma_{pp}^{\Upsilon\to\mu^+\mu^-}$ values and uncertainties as obtained using LHCb pp data at $\sqrt{s_{pp}} = 2.76$ TeV. 75

3.2 Reference cross sections and corresponding uncertainties in different p_{T} intervals. $\sigma_{pp}^{\Upsilon\to\mu^+\mu^-}$ values and uncertainties as obtained using LHCb pp data at $\sqrt{s_{pp}} = 7$ TeV. 76

3.3 Reference cross sections and corresponding uncertainties in different p_{T} intervals. $\sigma_{pp}^{\Upsilon\to\mu^+\mu^-}$ values and uncertainties as obtained using LHCb pp data at $\sqrt{s_{pp}} = 8$ TeV. 76

3.4 y bins $d(\sigma_{pp}^{\Upsilon\to\mu^+\mu^-})/dy$ values and uncertainties as obtained using LHCb pp data at $\sqrt{s_{pp}} = 2{,}76$ TeV. 76

3.5 y bins $d(\sigma_{pp}^{\Upsilon\to\mu^+\mu^-})/dy$ values and uncertainties as obtained using LHCb pp data at $\sqrt{s_{pp}} = 7$ TeV. 77

3.6 y bins $d(\sigma_{pp}^{\Upsilon\to\mu^+\mu^-})/dy$ values and uncertainties as obtained using LHCb pp data at $\sqrt{s_{pp}} = 8$ TeV. 77

3.7 y bins $d(\sigma_{pp}^{\Upsilon\to\mu^+\mu^-})/dy$ values and uncertainties as obtained using ALICE pp data at $\sqrt{s_{pp}} = 7$ TeV. 77

3.8 y bins $d(\sigma_{pp}^{\Upsilon\to\mu^+\mu^-})/dy$ values and uncertainties as obtained using ALICE pp data at $\sqrt{s_{pp}} = 8$ TeV. 78

3.9 The interpolated branching ratio times cross section of Υ(1S) for the p_{T} and y bins under study. 80

3.10 Summary of the systematic uncertainties for R_{AA} calculation. Type I (II) refers to correlated (uncorrelated) systematic uncertainties. 85

Chapitre 1

Introduction

1.1 The physics of QGP

1.1.1 The strong interaction

Since the discovery of atomic nuclei and their apparently smallest constituents, at least two topics have been deeply discussed by physicists for decades : are such particles fundamental (and if not how are they formed) and how do they interact ? The first big jump ahead towards the answer was performed in 1961 independently by Gell-Mann and Ne'eman with the eight-fold theory, later developed further as the baryons octet and hyperions decuplet, represented in figure1.1. The organization of the particles was related to a symmetry group called $SU(3)$ which provides a triplet fundamental representation not observed in nature. This hint, combined with the speculation that 8 or 10 particles were not likely all fundamental, lead to the introduction of more fundamental particles.

They were later called quarks by Gell-Mann. At a given point Gell-Mann and Zweig argued that, assuming the quarks spin to be $1/2$, mesons could be explained as bound states of a quark and an antiquark, while baryons were a bound state of three quarks. This choice lead to the peculiar electric charge of $\pm 1/3$ and $\pm 2/3$. A last issue regarded the spin statistics theorem violation, solved by the introduction of an additional quantum number : the colour. This was the birth of the quark model. By assuming the hadronic matter is not fundamentally made of protons and neutrons they were able to organize in an elegant way the zoo of particles discovered during the 20th century.

During the same years, Richard Feynman started thinking about a model useful for analyzing the hadrons produced in high energy physics experiments and capable of interpreting the radiation showers originating in ultra-relativistic collisions. By introducing the partons and the parton distribution functions, Feynman was able to interpret the deep inelastic scattering

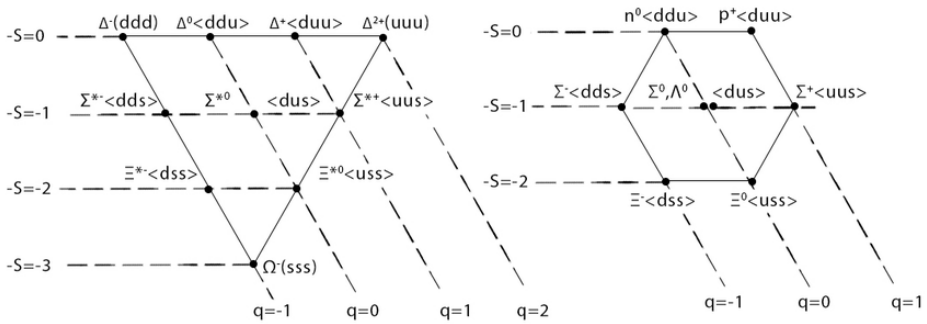

FIGURE 1.1 Representation of the baryon decuplet (left) and octet (right) following the eightfold way approach for three kinds of quarks : up, down and strange. The horizontal levels represent the net strangeness number, while the diagonals (top left to bottom right) link baryons with the same electric charge. From [1]

on hadrons as the collision between the projectile and an inner constituent of the target, called parton (see Fig.1.2).

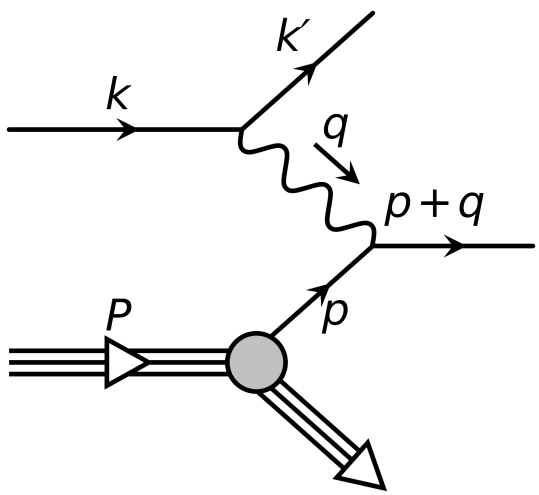

FIGURE 1.2 Cartoon of a deep inelastic scattering process between a projectile of momentum k and $k'$and a parton of initial momentum p belonging to a nucleon of initial momentum P. The interaction is mediated through the exchange of a boson of momentum q. [source]

Experiments of deep inelastic scattering performed at the Stanford Linear Accelerator Center (SLAC) between 1967 and 1973 pointed out a scaling behaviour, explained by Bjorken and Feynman as a signature of the point like constituents of the proton. Bjorken demonstrated

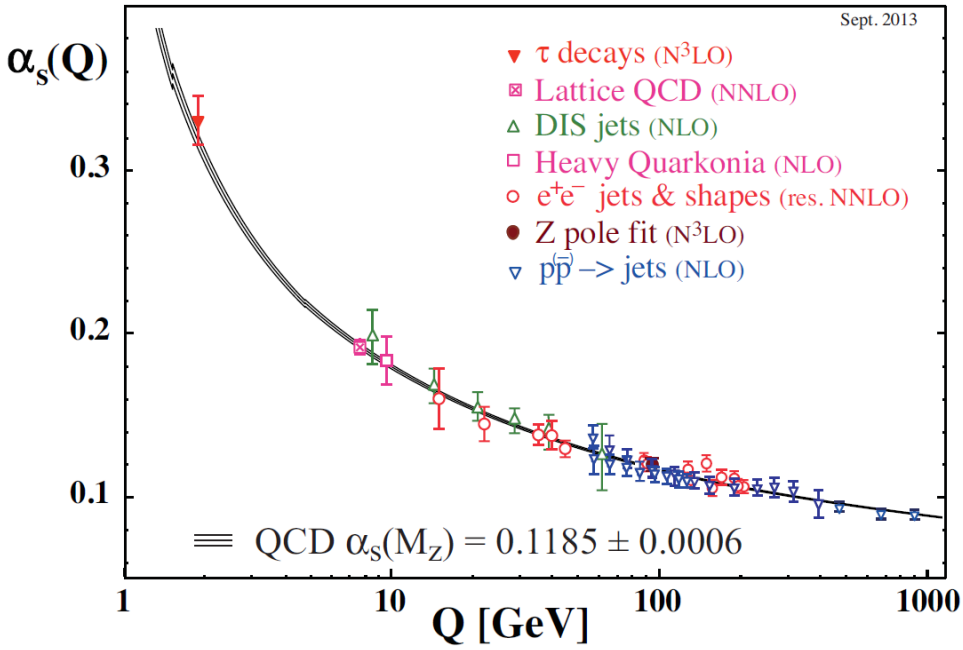

FIGURE 1.3 Plot of the running coupling constant of the strong interaction α_S. The band has been computed using the standard model and several experimental points, obtained measuring the coupling from different processes, are shown.
[source]

that the functions F_2 which describes the structure of the nucleon neither depend on the transferred momentum (Q^2) nor on the energy transferred in the scattering (ν), but on their ratio [1] :

$$x = \frac{Q^2}{2 \cdot M \cdot \nu} \tag{1.1}$$

where M is the mass of the target. The x variable has no dimension and stands for the ratio between the fraction of the 4-momentum that is transported by the point-like constituent and the total 4-momentum of the target.

After few other proofs the Gell-Mann quarks and the Feynman partons turned out to be the same objects. The answer to the first question was then well established (how are hadrons made ?) when the physics community started tackling the second one regarding how do they interact. The peculiarity of the new set of particles was the introduction of colour quantum number. In 1973, in analogy with the Quantum Electro Dynamics (QED),

1. The observed scaling was a peculiarity of the explored x range ($0.2 < x < 0.3$), since at higher and lower x ranges the scaling is violated by a dependence of F_2 from the transferred momentum Q^2.

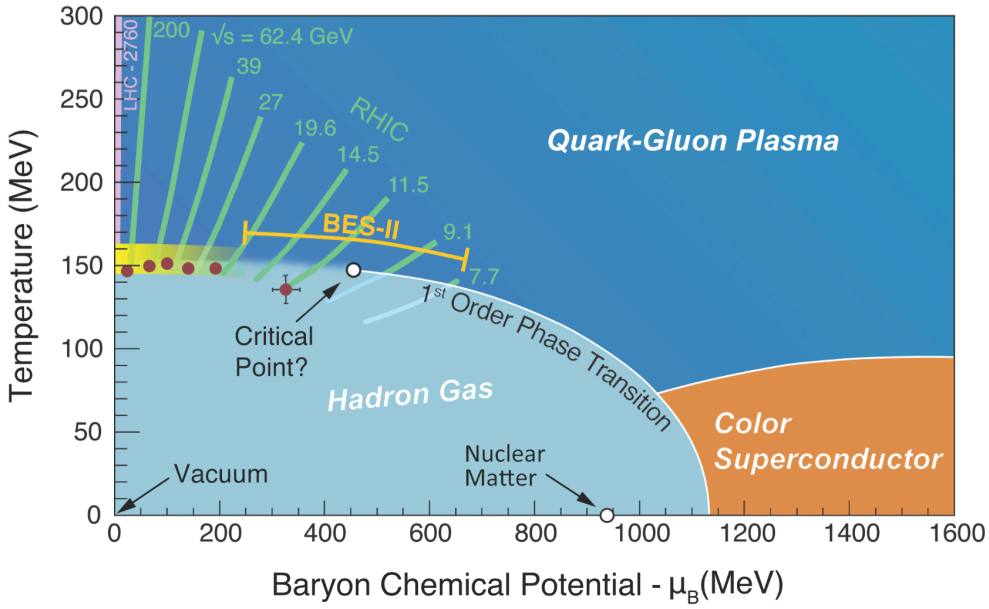

FIGURE 1.4 Cartoon showing the main hadronic matter phases in a (T, μ_B) diagram.

[source]

the Quantum Chromo Dynamics (QCD) was proposed as the quantum field theory of the hadronic interaction. The theory was supposed to be based on the existence of three colour charges and the non-Abelian simmetry group SU(3). Eight massless bosons, generators of the Lie symmetry group of the strong interaction, represented the mediators of such interaction and were later called gluons.

The gluons are different with respect to the photons, since, as an effect of the non Abelianness of the theory, they carry a colour charge, making them self-interacting. The coupling constant of the strong interaction is defined as running, since it depends on the value of the transferred momentum Q^2 as shown in Fig.1.3. In particular the lower the Q^2 values the higher the coupling constant. As a result, the strength of the interaction increases with distance. This property leads to the confinement of quarks and gluons inside hadrons. As a result the hadrons can only be found or produced in a colour singlet state and isolated quarks cannot be observed.

1.1.2 Quark Gluon Plasma

In 1975 N. Cabibbo and A. Parisi [17] suggested a state of nuclear matter in which quarks and gluons are not confined anymore into hadrons to explain the exponentially increasing spectrum proposed by Hagedorn [18]. This new state of matter was later called Quark Gluon

Plasma (QGP). From theoretical studies the main parameters determining the QGP evolution are the temperature (T) and the baryon-chemical potential (μ_B), defined in a thermodynamical fashion as the derivative of entropy with respect to the net baryon number. Three main regions are spotted in the (T, μ_B) phase diagram represented in Fig.1.4 :

— At low T and low μ_B the nuclear matter is composed of hadrons behaving as a hadron gas ;

— At low T and high μ_B, according to the latest theoretical developments, quark matter should enter a phase other than QGP, analogous to the superconducting phase of solid-state physics [19] ;

— At high T the strongly interacting matter can be described as a system of deconfined partons. Such behaviour is caused by the asymptotic freedom of QCD.

According to the Big Bang model the conditions of high temperature and low baryon-chemical potential are supposed to be the ones of the early Universe. At the beginning of the Universe all the energy and matter were condensed in a tiny spatial region. Then, during the first microseconds of evolution, the Universe started expanding from a condition of extreme energy density and temperature. Indeed the extreme conditions needed for the QGP production are similar to the ones happened at the beginning of the Universe evolution and can be reproduced in laboratory by means of ultra-relativistic heavy ion collisions.

While expanding, the energy density and the temperature started dropping. Two transitions happened at $T \simeq 160$ MeV and $T \simeq 100$ KeV [20] : the hadron formation started at the first threshold, while small nuclei could survive after the second value [21]. The nuclear composition of early Universe was fixed at that point : such phenomenon is called primordial nucleo-synthesis. Only few minutes later, when the Universe temperature dropped below 1 MeV, the radiation decoupled from matter and the whole Universe started becoming transparent. The Cosmic Microwave Background (CMB) is the residual of the first radiation.

Studying the QGP evolution and its characteristics might lead to a better understanding not only of the strong nuclear interaction and the origin of hadron masses, but also of the process of Universe formation.

One of the most common phenomenological models which can be cited to describe the transition to QGP is the MIT bag model [22, 23]. The two main hypotheses of this model are :

— the quarks are massless particles put inside a bag of finite dimension ;

— the confinement originates from the balancing of the internal pressure exerted by quarks into the bag and an external pressure B ;

The total energy of N quarks confined in a spherical volume of radius R is the sum of a kinetic term and a term related to the compensation by the external pressure B :

$$E = \frac{2.04 \cdot N}{R} \cdot \hbar c + \frac{4\pi}{3} \cdot R^3 \cdot B \tag{1.2}$$

The bag radius is determined by finding the minimum of energy of the system. Such condition is obtained imposing the condition $dE/dR = 0$.

$$\frac{dE}{dR} = -\frac{2.04 \cdot N}{R^2} \cdot \hbar c + 4\pi \cdot R^2 \cdot B = 0 \tag{1.3}$$

The model allows one to compute confinement thresholds for various systems. For example, for a baryon, composed by $N = 3$ quarks and with $R = 0.8$ fm the external pressure becomes :

$$B^{1/4} = \frac{206 \text{ MeV}}{\hbar c} \tag{1.4}$$

Such value is the limit below which the confinement of the quarks inside the baryon happens. With the growth of the internal pressure, the quarks behaviour gradually changes to an asymptotically free one. The internal pressure can increase in two ways :

— The increase of temperature causes an increase of kinetic energy of quarks inside the bag. In this situation the formed QGP is called "hot" ;

— The increase of pressure is caused by the increase of baryon density achieved via compression. This scenario is possible in extremely dense objects such as neutron stars and is defined as "cold" QGP.

The bag model provides an estimation of the minimum temperature and energy density needed to produce the deconfined state.

The pressure required to produce a QGP out of a volume V filled with massless quarks and gluons in which the net baryon number is null (equal number of quarks and anti-quarks) is computed as :

$$P = g_{tot} \cdot \frac{\pi^2}{90} \cdot T^4 \tag{1.5}$$

Where g_{tot} is the total number of degrees of freedom for quarks, anti-quarks and gluons. The pressure exceeds the external one at a temperature of around 145 MeV, a value similar to the lattice-QCD prediction of 160 MeV [20]. In addition, since the energy density is related to the pressure value, it can be computed as well :

$$\varepsilon = 3 \cdot P = g_{tot} \cdot \frac{\pi^2}{30} \cdot (160 \text{ MeV})^4 \simeq 1 \text{ GeV/fm}^3 \tag{1.6}$$

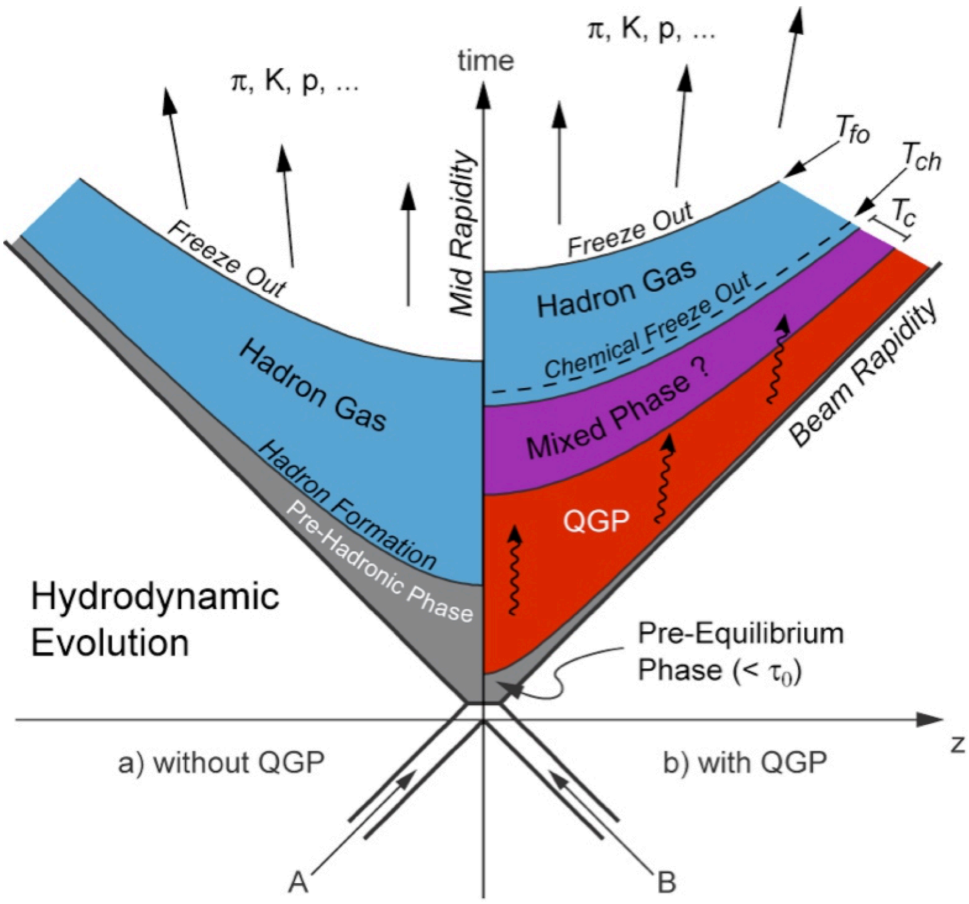

FIGURE 1.5 Space-time evolution of the fireball originated from an heavy ion collision with (left) and without (right) QGP.
[source]

Which is considered to be the threshold value to produce a deconfined medium.

The heavy-ion collision experiments tackle the QGP production through the approach based on reaching an extreme temperature, thanks to the high energy available in the center of mass of the collision. The collision process is characterized by a complex space and time evolution, but can be divided in some macro-conditions which can help understanding the whole process (see Fig. 1.5) :

— at $t = 0$ the collisions process starts ;

— Right after the collision the system crosses a pre-equilibrium phase. During this phase the medium is not yet thermalized and is governed by hard and semi-hard QCD processes ;

— The central "fireball" starts expanding following pressure gradients. The partons act as deconfined during this phase. The conservation of energy causes the temperature to drop depending on the fireball expansion ;
— The chemical freeze-out happens when the average temperature drops below a threshold which at LHC amounts to $\simeq$ 160 MeV [20]. The energy of the interactions does not allow to modify the abundances of hadrons ;
— The thermal freeze-out corresponds to the moment in which the elastic interactions between hadrons stop. At this point the kinematic spectra of the produced hadrons is fixed. The threshold temperature for this situation was deduced to be around 120 MeV [24].

The QGP phase lasts for about 10 fm/c and a direct observation is impossible. However, after the thermal freeze-out the hadrons fly freely and they can be detected by the experiment. Since the emerging hadrons had been influenced by the interaction with the QGP, or even produced inside it, they carry valuable information on its properties.

1.1.3 Soft and hard probes

The particles produced in a nuclear collision might be distinguished in soft and hard probes. Soft probes are produced during the evolution of the system formed in the collision and are related to the collective behaviour of the medium. The processes involving a soft probe production are characterized by low transferred momentum and for this reason most part of the produced particles are soft probes. Some observables related to soft probes are :

— Particle multiplicity : the multiplicity of particles produced is important for the determi- nation of the energy density of the collision and the study of their transverse momentum spectra allows to obtain information on the chemical and thermal freeze-out ;
— Collective flow : the spatial anisotropy of the colliding region induces pressure gradients which cause anisotropic particle distributions. This effect can be explained as a collective motion of particles produced in the interaction and its study is closely related to the determination of the equation of state for a deconfined medium ;
— the study of real and virtual photons (electromagnetic probes) is important for the determination of the medium temperature.

By contrast to soft probes, hard probes are particles produced in high transferred momentum processes and they are characterized by much lower production cross section. Hard probes are produced early during the collision and experience the full evolution of the system, in particular the early stage of the deconfined medium. Some observables related to hard probes are :

— Jet quenching : jets are produced by the fragmentation of high momentum partons. Interacting with a deconfined medium they can lose energy scattering with other free partons or through radiative gluon emission. The result is a quenched particle spectrum ;
— Open heavy flavour : particles with valence heavy quarks (charm or bottom) content are very important in the study of the QGP. Heavy quarks are produced in the initial stages of the collisions and experience the full evolution of the fireball. They lose energy in the interaction with the medium, and this results in a modification of the differential spectra. Moreover, the study of heavy flavours at low pt provides information on the thermalisation process of the medium ;
— Quarkonia production modification : the term quarkonium indicates a bound state of two heavy quarks and it is named charmonium when formed by charm quarks, bottomomium when formed by bottom quarks. These mesons are strongly affected by the formation of a partonic medium and this effect can result in a suppression due to a mechanism of color screening.

The measurement of bottomonium production is a main subject of this thesis. Similarly to other probes of the system, it can be studied as a function of the centrality of the collision, which allows to access additional information regarding the dependence of the probe production from the energy density.

1.1.4 Centrality estimation : Glauber model

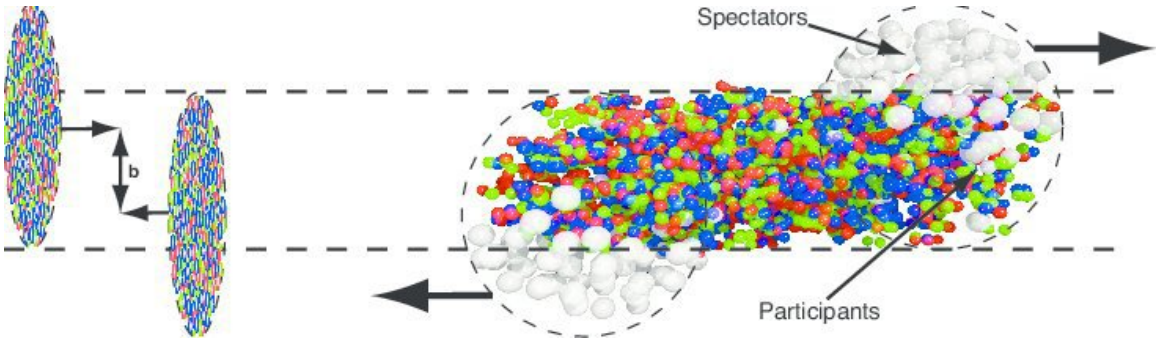

FIGURE 1.6 Schematic of the stages on a heavy ion collision surrounding the collision moment. At first (left side) the nuclei are relativistically contracted. After the collision (right side) the spectators proceed unperturbed while the participants generate a colour tube filled of free partons.

In the centre of mass system of the collision, the nuclei are Lorentz-contracted as shown in figure 1.6. Nuclei are composed by nucleons. The number of nucleons interacting during the collision depends on the impact parameter, which is defined as the spatial separation between the centroids of the two nuclei and determines the number of nucleons participating to the interaction. The measurement of the impact parameter is fundamental to know the nature of the initial collision state. The Glauber model, named after Roy Glauber, is usually used to model and analyze the geometry of a nuclear collision. The model stands on three basic assumptions :

— At high energy the nucleons are undeflected thanks to the large momentum, hence their trajectory is asymptotically linear ;
— Nuclear size has to be large compared to the range of nucleon-nucleon interaction ;
— Nucleons motion is independent from the nucleus one, hence the nuclear collision can be described in terms of the nucleon-nucleon cross section.

For doing so two inputs are necessary :

— Inelastic nucleon-nucleon cross section. This value should be measured at the same center-of-mass energy. It can be measured in proton-proton collisions ;
— Nucleus density profile. It is necessary to provide a contour shape for the colliding nuclei. Historically the nucleus profile has been modeled in the shell model approach as a Woods-Saxon distribution, which models the average nucleon potential in the nucleus. The potential shape corresponds to the nucleons distribution. The modified Woods-Saxon distribution, also called 2-parameter Fermi distribution, is :

$$\rho(r) = \frac{\rho_0 \cdot (1 + \omega r^2/R^2)}{1 + \exp(\frac{r-R}{a})} \tag{1.7}$$

where :

— r is the radial position at which one wants to compute the nucleons density ;
— ρ_0 is the normalization factor needed to provide the correct density value at $r = 0$;
— ω is a parameter which can represent a density bump right before the distribution tail ;
— R is the radius at which $\rho/\rho_0 = \frac{1+\omega}{2}$, similar to a half-width half maximum if $\omega = 0$;
— a describes the steepness of the distribution's tail.

The Woods-Saxon distribution parameters are typically determined via e^--nucleus scattering processes. The differences between protons and neutrons are assumed to be negligible. In figure 1.7 the distribution for a Pb nucleus is shown.

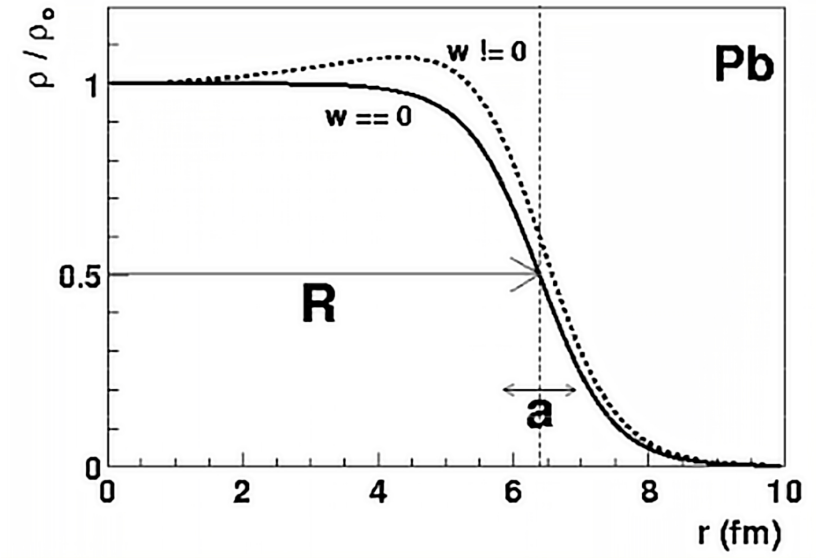

FIGURE 1.7 Woods-Saxon potential for *Pb* nucleus as the ratio of the $\rho(r)$ over ρ_0 as a function of the distance from the nucleus center (r). Displayed parameters are extensively described in paragraph 1.1.4

The Glauber model uses an optical and geometric approach to represent the nuclear collision. Referring to figure 1.8 :

— b is the distance between the centers of the colliding nuclei, namely the impact parameter;

— s is the distance of a nucleon flux tube relative to the nucleus center.

Note that in this discussion the vectors $\vec{b}$ and $\vec{s}$ will be replaced by their modulus. This can be done if the colliding particles are not polarized or present a spherical distribution of probability for the nucleon density. This assumption is legitimate for Pb nuclei.

The probability of finding a nucleon in a nucleon flux tube positioned at s from target A is defined as :

$$\hat{T}_A(s) = \int \rho_A(s, z_A) dz_a \tag{1.8}$$

The same equation can be rephrased to compute the same probability for the projectile. The effective overlap area of two specific nucleons can be described as :

$$\hat{T}_{AB}(b) = \int \hat{T}_A(s)\hat{T}_B(s-b)d^2s \tag{1.9}$$

in which the definition introduced in 1.8 is extensively adopted. $\hat{T}_{AB}(\vec{b})$ dimension is an inverse area.

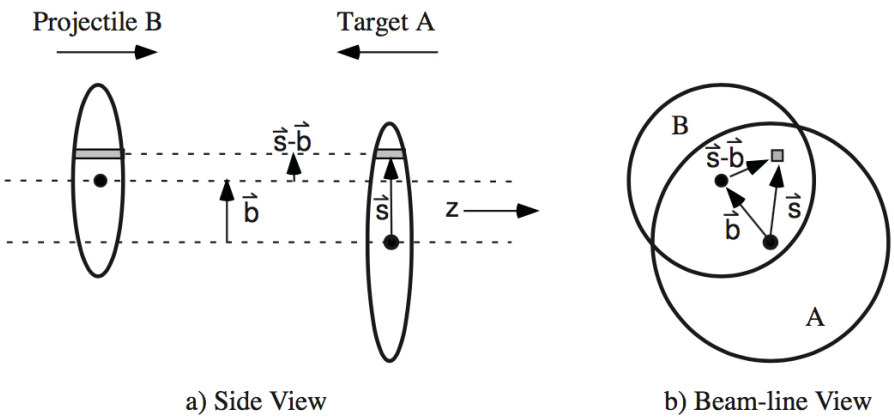

FIGURE 1.8 Schematic representation of the Optical Glauber Model geometry, with transverse (a) and longitudinal (b) views. From [2].

The probability of inelastic interaction between two specific nucleons belonging to A and B respectively can be described by :

$$P_{AB}(b) = \hat{T}_{AB}(b)\sigma_{inel}^{NN} \tag{1.10}$$

This interaction probability has to be reworked in order to reproduce the probability of having n binary collisions with $A+B$ colliding nucleons distributed in two different nuclei. Using a binomial distribution of probability one obtains :

$$P(n,b) = \binom{AB}{n}[P_{AB}(b)]^n[1-P_{AB}(b)]^{AB-n} \tag{1.11}$$

where AB is the product of the number of nucleons and n in the number of desired nucleon-nucleon collisions.

Using equation 1.11 one can compute $N_{coll}(\vec{b})$ (number of nucleon-nucleon collisions), $N_{part}(\vec{b})$ (number of participant nucleons) and $N_{spec}(\vec{b})$ (number of spectator nucleons).

$$N_{coll}(b) = \sum_{n=1}^{AB} nP(n,b) = AB \cdot P_{AB}(b) \tag{1.12}$$

$$N_{part}(b) = A\int \hat{T}_A(s)\{1-[1-\hat{T}_B(s-b)\sigma_{inel}^{\mathrm{NN}}]^B\}d^2s + B\int \hat{T}_B(s-b)\{1-[1-\hat{T}_A(s)\sigma_{inel}^{\mathrm{NN}}]^A\}d^2s \tag{1.13}$$

$$N_{spec}(b) = A+B-N_{part}(b) \tag{1.14}$$

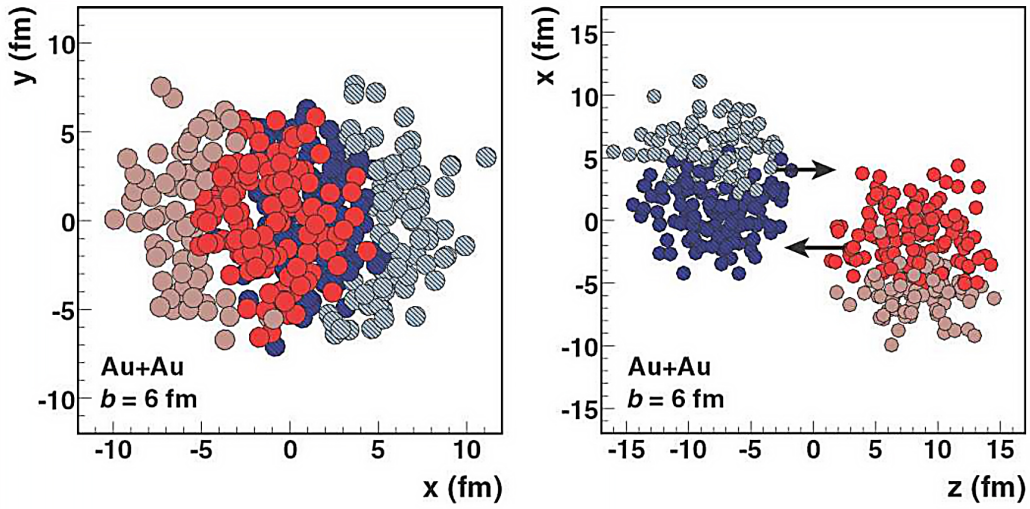

FIGURE 1.9 Glauber Monte Carlo $Au-Au$ collision with impact parameter $b = 6$ fm seen in the trasverse plane (left) and along the beam axis (right). Nucleons area is equal to σ_{inel}^{NN}. From [2].

In figure 1.9 participants of a $Au-Au$ collision are shown in dark blue and red, while semi-transparent blue and red dots represent the spectators. The figure is the representation of a specific generated event. The average numbers of participants, spectators and collisions is obtained via the statistical analysis of the whole set of Monte Carlo events, and not from a single event snapshot.

Through the Glauber model a measurement of the number of participant or spectator nucleons can provide an indirect measurement of the impact parameter of a nuclear collision. Unfortunately neither $N_{part}(b)$ nor $N_{spec}(b)$ can be directly measured. Typically the number of participants is related to the charged particles multiplicity (N_{ch}). N_{ch} has been measured over a large range of rapidity and is well described by a negative binomial distribution [25]. This approach allows one to simulate an experimental multiplicity distribution that can then be linked to an experimental observable. In figure 1.10 the collision probability is represented as a function of N_{ch}. Additional axes represent the correlation between N_{part}, b and fraction of the total cross section σ/σ_{tot}. A typical centrality detector provides a signal whose amplitude is proportional to N_{ch}, hence the source of the main centrality evaluation. An example is given in figure 1.11.

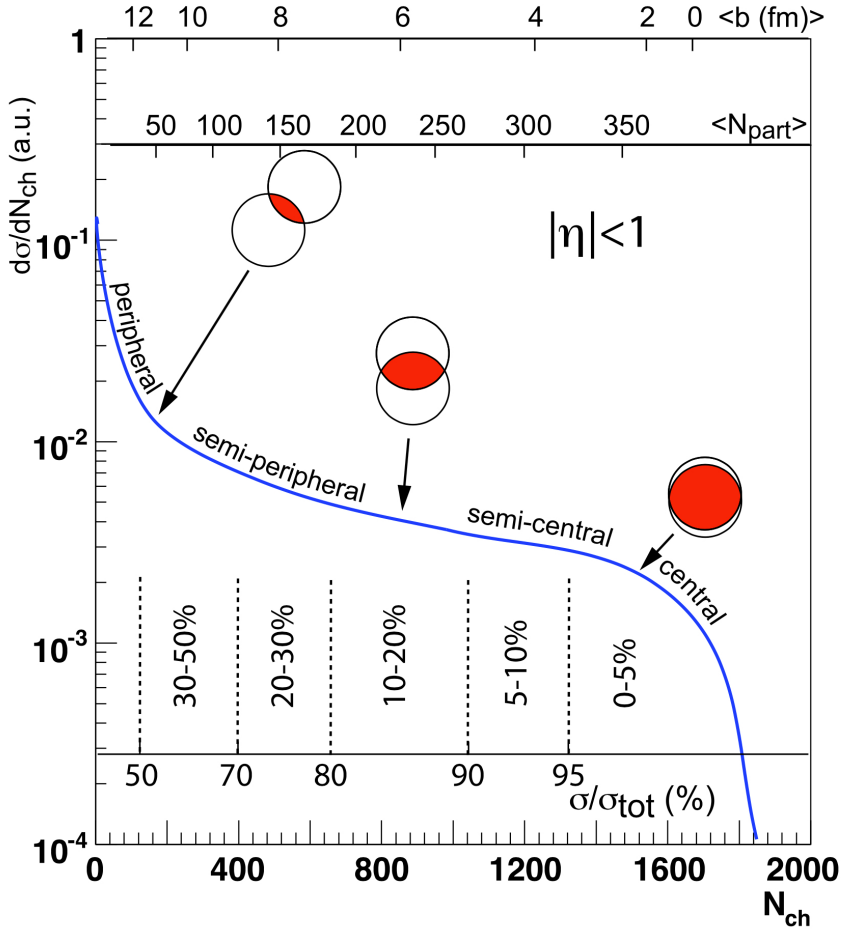

FIGURE 1.10 A cartoon example of the correlation of the final state observable N_{ch} with Glauber calculated quantities (b, N_{part}). The plotted distribution and various values are illustrative and not actual measurements. From [2].

1.1.5 Nuclear modification factor

In general the study of the modifications of the production of hard probes in heavy nuclei collisions, with respect to proton–proton collisions, makes use of the nuclear modification factor which is defined as :

$$R^X_{\mathrm{AA}} = \frac{N^X_{\mathrm{AA}}}{< N_{coll} > \cdot N^X_{\mathrm{pp}}} \tag{1.15}$$

where $< N_{coll} >$ is the average number of binary nucleon–nucleon collisions happening in the nucleus–nucleus collision and N^X_{pp} and N^X_{AA} are the yields of X states in a proton–

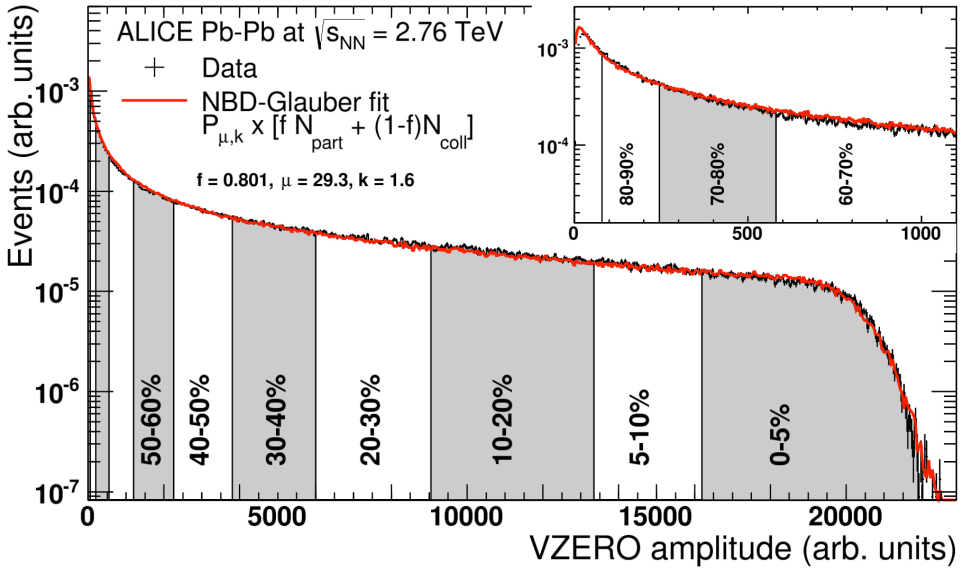

FIGURE 1.11 Distribution of the sum of signal amplitudes from a centrality detector. The distribution is fitted with the NBD-Glauber fit shown as a red line. The centrality classes used in the analysis are indicated in the figure. The inset shows a zoom of the most peripheral region. From [3].

proton and a nucleus–nucleus collision, respectively. The denominator of this expression originates from the assumption that a nuclear collision is an incoherent superposition of nucleon collisions. To simplify, the denominator corresponds to the number of Xs one would be able to measure in the case of absence of nuclear effects. The R^X_{AA} represents the deviation from the picture in which the nucleus collision is an incoherent scattering of its nucleon constituents The yields of a given state X are defined as the ratio between its production cross section and the minimum bias cross section :

Since the nuclear overlap function is defined by :

$$T_{\mathrm{AA}} = \frac{< N_{coll} >}{\sigma_{\mathrm{pp_{MB}}}} \tag{1.16}$$

Equation 1.15 can be written as :

$$R^X_{\mathrm{AA}} = \frac{N^X_{\mathrm{AA}}}{T_{\mathrm{AA}} \cdot \sigma^X_{\mathrm{pp}}} \tag{1.17}$$

Three scenarios can be foreseen for the nuclear modification factor :

— $R^X_{\mathrm{AA}} < 1$: a net suppression of the production of Xs is measured ;

— $R^X_{\mathrm{AA}} > 1$: a net enhancement of the production of Xs is observed ;
— $R^X_{\mathrm{AA}} = 1$: the nucleus–nucleus collision can be interpreted as an incoherent superposition of binary nucleon–nucleon collisions. Note that this situation might occur even in the case where suppression and enhancement effects balance out perfectly.

1.2 Bottomonium study

1.2.1 Rationale of bottomonium study

Quarkonia, *i.e.* bound states of charm or bottom quark-antiquark pairs, are sensitive probes of color deconfinement. Due to their heavy mass, heavy quarks are produced in the initial parton–parton interactions and propagate in the hot and dense medium. The presence of the medium provides a screening between the colour charges of the quarks and anti-quarks in a way which is analogous to the Debye screening of electric charges in a plasma, eventually leading to the dissociation of the bound states [26–28]. The dissociation temperature depends on the binding energy of the quarkonium states [29]. Less bound states are easily melted, while the most bound states required a much higher temperature. The dissolution of energetically ordered resonances, and their resulting suppression in the final state, can be correlated to the medium temperature. This melting process, called sequential suppression, can therefore be used as a thermometer of the medium itself (see figure 1.12).

First studies of quarkonium production in heavy-ion collisions were devoted to charmonium states, and a suppression of their yields was observed at the SPS [30–32], at RHIC [33, 34] and at the LHC [35–37]. The much smaller J/ψ suppression observed at LHC energies, despite the centre-of-mass energy per nucleon pair ($\sqrt{s_{\mathrm{NN}}}$) being one order of magnitude larger than at RHIC, is now explained by means of a competition between suppression and regeneration phenomena, which occurs during the deconfined phase and/or at the hadronization stage of the system [38–41]. At the LHC energies, the high abundance of charm quarks and bottom quarks to some extent makes non-negligible the probability of the regeneration to occur. While at RHIC the charm pairs abundance was of about 10 pairs per central collision, at the LHC the estimation rises to $\simeq 100$. The recombination process can lead to an enhancement of the production of a given quarkonium state, providing a concurrent effect to the aforementioned suppression and has been found to be more important at low p_{T} (due to easier recombination at low momenta) and in the most central collisions (due to the larger number of $c\bar{c}$ pairs) [42, 43].

Models able to reproduce the charmonium production rates include a sizeable regeneration contribution. However, the details of the suppression and regeneration mechanisms cannot

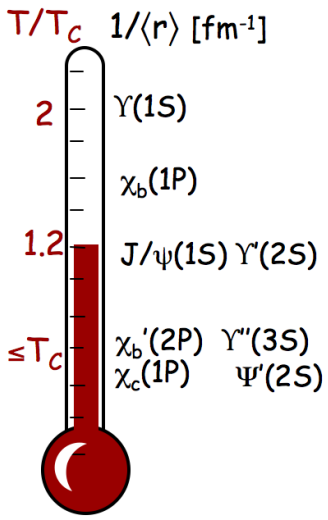

FIGURE 1.12 Cartoon representation of the dissociation temperatures of several quarkonium states. The sequential suppression can provide information regarding the average kinetic energy of the formed QGP droplet, leading to a QGP thermometer.
From [44]

be fully disentangled when measuring only charmonium states. Bottomonium states are expected to be much less affected by recombination with respect to charmonium states, due to the higher mass of the bottom quarks, hence to their lower abundance in the system. Since the $b\bar{b}$ yield in central heavy-ion collisions amount to a few pairs (≈ 10) per event at the LHC, the probability for regeneration of bottomonia through recombination is much smaller than in the case of charmonia (≈ 100 pairs). Incidentally the average number of $b\bar{b}$ pairs at the LHC is similar to the abundance of $c\bar{c}$ pairs at RHIC. The much lower regeneration contribution makes the bottomonium states the best candidates for a Debye-based QGP thermometer.

Is worth mentioning that, for bottomonium production, perturbative calculations of production rates in elementary nucleon-nucleon collisions are more reliable than for charmonium yields due to the higher mass of the bottom quark with respect to charm.

In conclusion the study of bottomonium production can provide an independent measurement of QGP characteristics, adding up to charmonium measurements to better understand the dissociation and recombination contributions to quarkonia production.

In addition bottomonium production theoretical estimates [45] indicate that its formation may occur before QGP thermalization [46]. In this situation, a quantitative description of the influence of the medium on the bound states becomes challenging. Even if the dissociation temperatures may vary significantly between different models [27, 28], it is commonly

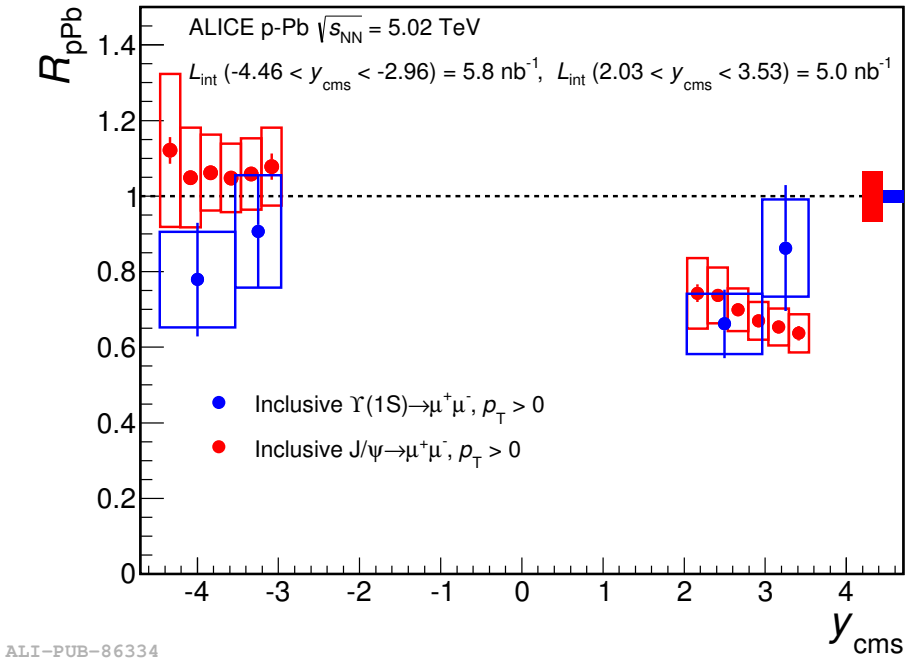

FIGURE 1.13 J/ψ (red) and $\Upsilon(1S)$ (blue) nuclear modification factor as a function of y measured by ALICE in p-Pb collisions ($-4.46 < y < -2.96$ and $2.03 < y < 3.53$) at $\sqrt{s_{NN}} = 5.02$ TeV. From [4]

accepted [47] that the spectral functions of the bottomonium states are affected by the high temperature of the surrounding medium. This effect leads to much larger spectral widths than in vacuum. Finally, the feed-down processes from higher mass resonances are not negligible (around 40% for the $\Upsilon(1S)$ and 30% for the $\Upsilon(2S)$ [28]) and must be therefore taken into account in the study of the suppression of the ground states.

The bottomonium suppression due to the QGP should be disentangled from the modification due to Cold Nuclear Matter (CNM) effects, such as the nuclear modification of the parton distribution functions [48, 49], as well as parton energy loss [50]. These effects on the bottomonium production were studied in p–Pb collisions by ALICE [51] and LHCb [52], which reported for the $\Upsilon(1S)$ a nuclear modification factor slightly lower than unity at forward rapidity and compatible with unity at backward rapidity, although with significant uncertainties (see Fig. 1.13). As a side note, in both rapidity ranges the compatibility between J/ψ and $\Upsilon(1S)$ is verified, suggesting a similar CNM effects contribution for charmonium and bottomonium.

Recently, ATLAS results indicate a significant suppression of the $\Upsilon(1S)$ around mid-rapidity [53]. Additional measurements at forward/backward rapidity with higher statistics, are needed to fully constrain the models.

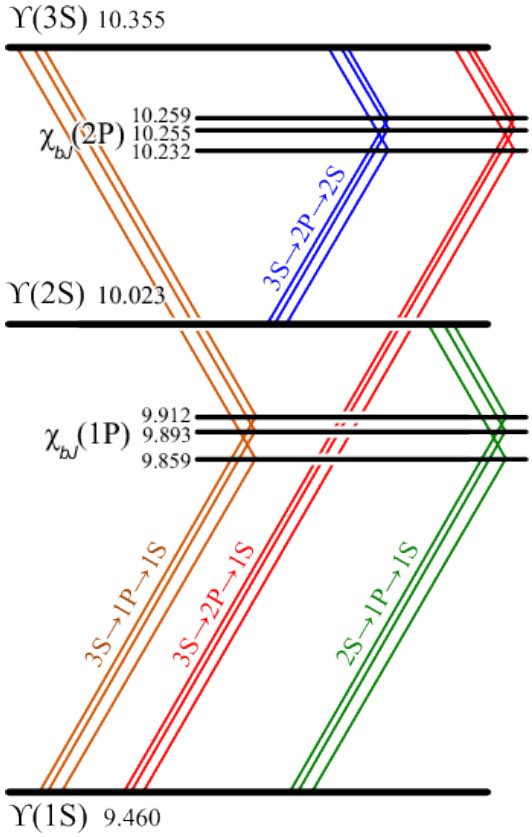

FIGURE 1.14 Representation of possible feed-down patterns for bottomonium states as measured from BaBar collaboration and reported in [5]. The numbers refer to the masses as reported by the PDG. Splittings in the photon spectra for these cascades are due to the mass splittings in the intermediate states χ_{bJ} with J = 0, 1 or 2. From [5]

1.2.2 Previous results

The charmonium production was measured in heavy-ion collisions at the SPS and RHIC. A similar suppression with respect to the yields measured in pp collisions was observed in the two cases, despite the large gap in the colliding energy [54]. Before the beginning of the LHC operations, the RHIC accelerator was leading the edge of QGP-oriented research. The PHENIX collaboration measured the J/ψ suppression in Au-Au collisions at $\sqrt{s_{\mathrm{NN}}} = 200$ GeV, highlighting a suppression strongly correlated with the centrality of the collision. The first J/ψ measurements at the LHC challenged even more the commonly accepted models, since a much lower suppression was observed in the most central collisions at LHC at $\sqrt{s_{\mathrm{NN}}} = 2.76$ TeV with respect to what had been observed at $\sqrt{s_{\mathrm{NN}}} = 200$ GeV at RHIC (Fig. 1.15).

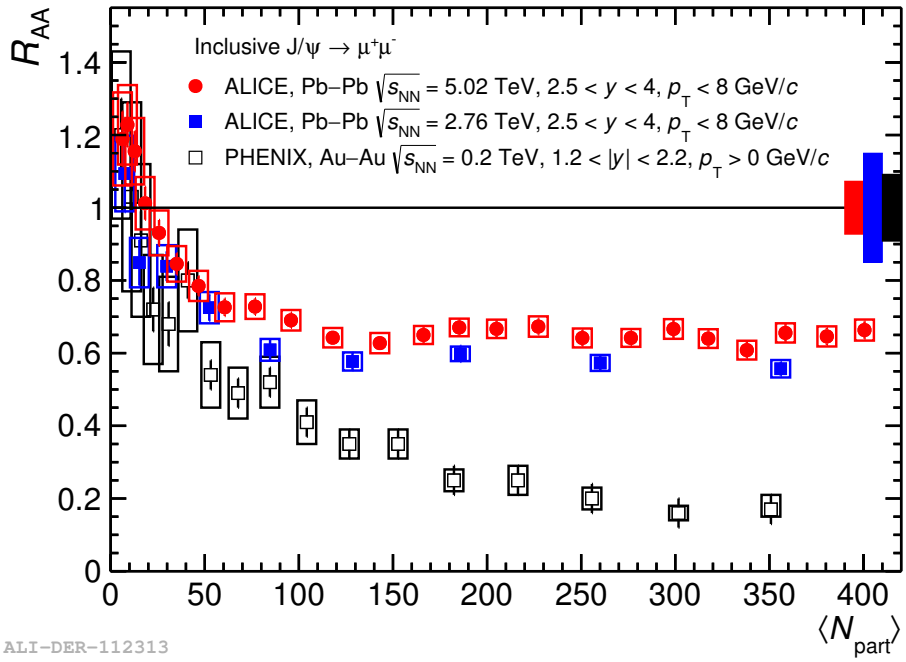

FIGURE 1.15 J/ψ nuclear modification factor measured by PHENIX (RHIC) at $\sqrt{s_{\rm NN}} = 200$ GeV (open black) and by ALICE at the LHC at $\sqrt{s_{\rm NN}} = 2.76$ and 5.02 TeV (blue and red, respectively), as a function of the number of participant nucleons. The RHIC points appear systematically below ALICE ones for $< N_{part} >= 50$, indicating a much lower suppression at LHC in the most central collisions. The two ALICE series appear to be in agreement over the whole centrality spectrum despite a factor $\times 2$ in the center of mass energy. From [4]

The data can be consistently described by models that implement statistical regeneration mechanisms for the J/ψ production. Such models suggested that for Υ(1S) production the regeneration effects would be negligible, even at LHC energies conditions, hence the bottomonium production studies were performed as well on the same data set. As one can notice by performing a comparison between figures 1.15 and 1.16 the Υ $R_{\rm AA}$ at $\sqrt{s_{\rm NN}} = 2.76$ TeV appears to be similar to the J/ψ one, measured at RHIC. This observation can be related to the fact that the estimations of the total number of bottom quark pairs at the LHC is similar to the number of charm quark pairs at RHIC, even if different medium temperatures and feed-down fractions could alter the picture. A strong suppression of the Υ(1S) state in Pb–Pb collisions at $\sqrt{s_{\rm NN}} = 2.76$ TeV was measured by ALICE using properly scaled measurements from pp collisions by ALICE [6] and CMS [55, 56], in the rapidity ranges $2.5 < y < 4.0$ and $|y| < 2.4$, respectively (see Fig. 1.17).

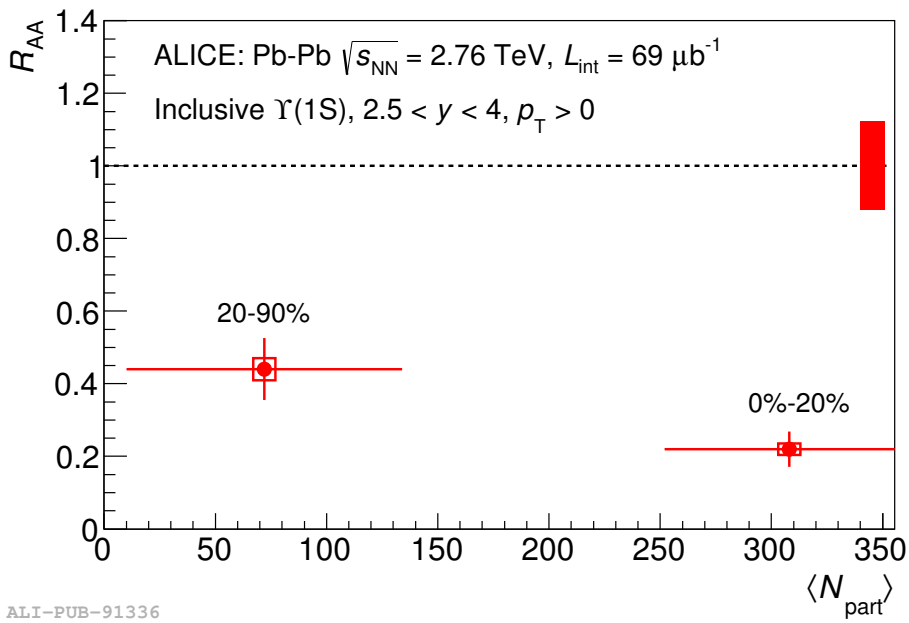

FIGURE 1.16 ϒ nuclear modification factor measured at the LHC by ALICE at $\sqrt{s_{NN}} = 2.76$ TeV. Two centrality bins are shown, referring to the quoted centrality distribution percentiles. From [6]

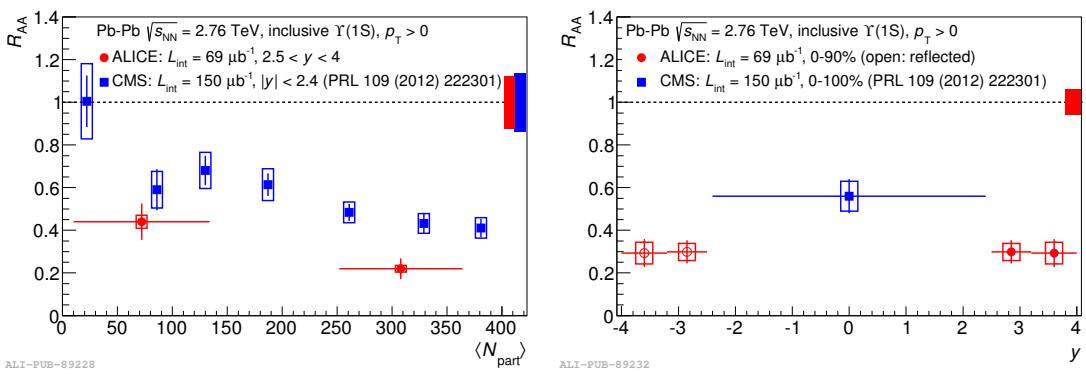

FIGURE 1.17 ϒ(1S) nuclear modification factor as a function of $< N_{part} >$ (left) and y (right) measured by ALICE (red points, $2.5 < y < 4.0$) and CMS (blue points, $|y| < 2.4$) at $\sqrt{s_{NN}} = 2.76$ TeV. From [6]

The suppression increases with the centrality of the collision, reaching about 60% and 80% for the most central collisions at mid- [56] and forward rapidity [6], respectively. Moreover, the ϒ(2S) suppression reaches about 90% while the one for ϒ(3S) is compatible with 100% [56]. The transverse momentum dependence of the ϒ(1S) R_{AA}, measured for $p_T < 20$ GeV/c by CMS [56], is compatible with a constant value. When considering the y-

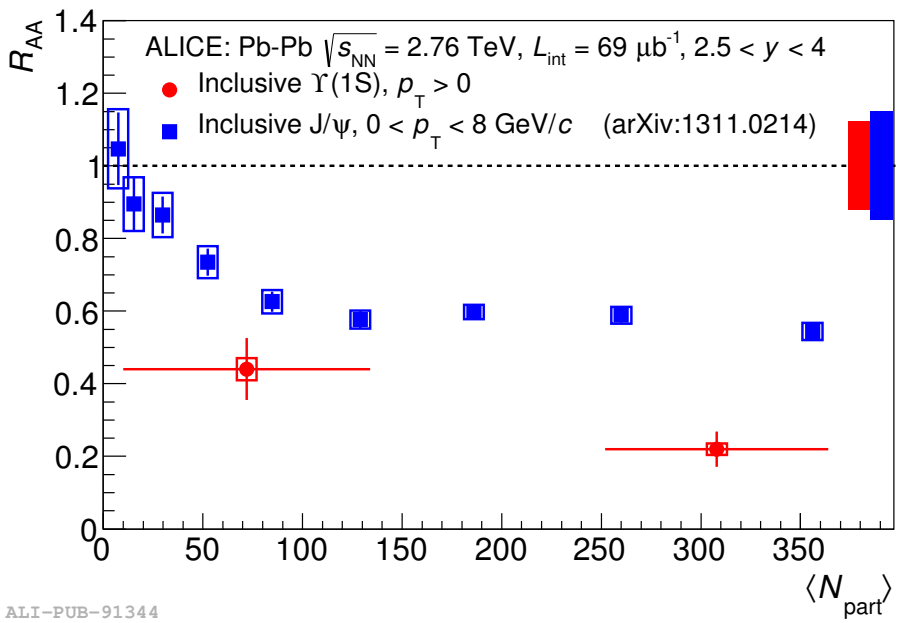

FIGURE 1.18 J/ψ (blue) and Υ(1S) (red) nuclear modification factor as a function of $< N_{part} >$ measured by ALICE at forward rapidity ($2.5 < y < 4.0$) at $\sqrt{s_{\rm NN}} = 2.76$ TeV. From [6]

dependence resulting from the comparison of ALICE and CMS results, there is an indication for a stronger suppression at forward y. Transport models [41, 13] fairly reproduce the experimental observations of CMS, while they tend to overestimate the $R_{\rm AA}$ values measured by ALICE. Similar conclusions can be obtained in the frame of an anisotropic hydrodynamic model [15]. The comparison between J/ψ and Υ(1S) measurements performed by ALICE, reported in figure 1.18, denotes a much stronger suppression for the latter ($> 3\sigma$) in the most central collisions.

1.3 The Large Hadron Collider

The Large Hadron Collider (LHC) is the most powerful particle accelerator ever built. It is the largest element of the CERN acceleration facility and has been placed in the same 27 km long tunnel previously used for the Large Electron Positron collider (LEP) placed between 45 and 170 m underground. The CERN acceleration facilities are depicted in figure1.19. Some of the previous CERN accelerators are connected together and now used as pre acceleration steps for the final LHC injection.

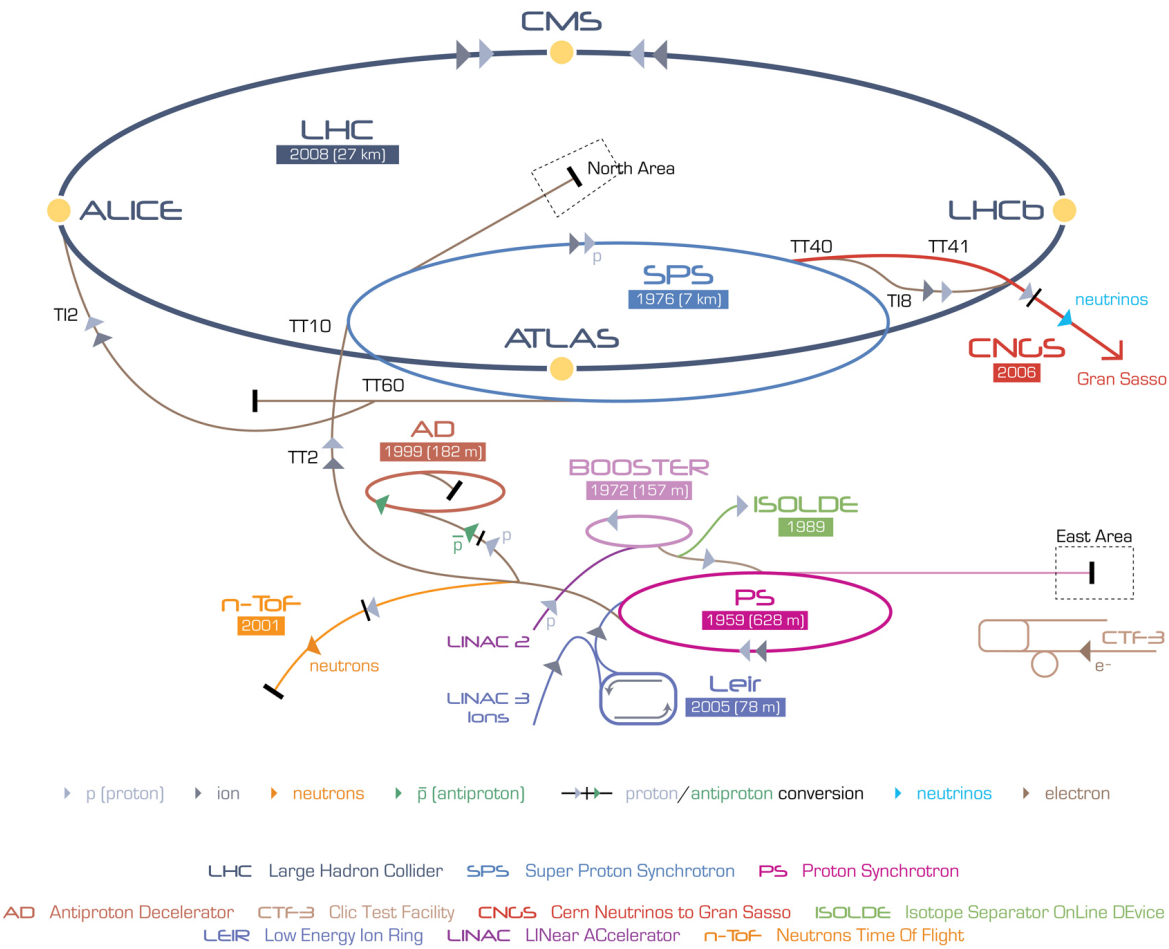

FIGURE 1.19 Schematic representation of the CERN accelerator complex. [source]

The LHC allows one to perform proton-proton, proton-Pb and Pb-Pb collisions (and lately also Xe-Xe). For what concerns the pre-acceleration of protons the CERN LInear ACcelerators (LINAC), the Proton Synchrotron Booster (PSB), the Proton Synchrotron (PS) and the Super Proton Synchrotron are used upstream the LHC. The heavy nuclei are instead firstly produced, ionized and accelerated in the Low Energy Ion Ring (LEIR) and then injected directly in the PS-SPS chain. Thanks to the superconducting magnets (dipoles, quadrupoles and higher order ones) protons and nuclei can be accelerated by design up to 7 TeV and 2.75 TeV respectively. Such energy has not been achieved yet, due to insufficient magnets performance, instead the maximum reached energies were 6.5 and 2.5 TeV. Along the LHC ring four main experiments are placed : ALICE (A Large Ion Collider Experiment), ATLAS (A Toroidal LHC ApparatuS), CMS (Compact Muon Solenoid) and LHCb (Large Hadron Collider beauty).

1.4 ALICE experimental setup

The main purpose of the ALICE experiment is the study of the physics of strongly interacting matter in ultra-relativistic heavy-ion collisions. It is also designed for proton-proton and proton-nucleus collisions which represent an important part of its physics program. The experiment itself can be divided into three main sectors :

— ancillar detectors are used for triggering, event characterization and beam luminosity measurements ;

— central barrel detectors are embedded into a solenoid with a magnetic field of $B = 0.5$ T and are used for tracking and identification of charged particles and photons ;

— muon spectrometer covers the forward region with respect to the interaction point and its detectors are designed for muon tracking and trigger.

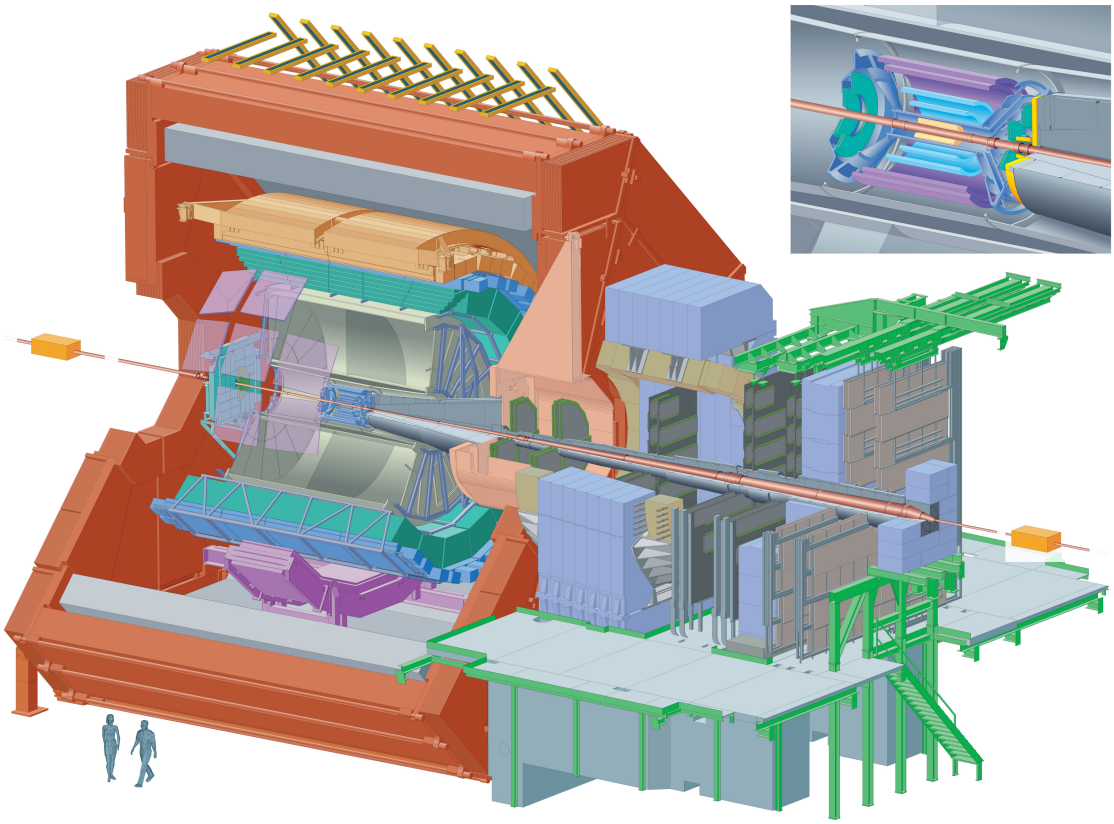

FIGURE 1.20 Schematic of ALICE detectors setup, with a maximised view of the innermost detectors. [source]

The detector is completed by an array of scintillators to trigger on cosmic rays. A more detailed discussion of the ALICE detectors is reported in the following sections.

1.4.1 V0 and Zero Degree Calorimeters (ZDC)

The two most relevant ancillar detectors for the work described in this thesis are introduced below.

ZDC

The main task performed by these calorimeters is the estimation of the collision centrality via the energy deposited by the spectator nucleons. There are two ZDCs, each composed of a neutron detector (ZN) and a proton detector (ZP). They are located ± 113 m away from the IP; at such distance, protons and neutrons are spatially separated by the LHC magnetic elements : for this reason, while the neutron calorimeter is placed at zero degrees with respect to the LHC beam axis, the proton calorimeter is displaced (see Fig. 1.21).

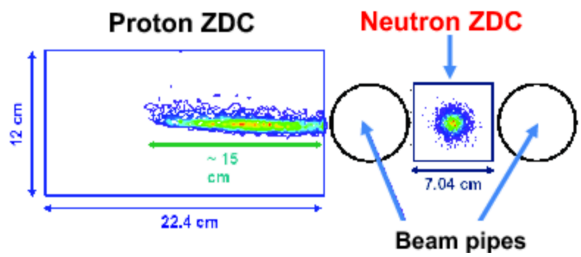

FIGURE 1.21 Schematic representation of the ZDC along the z-axis. The trasverse positions of the beam pipes, ZN and ZP are shown. From [7]

V0

The V0 detector (Fig. 1.22) is composed of two scintillator hodoscopes located at 90 cm ($V0_C$, muon spectrometer side) and -340 cm ($V0_A$, PMD side) from the interaction point. Its main tasks are the delivery of minimum bias and centrality triggers, the offline estimation of centrality, the rejection of beam-gas interactions and the measurement of luminosity.

1.4.2 Central barrel detectors

The mid-rapidity section of the ALICE experimental apparatus is named central barrel. It includes many detectors, each of them with different purposes. The structure surrounds the interaction point, covering the pseudorapidity range up to $|\eta| < 1.4$, and it is inside the 0.5 T magnetic field generated by a warm solenoidal magnet originally employed by the L3 collaboration.

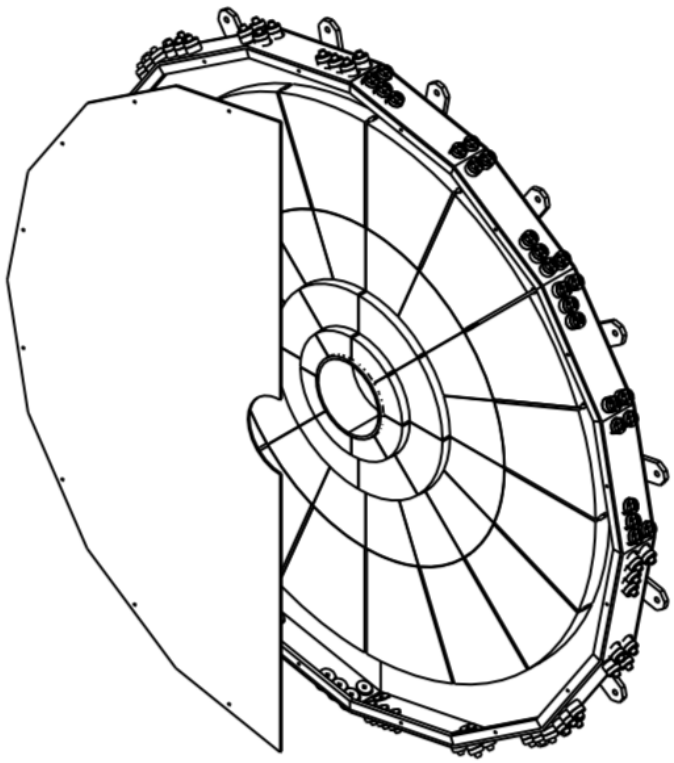

FIGURE 1.22 Schematic representation of one of the two V0 arrays ($V0_A$).

Inner Tracking System (ITS)

The ITS is the closest detector to the beam pipe of the ALICE apparatus. Its purposes are the identification of primary collision vertexes, the reconstruction of secondary vertexes from heavy particles decays and the tracking and identification of low momentum particles. The spatial resolution of the ITS is better than 100 μm. It is completely made of silicon detectors, implemented using three technologies. Six layers compose the ITS and are shown in Fig. 1.23 :

— Silicon Pixel Detector (SPD) : two layers located at 3.9 and 7.6 cm from the interaction point, they are important for a high spatial resolution and for their very fast response ;

— Silicon Drift Detector (SDD) : two layers located at 15 and 23.9 cm from the interaction point, they provide a bi-dimensional spatial information ;

— Silicon Strip Detector (SSD) : two layers located at 38 and 43 cm from the interaction point, they provide a complementary information on track positions.

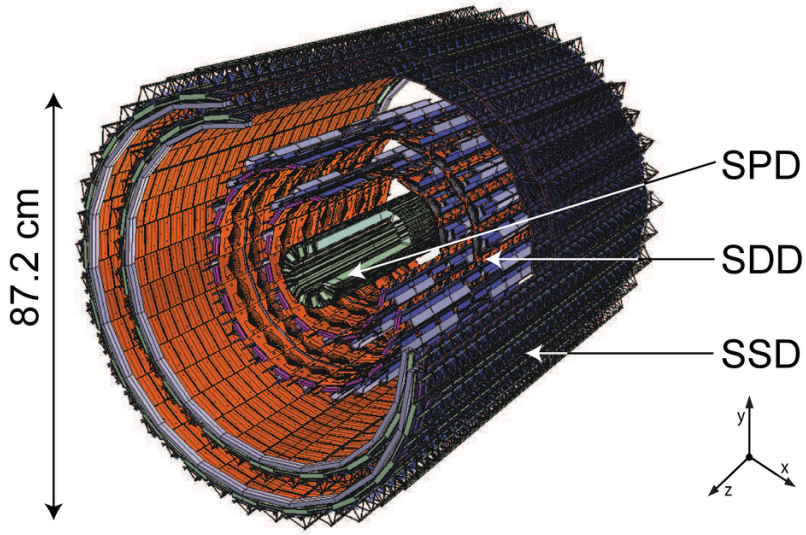

FIGURE 1.23 Schematic of the ALICE ITS. From [8]

Time Projection Chamber (TPC)

The Time Projection Chamber is the main tracking detector of the central barrel. It is a 88 m^3 cylindrical detector filled with a gas mixture of $Ar - CO_2$ $(90 - 10\%)$ for most of the operation time. Its volume is limited by two end-plates acting as segmented read-out electrodes. In addition an electrode is placed in the middle of the TPC, dividing it into two halves, as shown in figure 1.24. The ionizing particles crossing the detector ionize the gaseous mixture. The freed electrons drift towards the read-out electrodes. As a result the side projection of the track is obtained directly from the electrodes, while the third coordinate of the points is obtained through the time of arrival of each segment.

Transition Radiation Detector (TRD)

The purpose of the Transition Radiation Detector is the electron identification. It consists of six layers of multi-wire proportional chambers, filled with a mixture of Xe and CO_2, equipped with a radiator made of optical fibers embedded in plastic foam directly glued on the electrode. The modular structure is detailed in figure 1.25. It is designed to provide charged-particle tracking, electron identification via transition radiation and pion rejection.

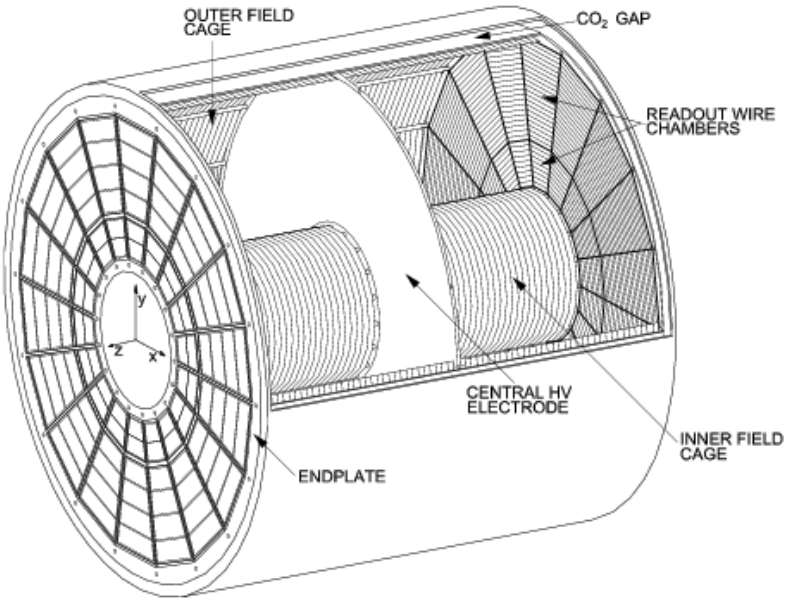

FIGURE 1.24 Representation of the TPC with some details of the layout. From [9]

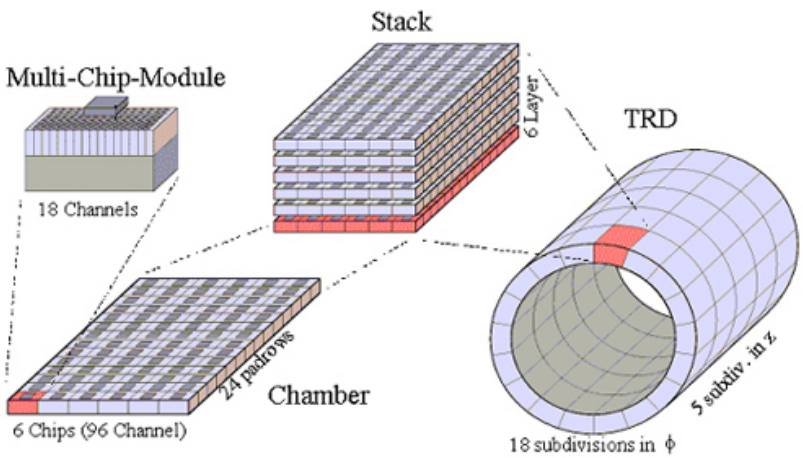

FIGURE 1.25 Schematic of the ALICE TRD with an highlight on the modular struture of the detector. [source]

Time Of Flight (TOF)

The Time Of Flight detector is designed to identify charged particles with a momentum from 1 to few GeV/c, extending the TPC particle identification capabilities. It is composed by multi-gap resistive plate chambers arranged into 18 sectors in a cylindrical shell placed

3.7 m far from the beam pipe (Fig. 1.26). The TOF provides the arrival time of a particle in the detector volume with a resolution of 80 ps, completing the information gathered by TPC and TRD, in terms of identification of the detected particles, in particular separating π/K up to 2.2 GeV/c and K/p up to 4 GeV/c.

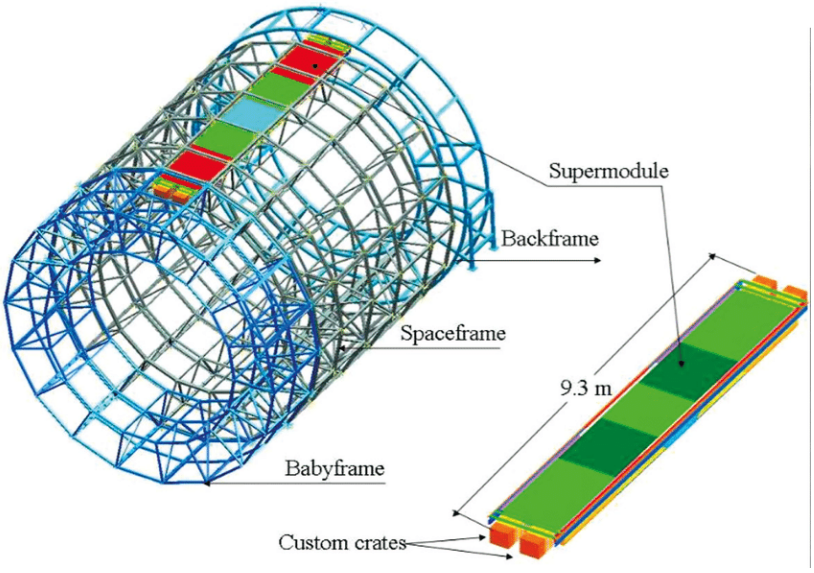

FIGURE 1.26 Schematic of the ALICE TOF. A detector module is represented along with the support structure. From [10]

High Momentum Particle Identification Detector (HMPID)

The main purpose of HMPID is to enhance the particle identification capability beyond the range allowed by ITS, TPC and TOF. It is based on proximity focusing Ring Imaging Cherenkov (RICH) counters and consists of seven modules mounted in an independent support cradle (Fig. 1.27). When a fast charged particle traverses the 15 mm layer of liquid C_6F_{14}, Cherenkov photons are emitted and detected by the photon counter, which is a thin layer of *CsI* deposited onto the pad cathode of multi-wire proportional chambers.

PHOton Spectrometer (PHOS)

The Photon Spectrometer is a high resolution electromagnetic spectrometer (Fig. 1.28) which consists of a highly segmented electromagnetic calorimeter of lead-tungstate crystals. It is located on the bottom of the ALICE experimental apparatus, covering the pseudorapidity range $|\eta| < 0.12$ and an interval of $\frac{5}{9}\pi$ radiants in the azimuthal angle. It is designed for

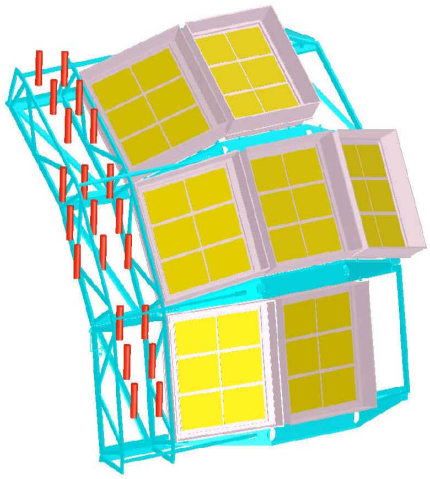

FIGURE 1.27 The HMPID layout. [source]

measuring photons and neutral mesons (π_0 and η) through their decays into two photons up to momenta about 10 GeV/c.

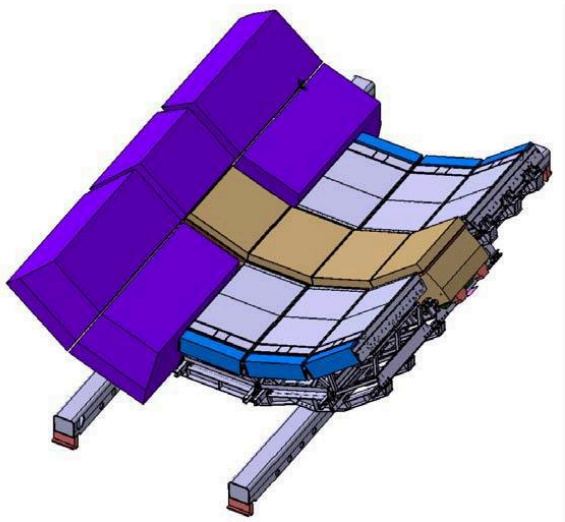

FIGURE 1.28 The PHOS layout (brown) along with the DCal detector arrays (blue and light blue). [source]

ElectroMagnetic Calorimeter (EMCal) and Di-jet Calorimeter (DCal)

Positioned on the top and bottom of the ALICE structure, close to the solenoid coils, EMCal is designed to study jet quenching and it is used for triggering on photons, electrons

and jets. It is composed of towers of lead scintillators with photomultiplier readout and it covers a pseudo-rapidity range of $|\eta| < 0.7$ (Fig. 1.29). The Di-jet calorimeter is an additional array of electromagnetic calorimeter which expands the acceptance of EMCal, allowing for back-to-back correlations (Fig. 1.28).

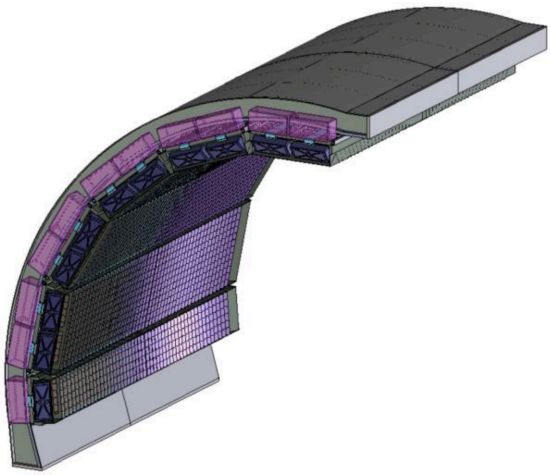

FIGURE 1.29 The EMCal layout. [source]

1.4.3 Muon spectrometer

The Muon Spectrometer is designed to measure muon production from the decays of quarkonia (J/ψ , $\psi(2S)$, $\Upsilon(1S)$, $\Upsilon(2S)$ and $\Upsilon(3S)$), low mass vector mesons (ρ, ω and ϕ) and heavy flavor hadrons. In addition it also allows for the measurement of $W^{\pm}$ and Z^0 bosons. The detector is covers the pseudorapidity region $-4.0 < \eta < -2.5$ and it has a total length of $\simeq 17$ m. For the sake of readability, the rapidity acceptance of the spectrometer and the rapidity ranges quoted in this thesis will be reported as positive ranges instead (*e.g.* $2.5 < y < 4.0$). It is composed by a system of passive absorbers, a dipole magnet, a muon tracker, an iron wall and a muon trigger system. The main components of the Muon Spectrometer will be discussed with more details in the following and are highlighted in figure 1.30.

Absorbers system

The Muon Spectrometer requires some shielding to reduce the otherwise large background produced especially in nucleus-nucleus collisions. For this reason it is equipped with a system of absorbers :

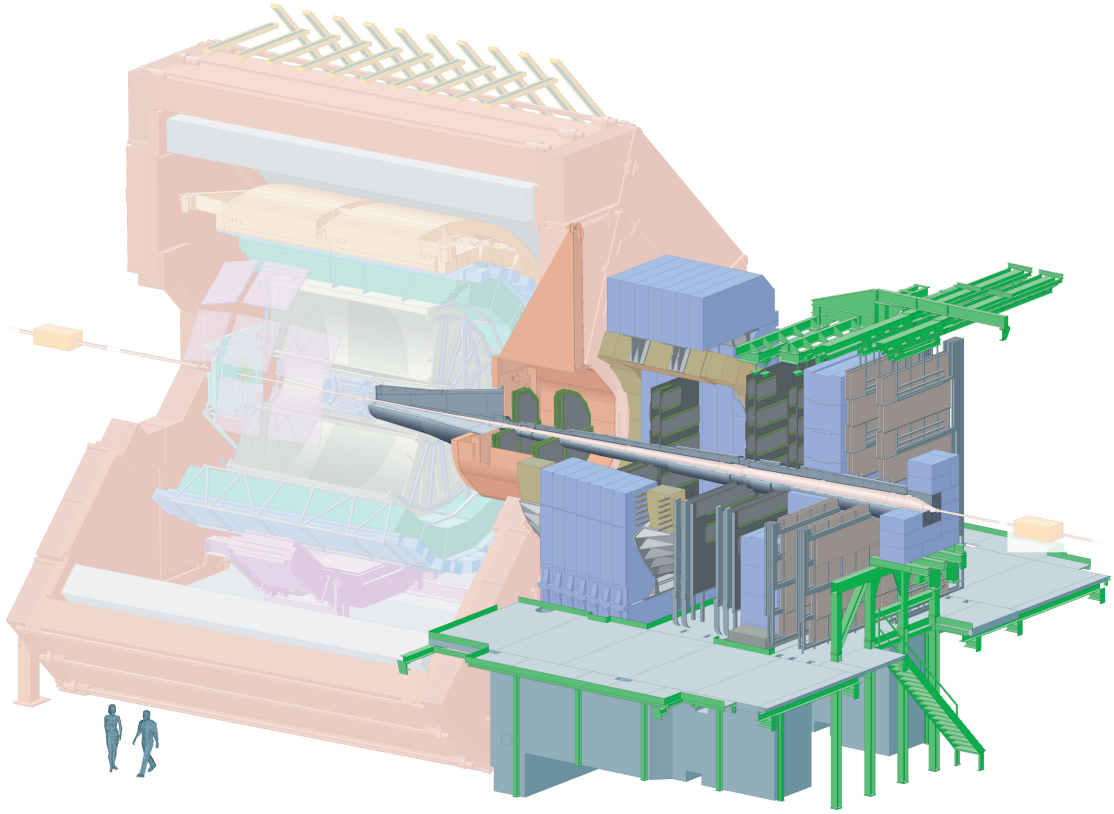

FIGURE 1.30 Schematic representation of ALICE with highlighted muon spectrometer components. [source]

— front absorber : this absorber is located as close as 90 cm from the interaction point. The purpose of the front absorber is to filter out hadrons and to reduce the background generated by pion and kaon decays. The front absorber materials were chosen to limit the multiple scattering of muons and leptons in general. The section of the front absorber placed closest to the interaction point is made of carbon to limit multiple scattering thanks to the low Z. The next sections of the absorber are composed of concrete to absorb secondary particles and low energy protons and neutrons. The whole absorber is coated of lead and boronated polyethilene to avoid decay products recoils in the TPC. A detailed view of the absorber can be found in figure 1.31 ;
— beam shield : the beam pipe is layered with this shielding made of tungsten, lead and stainless steel to shield the muon spectrometer from the particles produced in the interactions between low angle particles and gas residuals inside the beam pipe itself ;
— iron wall : this 1.2 m thick absorber is placed between two detector systems and acts as a filter capable of absorbing everything but muons ;

— rear absorber : an additional passive element has been installed around the connection hole between the experiment cave with the LHC tunnel in order to further remove products of gas interaction.

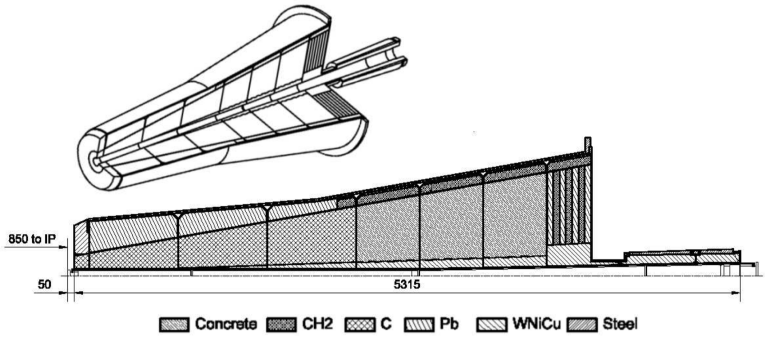

FIGURE 1.31 Detailed reprensentation of the front absorber composition.

Dipole magnet

Located at 7 m from the interaction point, the dipole magnet is used to bend the particle in such a way that the momentum and electric charge can be determined. A schematic representation is reported in Fig. 1.32. The value of the magnetic field provided (the magnetic flux density is 0.7 T and the integrated value is 3 T$\cdot$ m) is defined by requirements of quarkonium mass resolution. The magnetic field is perpendicular to the beam pipe. The ALICE reference frame is a Cartesian tridimensional space in which the z axis is placed along the beam direction, the x axis is parallel to the ground and pointing to the center of the LHC and the y axis vertical towards the top. In this reference frame the magnetic field is directed along the x axis. The charged particle are therefore deviated along y (bending direction) while the x direction is therefore referred to as non-bending.

Muon Tracker or Muon Chambers (MCH)

The tracking system is made of 10 detection planes made of multi wire proportional chambers arranged in 5 stations of 2 planes each (Fig. 1.33, round shaped layers). The produced electrons generate an avalanche drifting towards the nearest anode wire, and the resulting ion cloud induces a charge distribution on the cathode planes, allowing to determine the position of the impacting particle. The size of the chambers depends on the spectrometer's angular coverage, considering the deviation of muons by the magnetic field. The pad size of

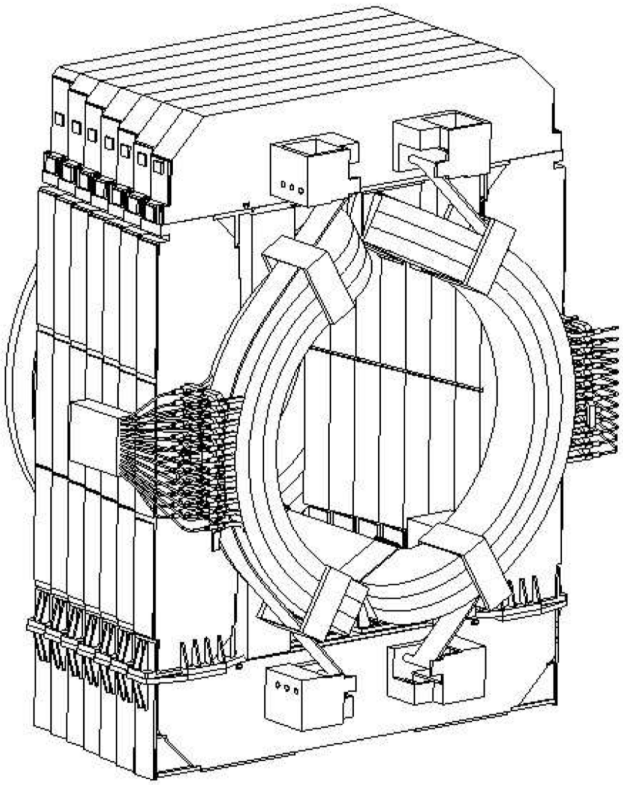

FIGURE 1.32 ALICE dipole magnet schematics.

all the chambers is smaller close to the beam pipe, in order to take into account the higher density of particles produced in that region. The spatial resolution is better than 100 μm and all the chambers are made of composite material ($< 3\%$ X_0 per chamber) to minimize the scattering of the muons in order to obtain the required resolution. To limit the occupancy to a maximum of 5% the full set of chambers has more than 1 million channels.

Muon Trigger (MTR)

The muon trigger system is designed to tag high p_T muons produced in heavy quarkonium and open heavy flavour meson decays (Fig. 1.33, square shaped layers). Thank to a configurable p_T threshold, the system is able to provide trigger signals to select interesting events and to discard events with only low p_T muons, which mainly come from pions and kaons decays. The muon trigger system is composed of 72 Resistive Plate Chambers with $x-y$ read out, organized in 4 planes paired in two stations to provide redundancy. Each RPC consists of two planes, made of bakelite and separated by 2 mm of gas. A charged

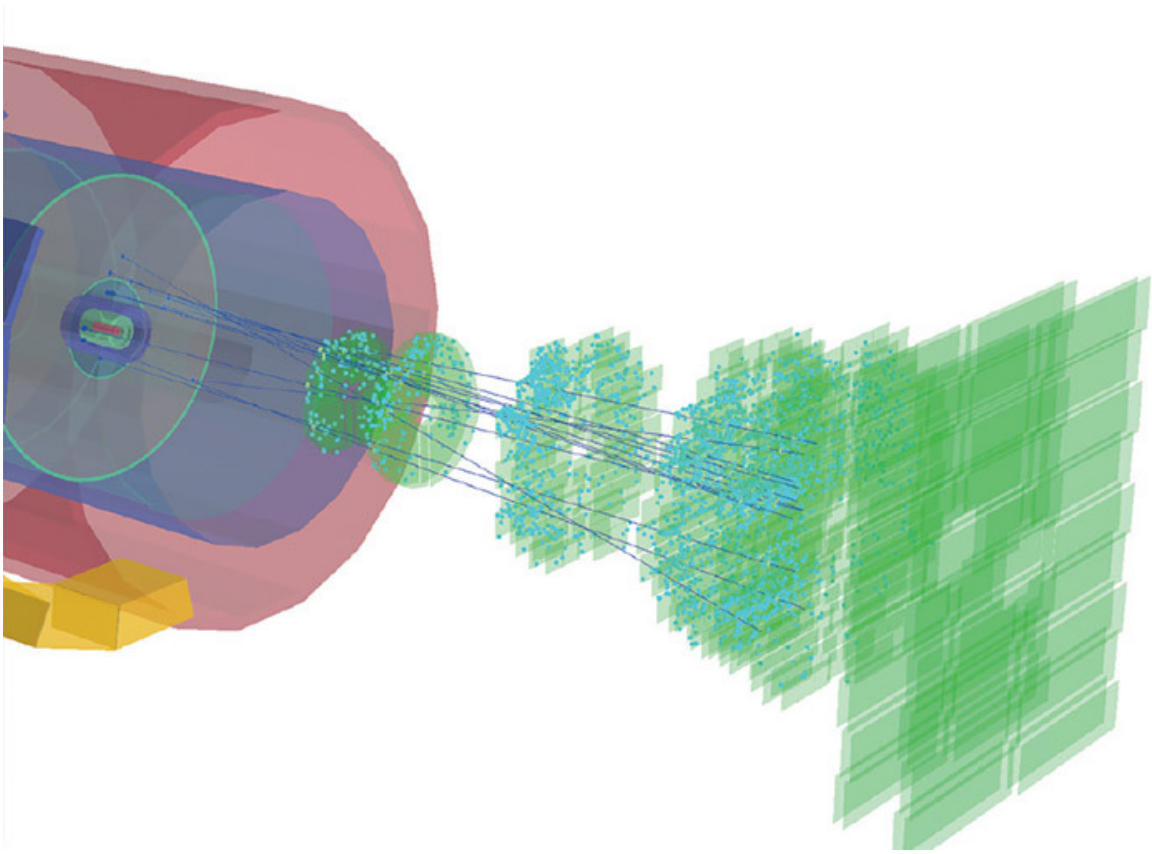

FIGURE 1.33 Digital representation of the layout of the muon chambers and muon trigger system, shown in green.

particle passing through the gas ionizes it, causing the formation of an avalanche of secondary electrons, which are picked up by the copper strips placed outside the chambers.

The read-out of the Muon Trigger System is performed through front-end electronics (FEE) boards connected to the strips. Information collected by the FEE is aggregated at the level of the Local Boards (LB). The ALICE MTR is equipped with a total of 234 local boards (Fig. 1.34). The LBs collect the strip pattern of FEE boards aligned projectively on the four planes of the MTR. In addition to the patterns of the directly aligned FEE boards, the output of the boards surrounding the corresponding one on the third and fourth planes are retrieved and combined at the LB level. This procedure is necessary for the generation of the online trigger signal, obtained looking at the hits in the first and second planes and checking if any corresponding hit is present in the patterns of the third and fourth ones. A hit on at least $3/4$ planes both in bending and non-bending directions is required to produce a trigger signal.

In order to be triggered a particle still has to pass the p_{T} cut. Such selection is performed considering the deviation of a track with respect to the track with infinite momentum. This

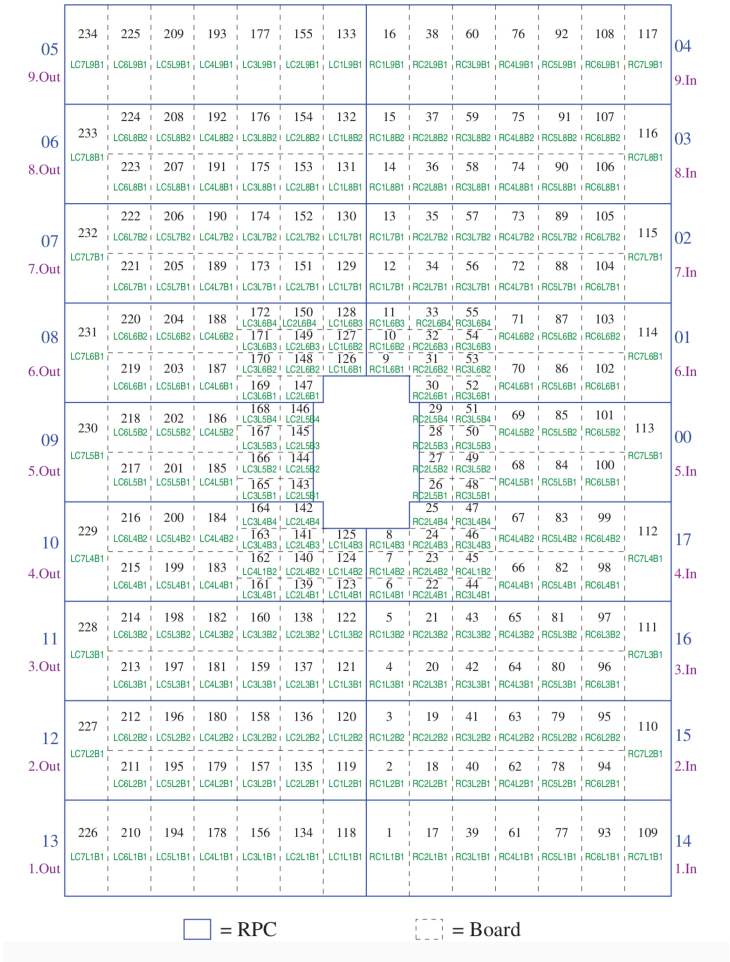

FIGURE 1.34 Local Board segmentation of the ALICE Muon Trigger.

deviation depends indeed on the p_T of the particle, being larger at low transverse momenta. The actual estimation of the p_T is performed through the Look-Up Tables (LUT) which are filled according to Monte Carlo simulations of muon tracks, in which a realistic description of all detectors as well as their segmentation and the field map of the dipole are taken into account. In the LUT, for each strip in the first trigger chamber a deviation in strip is tabulated corresponding to the maximum deviation between the first and second station allowed, corresponding to a minimum p_T of the track. The muon trigger can provide a decision based on two thresholds, to be chosen among four values : 0.5, 1, 1.7 and 4.2 GeV/c, which are tabulated in the LUT. It is worth noting that the L0 trigger cut is not sharp : the cut values

refer to the transverse momentum magnitudes at which the trigger efficiency reaches the 50%.

Chapitre 2

Measurement and monitoring of Muon Trigger System performances

2.1 History and main features of Resistive Plate Chambers

Before the invention of the RPCs, the first gaseous detectors to operate in the streamer regime were spark and streamer chambers.

Spark chambers (see Fig. 2.1) are detectors composed of a stack of metal plates put in a sealed box filled with an opportune gaseous mixture [11]. The metal plates are kept at high voltage, providing an electrical field of at least 70 kV/cm. An ionizing particle which travels through the detector causes the ionization of the gas, then the primary electron avalanche develops in $10^{-8} \div 10^{-7}$ s and subsequently the secondary ionization and the streamer development happens in $10^{-10} \div 10^{-9}$ s after the avalanche [11]. In the presence of a sufficiently high voltage, the ionized gas can drift causing a trail of sparks that allow one to reveal the ionizing particle path. The application of the high voltage cannot be permanent, because in this case the creation of a electric arcs would lead to discharge of the whole system. For this reason an additional detector is needed in order to trigger the application of the high voltage to the plates right during the passing of the ionizing particle. Typically the high voltage trigger detectors are scintillators. In addition whenever a ionizing event happens, the whole interested plates get discharged due to the local conductivity change of the gaseous mixture. After a full discharge the recovery time is macroscopic, around 10 ms, due the capacitor-like behavior of the plates stack. In addition, only particles crossing two electrodes can cause a spark.

The high dead time due to electrical recovery and the need of an external HV trigger of the spark chambers caused the development of another kind of gaseous detector. In the past

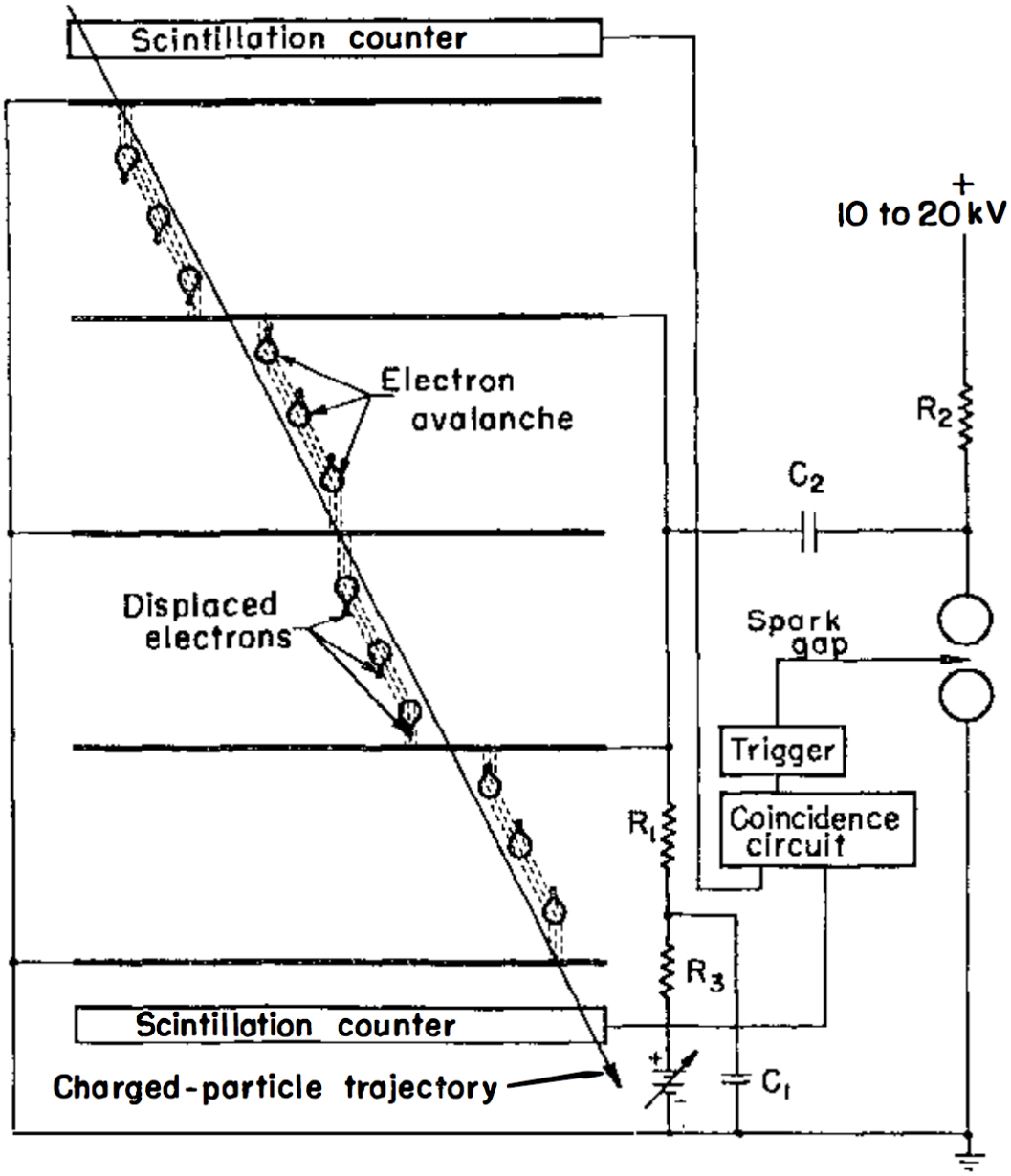

FIGURE 2.1 Spark chamber schematic with some details on the external trigger system and coincidence electronics.Extracted from [11]

the model for spark growth has prompted several groups [57] to investigate the possibilities of arresting the discharge before the streamers have developed into a spark channel. The most important consequence of this work is that the isotropic streamer chamber has been invented, in which particle trajectories at all angles to the applied electric field may be recorded. In addition the streamer chamber allowed one for the recording of more than 30 tracks at a

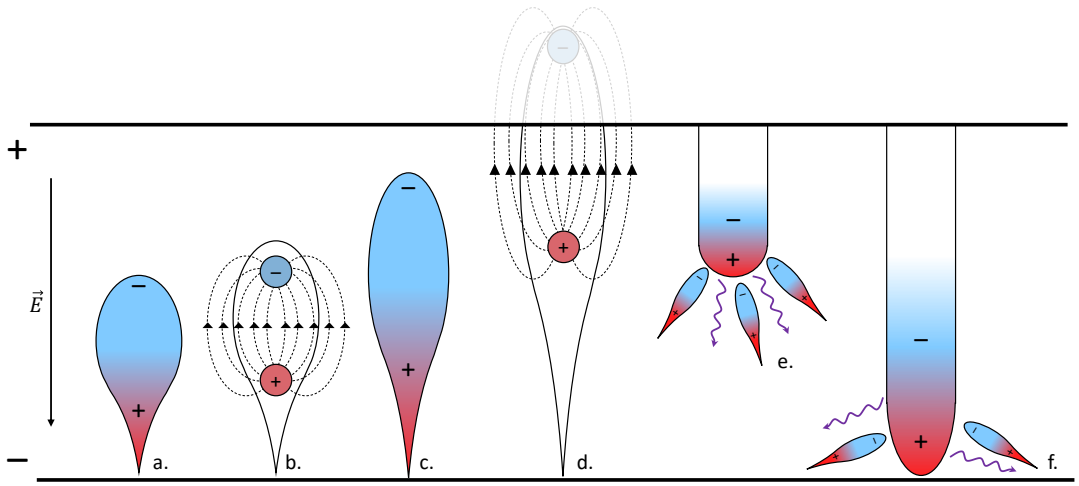

FIGURE 2.2 Transition from an avalanche to a streamer in a gaseous detector. (a) creation of the initial avalanche due to ionization of the gas ; (b-c) acceleration of electrons due to the electric field ; (d) growth of the avalanche until the internal field compensated the applied field ; (e) recombination photons cause the production of additional electron-ion pairs which generate additional avalanches at the head of the ionized region ; (f) the process continues with the merging of avalanches and the growth of the streamer.

time. In this case the electric field is not strong enough to cause an electric arc between the electrodes, but the gradient of the electric field stays strong enough to cause visible streamers around the particle path (see Fig. 2.2). While the HV was still externally triggered by fast detectors, the much lower energy required to develop streamers allowed one to reduce the pulse width down to $60 - 100$ ns. The typical way of recording a streamer chamber event was by a visible light snapshot of the streamer cavity. For this reason the cavity walls required to be transparent. The streamer mode helped in this task : while the sparks need to reach the electrodes to form, the streamer can be operated with electrodes which are either integrated in the chamber glass walls or external to the glass box.

For the first time the electric field was induced on the gas gap externally, making the gaseous mixture able to generate streamers upon ionization. Further development of this technology, aimed at reducing the HV pulse length and height, eventually incurred in the avalanche operational mode. While the streamer is a structure of avalanches which come

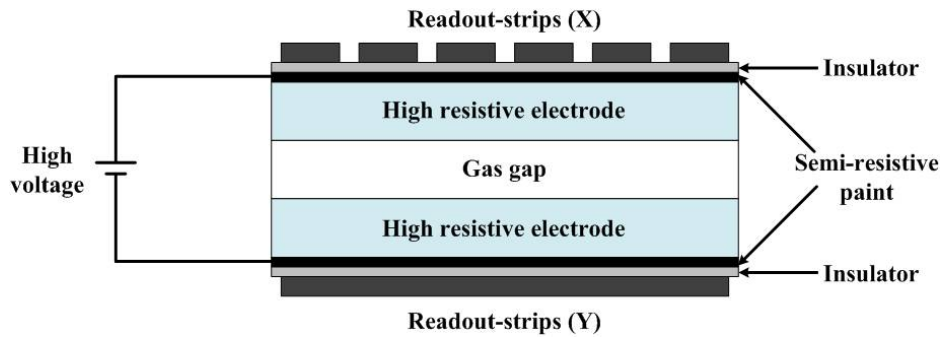

FIGURE 2.3 Schematic representation of an RPC structure from the side.

to saturation and cause a subsequent set of new avalanches, a simple avalanche is a single drop of ionized gas which develops following the electric field gradient. The discharge size and intensity is obviously reduced from spark mode to streamer mode to avalanche mode. For this reason the light output diminishes and hence the optical problems become more severe. At that point the limits of the optical readout (e.g. with a camera) started to appear and caused a further development of such detectors.

The Resistive Plates Chamber (RPC) detectors were developed by Santonico and Cardarelli [58]. The RPCs are composed of a thin gas gap of some millimeters of thickness and planar resistive electrodes, between which a HV of several kV is applied by means of a graphite coating on the outer face of each electrode. The signal is picked up inductively by means of copper strips, electrically insulated from the electrodes. The use of a resistive electrode ensures that the reduction of the electric potential between the electrodes is local, meaning that the detection happens without a complete discharge of the electrodes. Moreover, the local nature of the discharge makes RPC an intrinsically position-sensitive detector. The RPCs are relatively cheap detectors with a fast response time (of the order of *ns*) and good spatial resolution (slightly better than 1 *cm*) that can therefore cover large surfaces and sustain high particle rates. RPCs are currently adopted, mainly as muon detectors, by ALICE, ATLAS and CMS at the LHC and many other particle physics experiments around the world.

RPC detectors are made of several layers of different materials. First of all the gas gap is the innermost part of the detector and contains a gas mixture which will be discussed later. Electrodes resistivity is of the order of $10^9 - 10^{10}\ \Omega \cdot \mathrm{cm}$. The roughness of the electrodes must be as low as possible to limit the peak discharge around surface anisotropies.

For this reason the resistive electrodes are frequently coated with oils in order to improve the smoothness of the inner surface and to preserve the resistivity (see Fig. 2.4). Right outside the resistive electrodes an insulation layer made of plastic material is provided, in order to

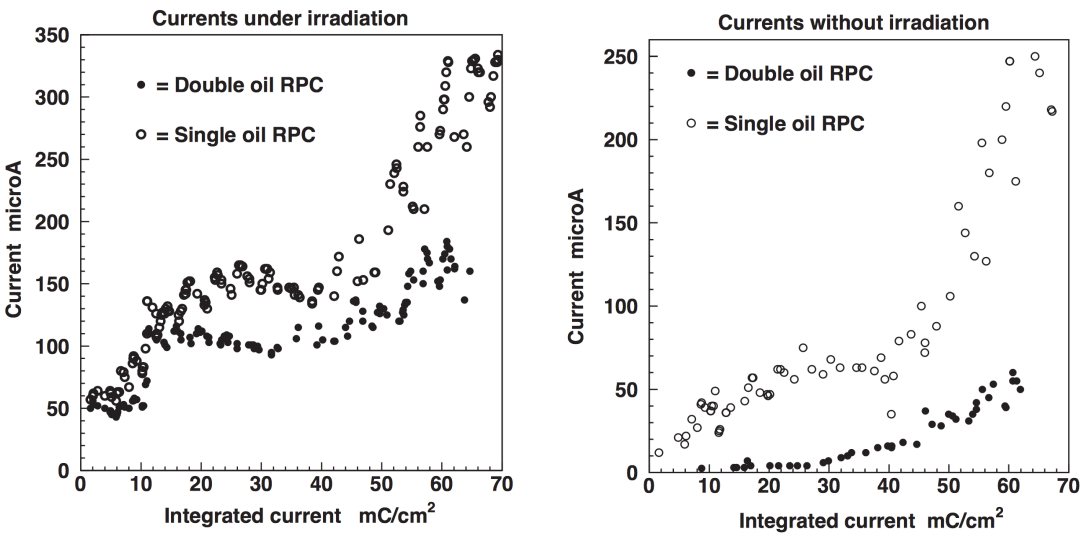

FIGURE 2.4 Current trend over time for single side oil coated and double oil coated RPCs. From [12].

electrically decouple the internal electrodes and the pick-up strips. The readout pads or strips are installed outside the insulation layer. The edge of the chamber is sealed by means of plastic material walls and is equipped with pipes for the flow of the gaseous mixture.

The gaseous mixture of a RPC is not standard and each implementation can differ from any other one. However, some basic ingredients can be identified :

— Donor gas : (*e.g.* Ar) it is the gas that should be ionized by the ionizing particle and which provides amplification of the deposited charge via secondary ionisation ;

— X-ray quencher : (*e.g.* $i-C_4H_{10}$) it is a gas that has an high cross section for x-rays and high energy photons. This is needed in order to absorb recombination photons that can cause a degeneration in streamer ;

— Charge quencher : (*e.g.* SF_6) it is a gas that provides high electro-negativity in order to limit the transversal development of the avalanche and reduce the probability of a streamer degeneration.

Depending on whether the RPC is chosen to operate in avalanche or streamer mode (Fig. 2.2) the gas mixture should be modified. For example a streamer mixture is mainly composed of Argon, while in avalanche mixtures this is replaced by a gas which, along with acting as a donor, has also quenching properties (*e.g.* $C_2H_2F_4$).

Several aspects, such as the gas mixture composition, enter the definition of an RPC HV working point. Typically this voltage is chosen by performing an efficiency versus voltage scan of a specific RPC, and might differ from one RPC to another. Apart from the detection efficiency, other aspects are important and should be considered when selecting the working

point of an RPC. A dependence between the supplied HV and the distribution of the cluster sizes (namely the number of adjacent strips fired by a single particle) has been observed, hence while the efficiency arises when raising the HV, the spatial resolution might be affected. Another aspect related to the HV value is the signal amplitude and the total charge deposed in the gas gap by a ionizing particle. The choice of the RPC gas mixture and HV is strictly connected to the characteristics of the front-end electronics (FEE) used for the read-out. The required signal amplitude is defined by the minimum threshold that can be set in the FEE, which in turn depends on the FEE's noise level. In some applications, the usage of FEE cards with an amplification stage allows for low-gain operation [59].

2.2 Ageing effects in RPC detectors

Like other gaseous detectors, the gas gap of the RPCs can undergo during long-term operation reversible and irreversible performance degradation.

The most important source of performance degradation is the amount of charge generated in the gas gap during irradiation at nominal voltage. The avalanche (or streamer) process can directly harm the electrodes or, more frequently, induce the generation of chemical compounds other than the gas mixture components. These compounds might form deposits on the inner surfaces of the gas gap, creating peaks which can affect the chamber noisiness, as well as they can chemically attack the surfaces. Both these situations can cause an increase of the noise rate of the chambers. An high noise rate causes a local inefficiency of the detector due to the recovery time after a discharge. These processes can be mitigated by special measures. Besides the already mentioned oiling of the inner surface of the electrodes, another common practice is the usage of a humid gas mixture. Indeed, one of the risks for bakelite-made RPCs is the mechanical deformations and the resistivity variations caused by the drying of bakelite layers. The humidification of the gaseous mixture allows one to constantly hydrate the inner surface of the bakelite electrodes, keeping the original gas gaps shape and avoiding changes of the bakelite resistivity (see Fig. 2.5).

The "age" of a RPC detector is frequently quantified by means of the integrated charge per unit surface (mC/cm^2). Detectors are ageing tested at high-intensity photon sources to simulate the effect of long-term operation.

Along with the efficiency of the detector, two among the most important parameters to be monitored to assess ageing are the dark current and the dark rate, *i.e.* the current and counting rate of the detector at nominal high voltage in absence of beam. These quantities are expected to be sensitive to the quality of the inner surface of the electrodes, as the presence of spikes or dips may enhance electron extraction from the cathode and consequent development of

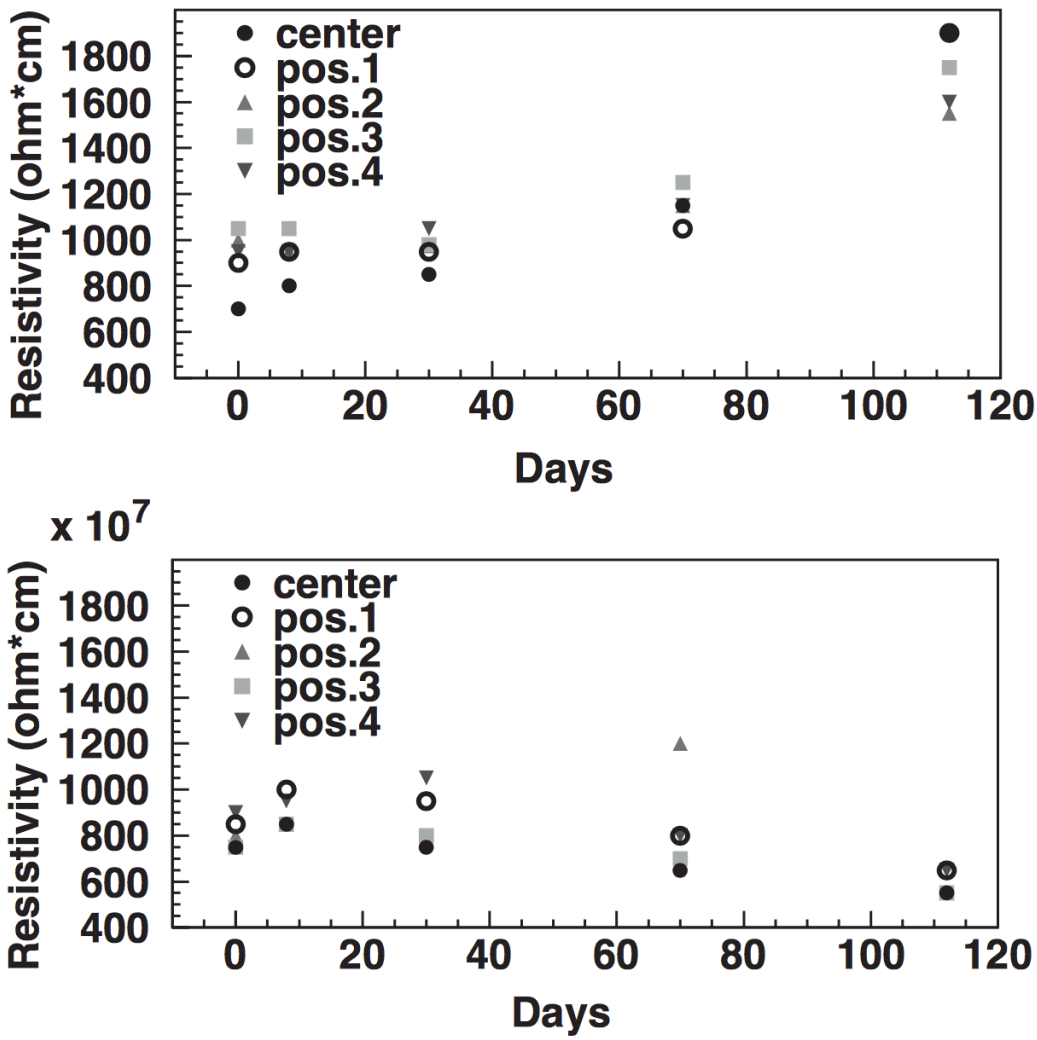

FIGURE 2.5 Resistivity trend over time for prototype ALICE RPCs. In the top panel a chamber provided with dry gas mixture is shown, while in the bottom panel the gas mixture is humidified. Different marker styles correspond to different testing positions. From [12].

an avalanche or streamer. Moreover, the dark current is sensitive to ohmic effects due to non-perfect insulation of the HV plate from the rest of the system.

In the second part of this chapter, the framework developed for the monitoring of the parameters mentioned above for the RPCs of the ALICE muon trigger will be described.

2.3 The ALICE muon trigger RPCs

The ALICE muon trigger system is made of four layers (MT11, MT12, MT21 and MT22) arranged in two stations spaced of 1.2 m, as shown in figure 2.6. Each layer is divided in two half-planes, inside LHC ring and outside LHC ring (INSIDE and OUTSIDE in the following). Each of the four layers is composed of 18 RPCs. The chambers of the first two stations are slightly smaller than the ones of the third and fourth in order to cover the same pseudorapidity range. Three types of RPC with different shapes are installed and correspond to long, short and cut shapes. The short and cut shapes are intended to leave the necessary clearance for the beam pipe. The muon trigger RPCs are made of 2 mm wide gas gaps with 2 mm thick bakelite resistive electrodes and polyammide insulation layers. The readout strips are copper made and their pitch can vary among three values : 1, 2 or 4 cm. All the RPCs are equipped with one set of readout strips per side. The strips of each side of the RPCs are reciprocally orthogonal. The vertical (horizontal) strips, providing x (y) hits, are called non-bending (bending) in relation to the dipole action on charged particles paths. The currently installed front-end electronics is called ADULT and is not amplified [60]. 71 RPCs are equipped with this electronics, while one RPC is equipped with a prototype of the FEERIC electronics [59] that provides an integrated amplification stage. The ALICE muon trigger RPCs (and the ADULT electronics) were initially developed for streamer mode operation [61]. Later on, a second operation mode ("maxi-avalanche") was developed [62], where the signal amplitude is smaller than in streamer mode, but still compatible with the minimum threshold ($\approx$ 7 mV) that can be set in ADULT. The beam test performed in maxi-avalanche mode showed a rate capability (*i.e.* the maximum irradiation rate that can be reached without efficiency degradation due to the local voltage drop) of about 80 Hz/cm^2. Moreover, prototypes were ageing-tested at the CERN Gamma Irradiation Facility up to an integrated charge of about 50 mC/cm^2. The gas mixture corresponding to such an operation mode is :

— 89.7% Tetrafluoroethane ($C_2H_2F_4$) ;
— 10.0% iso-Buthane ($i-C_4H_{10}$) ;
— 0.3% Sulfum esafluoride (SF_6).

As will be discussed in Chapter 4, the ALICE experiment will undergo a major upgrade before the LHC RUN3 (expected to start in 2021), where the instantaneous luminosity in Pb-Pb collisions will increase by almost one order of magnitude. In light of this, the FEERIC electronics was developed. The goal is to lower the HV and operate the detectors in pure avalanche mode, transferring the gain from the gas to the electronics, decreasing the deposited charge per hit by about a factor 4 and hence improving the rate capability and reducing the impact of ageing effects. Since the beginning of the LHC RUN2 (2015) one RPC is equipped with FEERIC, in order to test in real life the expected performance

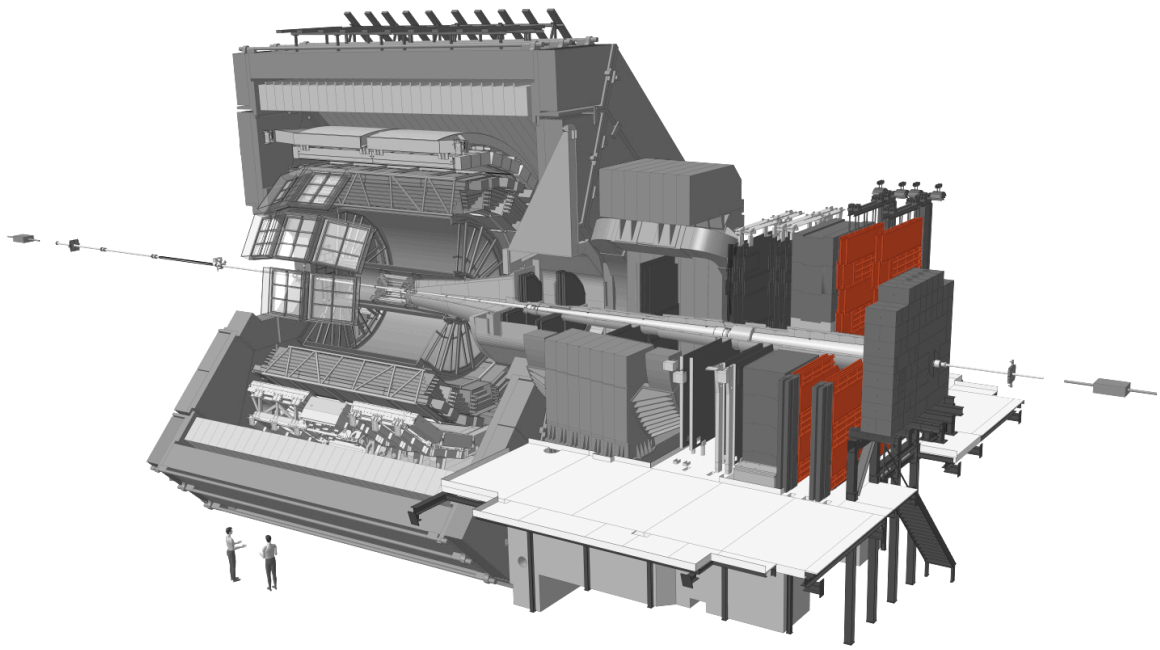

FIGURE 2.6 Grayed out ALICE with highlighted muon chambers and muon trigger chambers.

improvement. The working point of the ADULT-equipped RPCs is about 10200 V, while for the FEERIC-equipped RPC the working point is about 9500 V, *i.e.* 700 V lower than with ADULT. During the operation the variation of the atmospheric temperature (T) and pressure (P) results in a variation of the efficiency. This effect can be corrected for by dynamically adjusting the high voltage according to the formula :

$$HV = HV_{nom} \cdot \frac{T_0}{T} \cdot \frac{P}{P_0} \tag{2.1}$$

where HV_{nom} is the working point quoted above, $P_0 = 970$ mbar and $T_0 = 293.15$ K.

2.4 MTR monitoring data sources

The ALICE experiment is equipped with a complex safety and hardware monitoring system called Detector Control System (DCS). This system is the interface that allows to remotely control the detector, modifying the value of the high voltage, power supply and electronics statuses of the detectors. In addition to the interface role, the DCS is connected to a database which records the readings of all the sensors related to devices handled by the DCS. For what concerns the MTR, the DCS is able to record, for each chamber, the

current, HV and LV voltage and thresholds used for the electronics, as well as global gas flow, humidity and composition values. The read-out values are stored in a DCS database which can be accessed using custom Siemens WinCC applications in order to produce plots and trends for several variables over time. The data points are saved in the DCS database following two guidelines. First of all the values are stored in the database whenever a given threshold on percent variation, with respect to previously stored value, is passed. Additionally a slow clock (5 minutes) triggers the storage of the current read value, in order to keep track of smaller variations as well as of the stability of a given system. The DCS values are accessible through a web interface called DARMA (formerly AMANDA) by executing database-like queries and downloading structured text file.

Some DCS information has to be available offline in order to perform offline reconstruction and simulation of the ALICE apparatus. A database, the Offline Conditions Data Base (OCDB), stores all the calibration and alignment data for such purposes. A connection channel between the DCS infrastructure and the OCDB allows for the storage of the DCS readings during data taking. This allows one to keep a track of the working conditions of the detectors, as well as of all of the information on the status of data taking, beam, etc. that are necessary to the reconstruction or to the realistic simulation of the detector. All the data collected by ALICE is stored on the storage elements of the computing GRID. In order to provide this access flexibility, the OCDB uses some parameters stored as file meta-data. The data taking is organized in runs, periods of time of arbitrary length in which the detectors and accelerator conditions are considered to be stable. The storage of information in the OCDB follows the same pattern. The OCDB allows for the storage of DCS reading only during data taking runs, in which at least one of the ALICE's detectors are being read out.

2.5 MTR integrated charge measurements

As already stated the ageing of RPCs is assumed to be proportional to the integrated charge liberated in the gas gap, mostly via the chemical action of compounds created in the avalanche or discharge process. The ALICE muon trigger RPCs have been ageing-tested up to a total integrated charge of 50 $\mathrm{mC/cm^2}$. It is interesting to compare such a value with those reached after years of operation at the LHC. The integrated charge is obtained by time-integration of the current flowing through the detector. To this respect, the gas gap of an RPC sees a current flow which has four components (Eq. 2.2) :

— Ohmic component : it is due to the low conductivity of the gas gap and of the structure of the chamber. This part of the current depends linearly on the applied voltage ;

— Environmental irradiation : natural or activated radiation sources of ionising radiation, as well as cosmic rays detected by the RPC ;
— Noise-induced current : due to spontaneous discharges in the gas gap following electron extraction from the cathode surface ;
— Physics-induced current : caused by ionizing particles produced in physics collisions.

$$i_{tot} = i_{ohm} + i_{env} + i_{noise} + i_{phys} \tag{2.2}$$

The ohmic, environmental and noise-induced components are always present, in case the detector is kept at the nominal working voltage. The fourth component of the current depends on the operations of the LHC and the collision luminosity. From an aging point of view the ohmic current is not expected to have an effect on the detector ageing, as it is not associated to the liberation of charges in the gas, then it should not be taken into account in the computation. The environmental current is always present and can cause aging effects, but its entity is negligible. The noise-induced current is relevant for aging effects.

A detector might be switched on and fully operational when no data taking is being performed, for example, between one run and the following one or when no beam is provided by LHC and ALICE is taking cosmic data. In this kind of situations the amount of current flowing through the system corresponds to the sum of the ohmic contribution and the environmental and noise-induced ones. Measuring the amount of current flowing in a chamber in these conditions would provide a measurement of the dark current i_{dark}, defined as :

$$i_{dark} = i_{env} + i_{ohm} + i_{noise} \tag{2.3}$$

Given that i_{env} is negligible, it can be removed, obtaining a measure of the dark current :

$$i_{dark} \approx i_{ohm} + i_{noise} \quad for \quad i_{env} \to 0 \tag{2.4}$$

Ideally, to obtain a precise evaluation of the current causing aging of an RPC, one should integrate :

$$i_{net} = i_{env} + i_{phys} + i_{noise} \tag{2.5}$$

Since it is not possible to extract i_{ohm} from i_{dark} two extreme approaches are possible, assuming the i_{dark} value can be dominated by either of its terms. If $i_{dark} = i_{ohm}$ the dark current contribution to i_{tot} must be subtracted to obtain the value of i_{net} which causes aging effects, hence $i_{net} = i_{tot} - i_{dark}$. If $i_{dark} = i_{noise}$, its contribution to i_{tot} may take part in aging effects, hence $i_{net} = i_{tot}$.

In either cases, the integration of i_{net} over time will provide the aging index that can be compared to the limit value obtained in the tests. The newly introduced framework allows for both approaches. All the integrated charge shown in this thesis have been obtained assuming $i_{dark} \approx i_{ohm}$.

The above-mentioned measurements are not possible using OCDB as the only data source. In fact the OCDB polls DCS readings and stores them permanently only when data taking is being performed. Even if this condition can happen both with beam collisions and during cosmic runs, the coverage of the dark periods of the MTR is partial.

The work presented in this chapter was originated from the idea of combining OCDB and DCS measurements using the well established OCDB data retrieving interface and the AMANDA/DARMA DCS database access tool, in order to increase the working conditions coverage with respect of the OCDB-only approach. In addition the granularity provided by the DCS is much better with respect to the one of the data propagated to the OCDB, but the DCS readings have no run number, beam condition or LHC status information. By combining the two data sources a better understanding of the MTR performances would arise, giving the possibility to perform trend and distribution studies, as well as correlation studies between MTR parameters and external conditions such as collisions luminosity.

2.6 MTR performance analysis framework

As a subject of this thesis a brand new analysis framework for MTR performance analysis has been developed. This framework main task is to combine the data coming from OCDB and AMANDA/DARMA in order to create a complete set of data which can be used for specific studies of trends and correlations concerning the MTR system. As an additional value to this project, the framework aims at providing a reliable tool which is accessible and open source. Having a centralized repository, with the possibility for any collaborator to participate to the development of the framework and to the fixing of eventual software bugs, can improve both the user experience and the number of users hence the bug detection capability.

The framework internal data format is filled on a per-run basis, and contains the following information :

— Run number : identifies the current run ;
— Start and End of Run (SOR and EOR) : Are the timestamps defining the data taking inside a run ;
— Average HV : average value (weighted over time) of supplied HV. One value per each of the 72 RPCs ;

— Average i_{tot} : average value (weighted over time) of supplied current. One value per each of the 72 RPCs ;
— Average i_{dark} : average value (weighted over time) of dark current, extrapolated via the algorithm. One value per each of the 72 RPCs ;
— Integrated charge : integral of the i_{net} over the run. One value per each of the 72 RPCs ;
— Bending scalers : total number of hits on the bending plane of the chamber. One value per each of the 72 RPCs ;
— Non-bending scalers : total number of hits on the bending plane of the chamber. One value per each of the 72 RPCs ;

The algorithmic steps performed to obtain the i_{net} values over time are :

1. DCS i_{tot} and HV data points are retrieved ;
2. OCDB data regarding beam conditions, HV readings and scalers values are stored ;
3. Current readings are flagged as "dark" using the OCDB information about beam presence. See schema in figure 2.7 ;
4. A linear interpolation of all the i_{dark} values is performed. For all the non-dark current readings the value of i_{dark} is set using the interpolation of dark current values. See schema in figure 2.8 ;

The framework has been extensively tested and the plots presented in the following sections of this thesis have been produced by means of the new framework, merging the two available data sources for the first time.

2.7 Determination of dark current and dark rate and dark current interpolation procedure

One crucial point is how to determine if a rate or a current reading are indeed "dark" readings. While the dark current definition has already been quoted in section 2.5, the dark rate definition is to be given.

The dark rate is the rate observed and measured in the same conditions as the dark current, i.e. at nominal HV and when no collision is taking place in the LHC. This rate should be correlated with the natural radioactivity and cosmic rays incidence, as well as intrinsic noise counts of the detectors, but may contain a contribution related to noisy read-out channels.

The dark runs can be defined in various ways. In order to properly flag the DCS current readings either as dark or not it was needed to select runs with no beam and nominal HV supply.

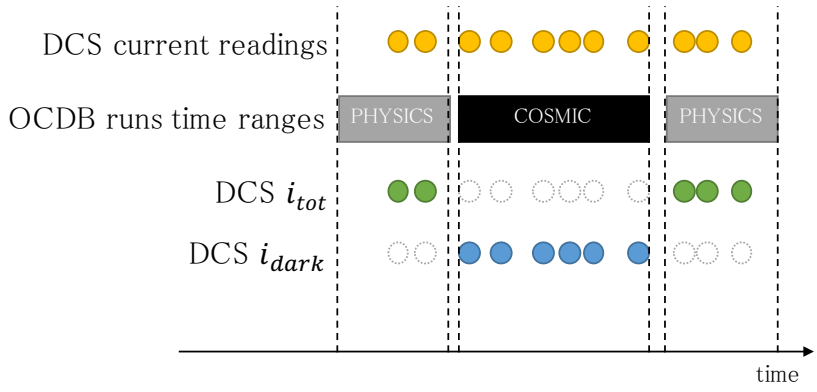

FIGURE 2.7 Cartoon representing the process of dark current readings flagging by combining OCDB and DCS data. The lines are represented on an arbitrary horizontal time axis. The first line represents the current readings stored in the DCS database. The frequency of those measurements is not fixed. The second line represents with boxes the duration of several runs. Gray boxes show physics runs, while the black box represents a run in nominal conditions without beam (cosmic run). The first line currents can be flagged either as i_{tot} if within a non-cosmic run or as i_{dark} otherwise. They are represented in the last two lines accordingly.

Selecting runs taken with physics setup without beam presence (flagged as "COSMIC") is the safest choice, but this kind of runs is less frequent and provides less coverage of the operation period.

Selecting calibration runs allows to better cover the operation period, since at least two calibration runs are performed at the end of every physics fill of the LHC. The CALIBRATION run refers to two kind of diagnostic run lasting for 2 minutes each. The first is a software-triggered read-out of the whole detector performed without collisions in the LHC, aimed at spotting noisy channels. During the second type of CALIBRATION run, the whole FEE is artificially stimulated and read-out in order to detect dead channels. Within a CALIBRATION run the detector is usually at nominal working voltage. However, they can occasionally be performed with a reduced HV and/or during the presence of beam in the LHC.

The dark current trend using cosmic runs only is displayed in figure 2.9. As for calibration runs, it was observed that the dark current measured immediately after a physics fill (which is when most calibration runs are performed) is systematically higher that that measured in “quiet” periods. The interpretation of this effect is that after a period of operation with beam presence some impurities stay in the gas gap for a while before being fluxed by the gas

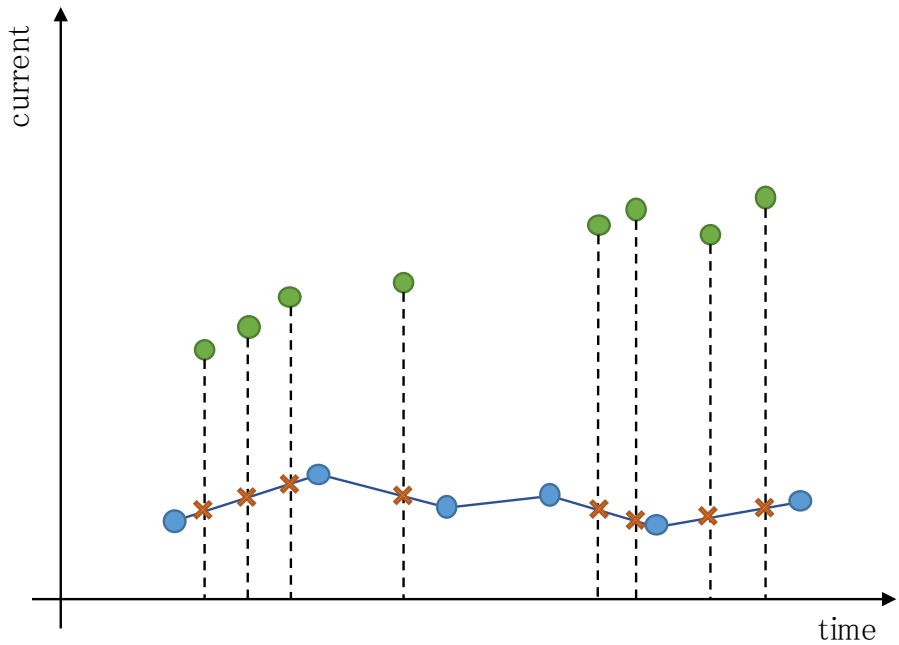

FIGURE 2.8 Cartoon representing the interpolation process. The green and blue points represent i_{tot} and i_{dark} readings, according to figure 2.7. The dashed vertical lines represent the projection on the time-axis of i_{tot} readings. The solid line connecting i_{dark} measurements represents the linear interpolation. The crossings between the i_{dark} interpolation curve and the vertical dashed lines, are the i_{dark} values attributed to i_{tot} measurements. Such values are highlighted with red crosses.

system. In order to avoid instabilities in the interpolation procedure due to this effect, only cosmic runs have been used to estimate the dark current and dark rate values.

A total of around 5200 cosmic runs have been used for this analysis. The scalers values are not stored in the DCS database, hence for the rate computation it is necessary to download OCDB information for all the runs performed with beam presence and collisions in the LHC. More than 12000 runs have been selected, covering pp, $p-Pb$, $Pb-Pb$ and $Xe-Xe$ colliding systems at all the center of mass energies provided by the LHC since the beginning of the operations.

2.8 Performance analysis

Several aging indicators for the 72 RPCs of the ALICE muon trigger will be presented and commented, trying to highlight eventual problematic RPCs which should be replaced. A

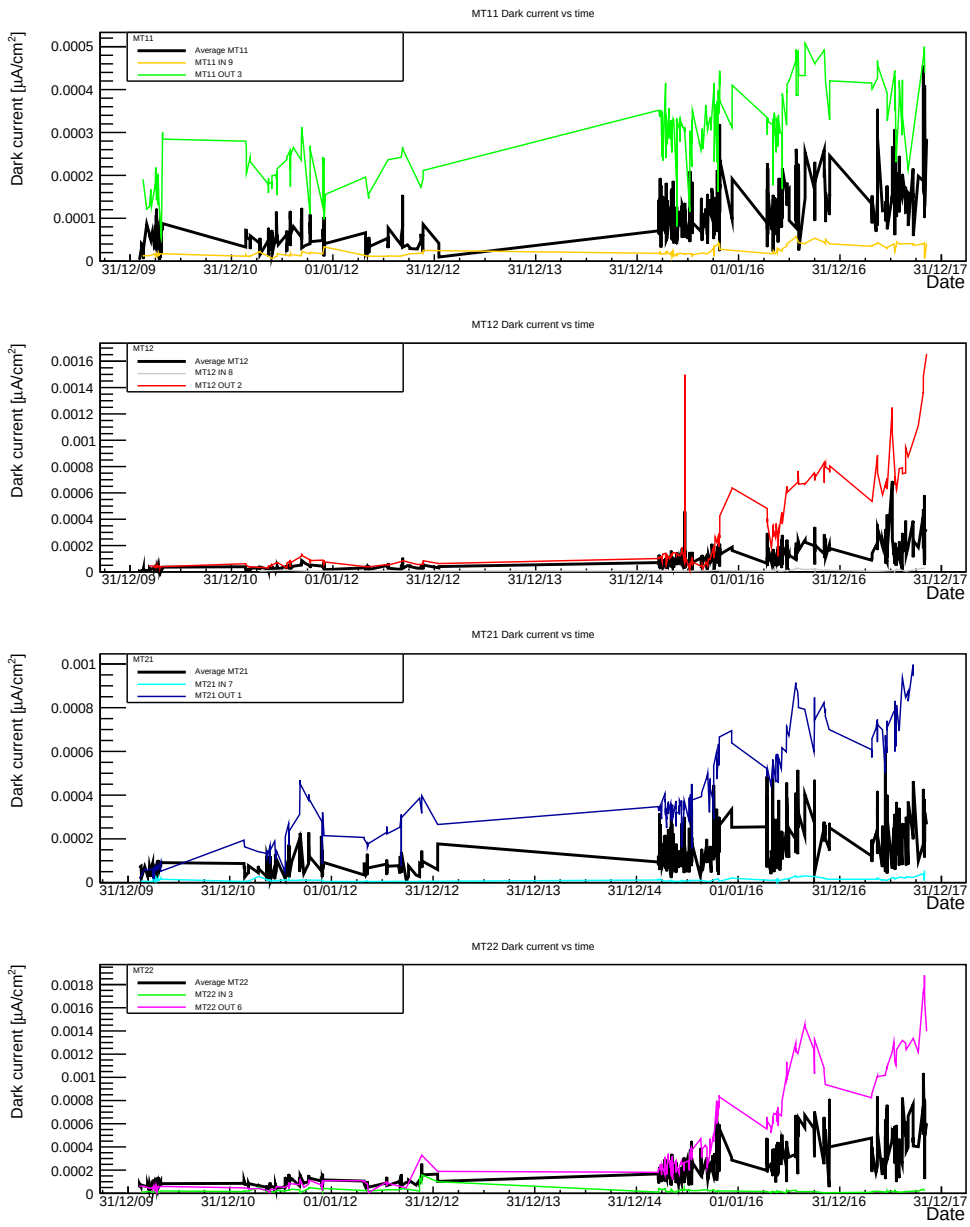

FIGURE 2.9 Average dark current trend computed with the described procedure using cosmic runs only. The trends are shown in four panels corresponding to the four detection planes (from top to bottom MT11, MT12, MT21, MT22). For improved readability for each plane only the maximum and minimum trends and the average plot are shown. Each point corresponds to a run. The y value is obtained via the average of all the RPCs dark currents, while the x value is the timestamp which corresponds to the end of run.

particular focus on the FEERIC-equipped RPC will address the main differences between the old and new read-out electronics from the chambers operations point of view.

2.8.1 Dark current trend

The evaluation of the dark current trend is fundamental to understand the health of the inner surfaces of the detectors. This working parameter strongly depends on the presence of irregularities on the boundary surfaces of the RPCs, hence can be used as a diagnostic tool. The dark current as a function of time for the 4 different RPC layers is shown in the four panels of figure 2.9. In each panel, the average dark current of the layer as well as the trend for the RPC drawing the largest and the smaller current in that layer are shown. The dark current measurements are reported in $\mu\mathrm{A}/\mathrm{cm}^2$, since dark current values have been divided by the corresponding RPC area. Given that the RPC areas are not all the same, this procedure helps to produce results which can be compared.

Sometimes a reduction of the dark current value can be observed. This effect is more important and clearly noticeable at the beginning of each year. It is commonly accepted that such a reduction of the dark current is caused by the yearly winter shutdown which undergoes for all the CERN LHC facilities. In fact every year the beam operations are stopped for a winter period which typically lasts from late November to the first 3-4 months of the following year. During this period the irradiation caused by the beam operations is absent. At the same time the gas flow through the chambers extracts impurities and eventually improves the inner surfaces smoothness. This recovery effect causes a reduction of the dark current and can systematically be observed for all the RPCs.

The trend shown in figure 2.9 covers four years of operations and includes the first LHC long shutdown period (LS1). A different trend before LS1 has been observed with respect to the one measured during RUN2. The dark current seems to raise during the RUN2 operations. The reason of such behaviour might be related to the much higher luminosity observed in RUN2, hence the stronger irradiation of the chambers causing longer recovery times. Comparing the specific trends of each RPC with the average trend one can easily observe that the increase of the average trend is mostly caused by some outliers. In fact 4 to 5 RPCs per plane, over a total of 18, show a dark current value large than the average trend. This behavior indicates that most of the RPCs present a much more stable behavior. The outliers of this trend can be considered the worst case scenario and should be monitored with attention in order to promptly notice eventual worsening of performances.

A detailed view of the dark current measurements for the FEERIC-equipped RPC are reported in figure 2.10. The dark current of the FEERIC RPC is negligible and in average a factor 20 lower with respect to the average. It is important to notice that while all the other

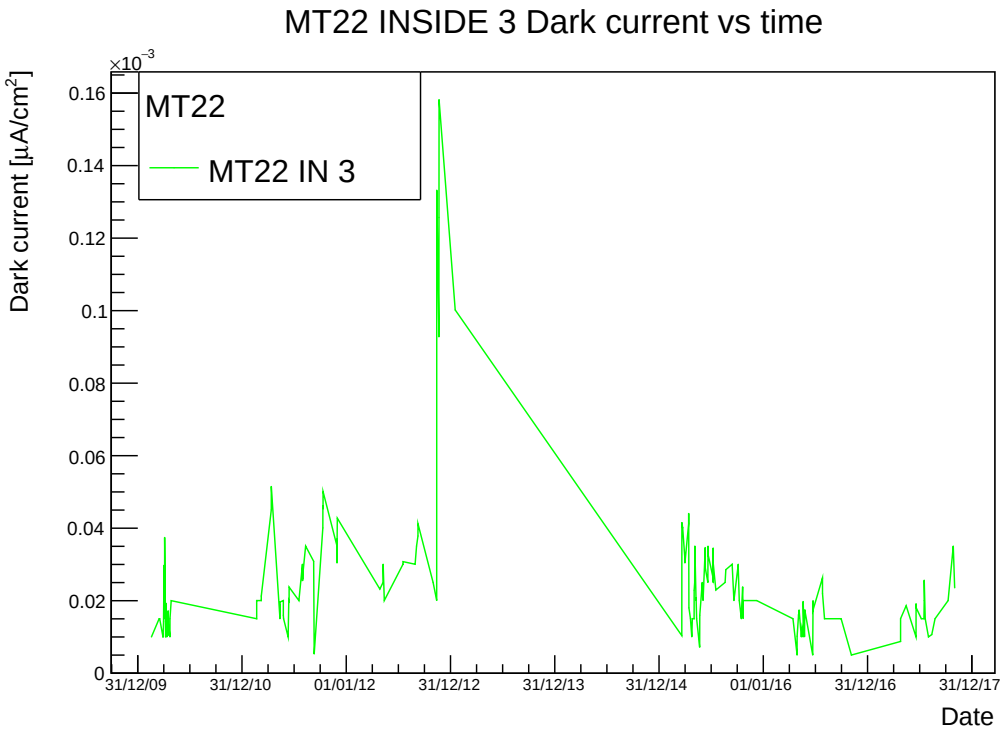

FIGURE 2.10 Dark current as a function of time for the FEERIC-equipped RPC. The FEERIC FEE has been installed in 2015, hence the first part of the plot refers to the same RPC equipped with the ADULT front-end. The dark current is measured during cosmic runs.

RPCs show an increase of the dark current over the years of operation, the measurements of dark current performed on the RPC equipped with the amplified electronics are compatible with a constant behavior.

2.8.2 Net current and integrated charge trend

This work presents for the first time a method to combine data from OCDB and DCS databases capable of subtracting the contribution of dark current from the evaluation of the integrated charge. In order to do that, the net current should be evaluated starting from the total current and the dark current readings, through the procedure presented in the previous sections.

The net current measurements are reported in figure 2.11 as a function of time (date). The panels correspond to the trends of MT11, MT12, MT21 and MT22 from top to bottom. In each panel, the average net current of the layer as well as the trend for the RPC drawing the largest and the smaller current in that layer are shown. The net current measurement

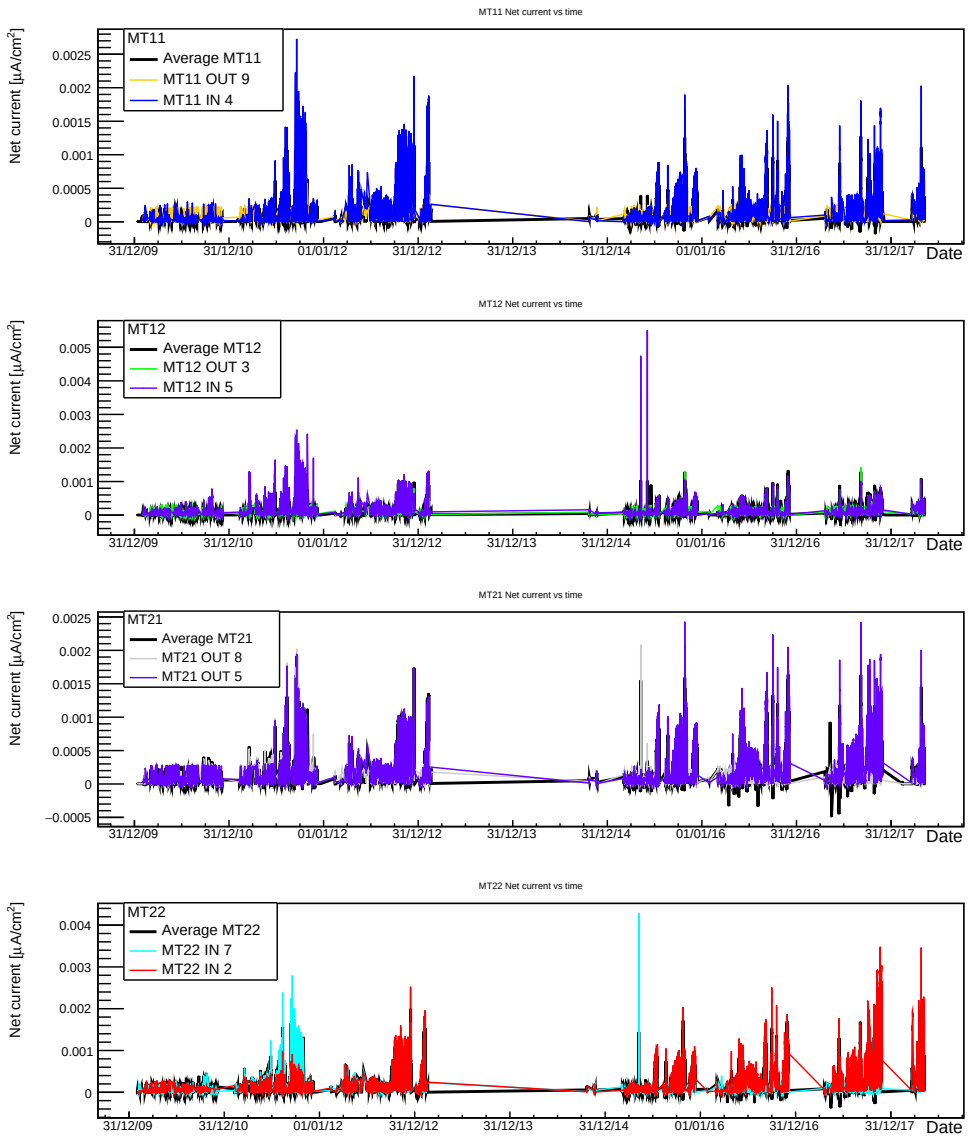

FIGURE 2.11 Net current trends for each RPC over the whole operation period. The trends are shown in four panels corresponding to the four detection planes (from top to bottom MT11, MT12, MT21, MT22). For each plane only the trends of the RPC with the maximum and minimum current are shown. Each point corresponds to a run. The y value is the difference between the average total and dark currents, while the x value is the timestamp which corresponds to the end of run.

represents the current related merely to the irradiation of the detectors, hence it is expected to have a baseline at 0 μA/cm^2 and increases with the intensity of the beam. The expected behavior is observed through the whole time range.

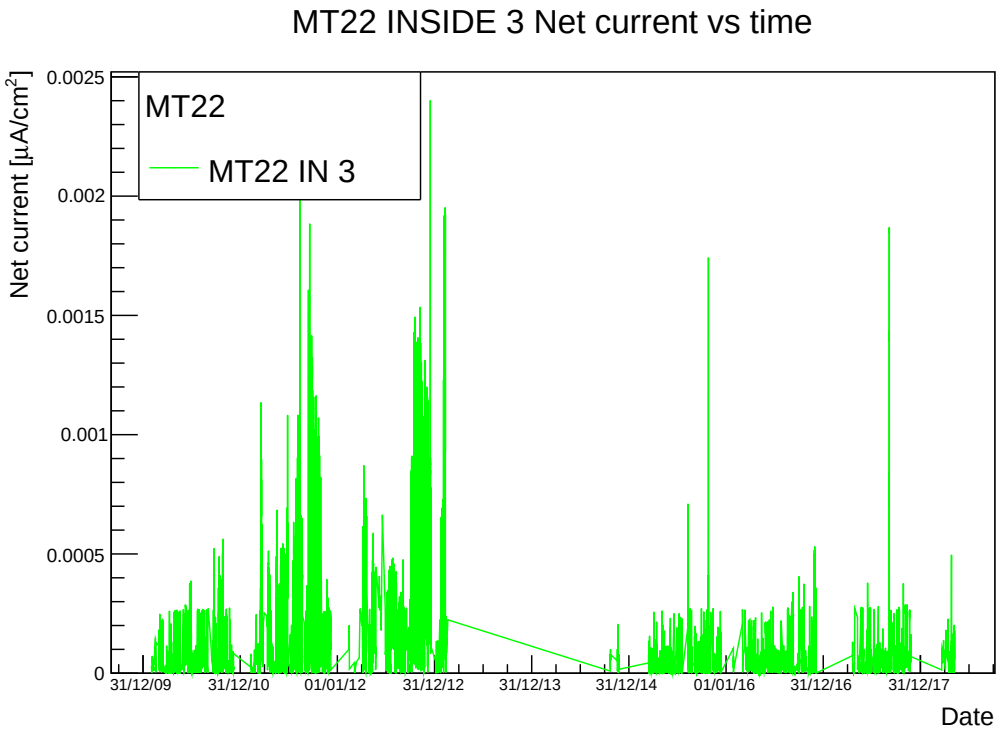

FIGURE 2.12 Net current as a function of time for the FEERIC-equipped RPC. The dark current is measured during cosmic runs, while the total current is measured during physics runs.

Concerning the FEERIC-equipped RPC, the net current measurements shown in figure 2.12 show a much lower current since 2015, when the RPC was equipped with FEERIC and the HV was lowered.

The net current plot has been integrated over time in order to obtain the integrated charge growth over time. The integrated charge can be estimated by integrating over time the currents of figure 2.11. The result is shown in figure 2.13, where MT11, MT12, MT22 and MT21 are plotted (from top to bottom). The time interval with a constant charge corresponds to periods with no collisions at the LHC.

The time series of one of the RPCs of plane MT12, shows a sudden drop of the integrated charge. This is due to the fact that the RPC was replaced with a new one during the operations and the integrated charge has been therefore consistently reset to 0 $\mu\mathrm{C}/\mathrm{cm}^2$.

A detailed view of the FEERIC integrated charge is shown in figure 2.14. The shape reflects the lowering of the net current shown before (see Fig. 2.12). An integrated charge about 6 times lower than the average for the MT22 plane has been collected since the installation of the FEERIC electronics.

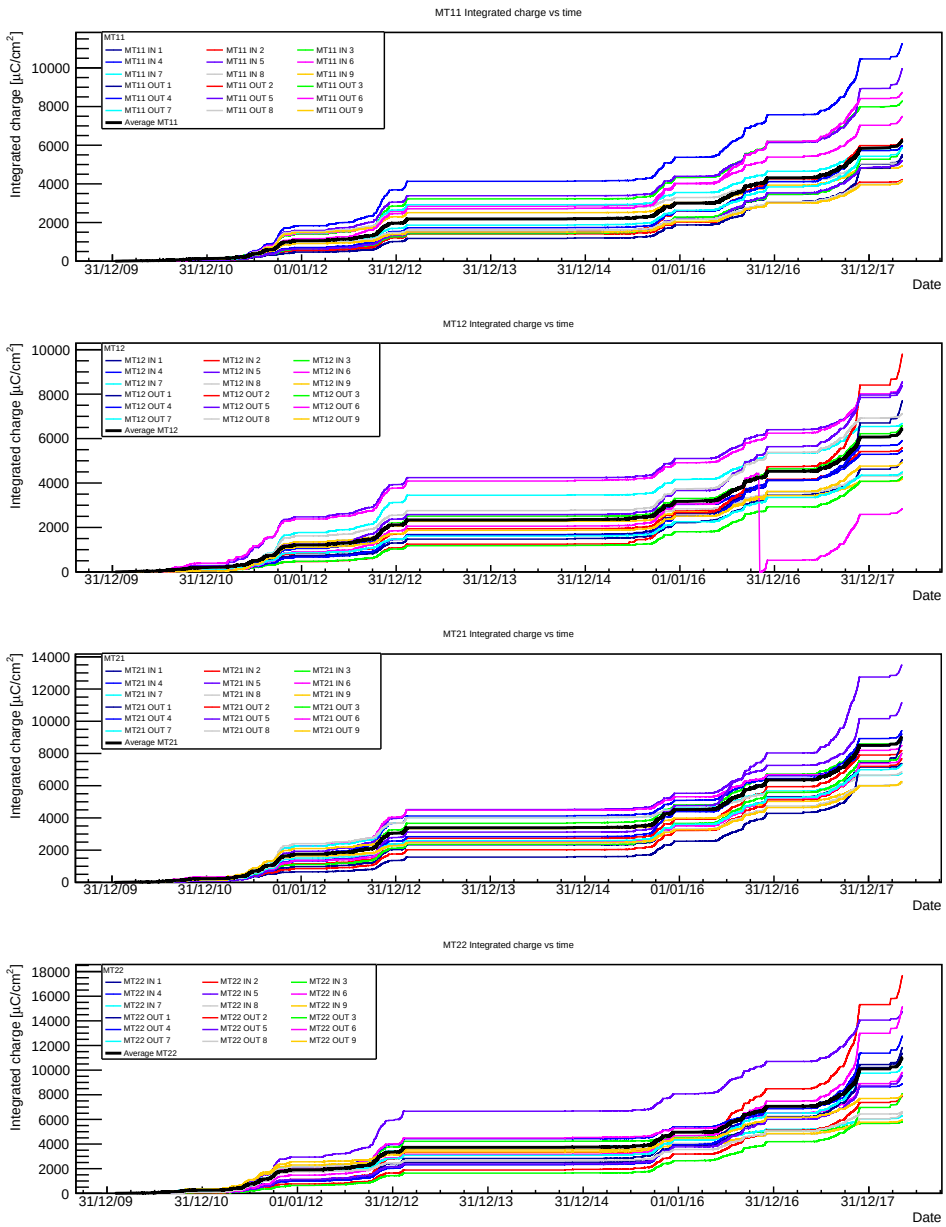

FIGURE 2.13 Integrated net charge for each RPC as a function of time. The 72 trends are divided by plane (from top to bottom MT11, MT12, MT21, MT22). For each plane the average plot is shown. Each point corresponds to a run.

The results for the integrated charge show that, at the end of the 2017 run, the average integrated charge is about 8 $\mathrm{mC/cm^2}$ (obtained by averaging the average values of the four planes), and the charge for the most exposed RPC is about 18 $\mathrm{mC/cm^2}$. This is comfortably far from the limit of 50 $\mathrm{mC/cm^2}$ reached in the ageing test. It is worth remarking that, when

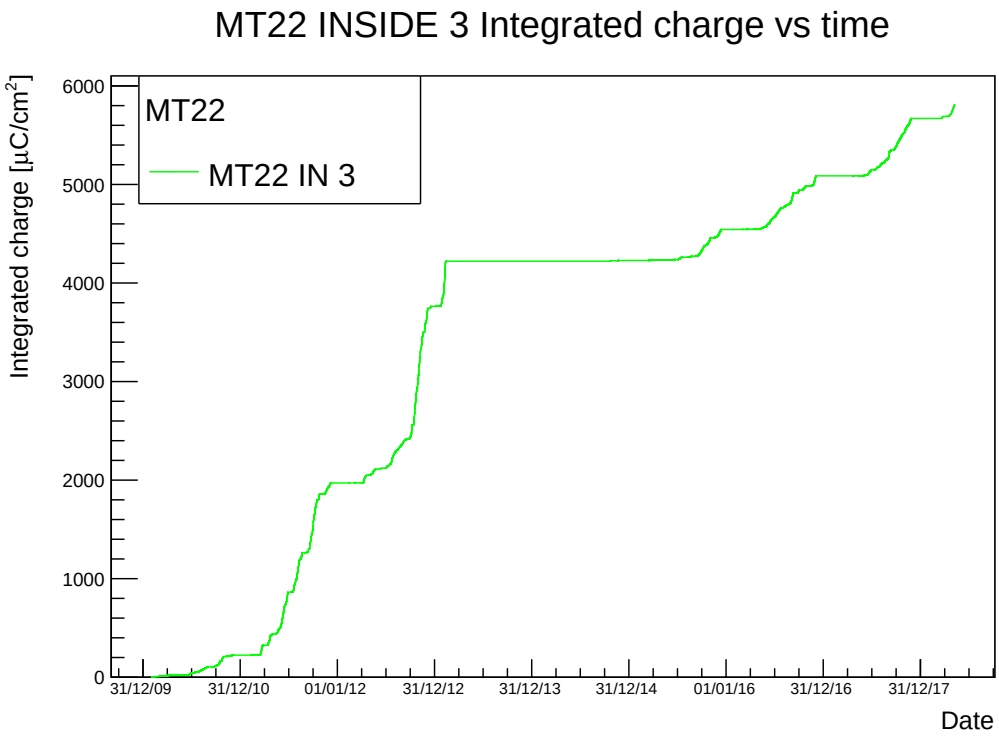

FIGURE 2.14 Integrated charge as a function of time for the FEERIC-equipped RPC. The y value is the integral of net current shown in 2.12.

the charge is integrated without subtracting the dark current (i.e.assuming that $i_{dark} = i_{noise}$) the results are larger by about a factor of two. Under this assumption, some RPCs may indeed be close to the end of their "certified lifetime". Specific tests are needed to disentangle the ohmic component of the dark current. A possibility will be to measure the ohmic current at low voltage (where no amplification is possible in the gas, hence the noise-induced current is suppressed), and extrapolate it to the nominal voltage.

2.8.3 Dark rate trend

The dark rate trend is shown in figure 2.15. The information which can be obtained from this set of graphs is complementary to that of dark current one. Observing an increase of the dark rate may be a symptom of aging. In fact the dark rate is defined as the rate measured when no beam is present in the LHC. The dark rate is then induced merely by environmental radioactive background or by spontaneous discharges in the gas gap. For this reason, assuming the environmental background to be constant, any modification of the dark

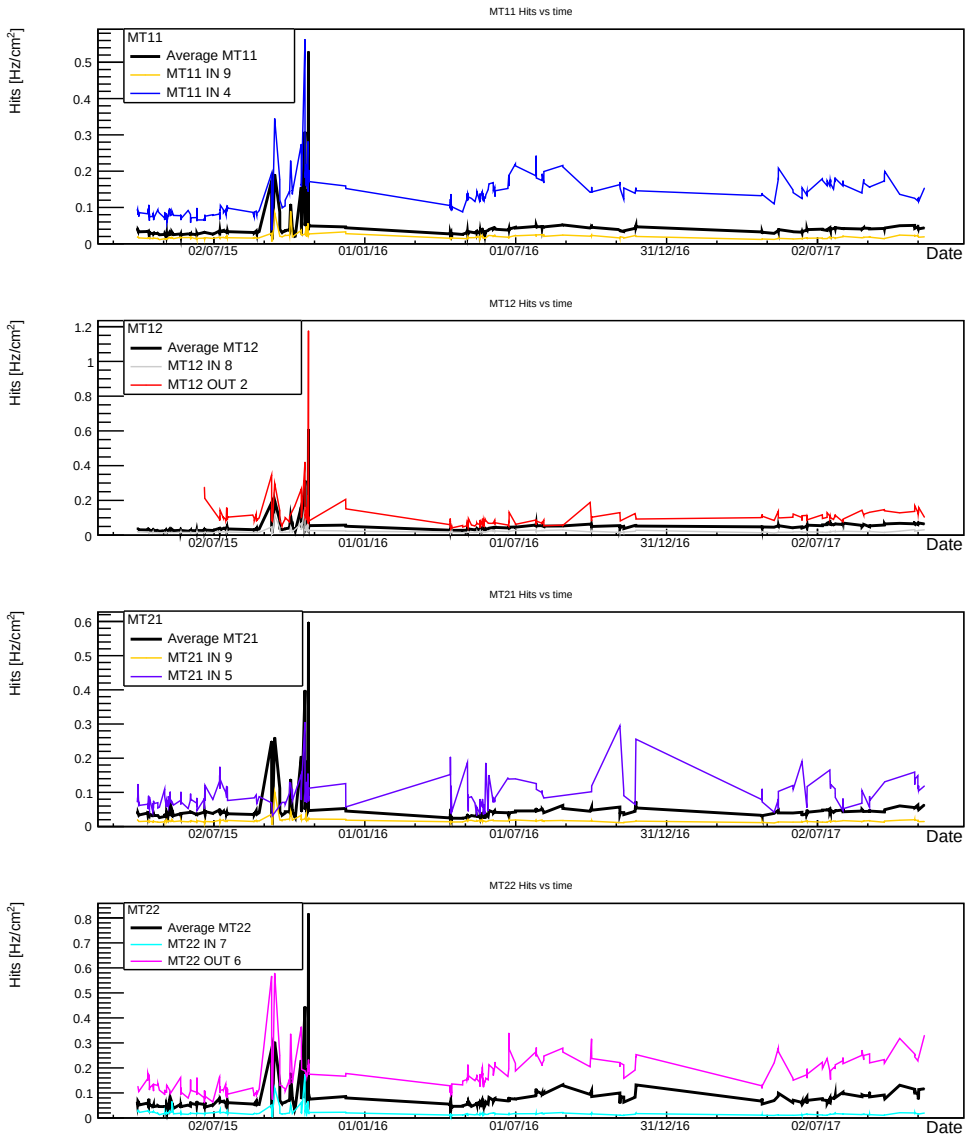

FIGURE 2.15 Dark rates trends for each RPC over the whole operation period. The 72 trends are divided by plane (from top to bottom MT11, MT12, MT21, MT22). For each plane the average plot is shown. Each point corresponds to a run. The y value is the average rate during a given cosmic run, while the x value is the timestamp which corresponds to the end of run.

rate is induced by physical modifications of the inner surfaces or, in general, of the RPC health.

In reality a variation of the environmental background should be taken into account. In fact right after the beam operations some activation of material close to the MTR may be

present. For this reason a temporary increase of the dark rate is foreseen, even if the beam is not present anymore. The signature one should look for is not a temporary increase of the dark rate, but a not complete recovery of the dark rate back to the level measured before a period with beam presence.

Analyzing the trends one can observe that some RPCs show a growth of the dark rate over the whole period of operation. Once again an average of 4 to 5 RPCs per plane (not shown in the figure) present a large dark rate, well above average. The chambers which show such behavior are the same that present an higher dark current with respect to the bulk of the RPCs. It is worth mentioning that, even if some outliers are found, most of the RPCs are still operating at the original level of dark rate after around 8 years of continuous operation. In that sense the dark rate trend is a good cross-check of the symptoms already detected with the dark current studies and the integrated charge ones. The affected RPCs have to be monitored to check their efficiency and to constantly ensure that their effectiveness as detectors is not being affected by the increase of the dark rate.

The dark rate trend for FEERIC is shown in figure 2.16. The dark rate trend is compatible with the average trend for the plane.

2.8.4 Correlations between rates and net current

The possibility to study correlations of different parameters was introduced with the new analysis framework. The correlations are valuable tools to provide a deeper understanding of the RPC. The correlation plot which allows to better understand the health of a detector is the one representing net current values correlated with measured rates.

The estimated net current of an RPC is expected to be proportional to the hit rate of the chamber itself. This proportionality is related to the charge deposited in the detector per each hit. The corresponding correlation can therefore easily highlight the presence of RPCs with abnormal discharge per hit. The correlation of the net current as a function of the hit rate during periods with collisions is shown in figure 2.17. One can observe that for most of the measurements there is a strong correlation between the net current and the estimated rate. The correlation however is not perfect, and, for a given rate, a dispersion of the net currents can be observed. Such deviations can in principle be due to different energies of the crossing particles as well as different crossing angles, resulting in different path length in the gas gap, or to an intrinsically different response of different chambers. They may also simply come from a bias in the calculation of the hit rate. This is calculated by summing up the rate of all strips, and no correction for the cluster size is possible. Such a bias depends on the segmentation of the read-out, hence it can be different for different RPCs.

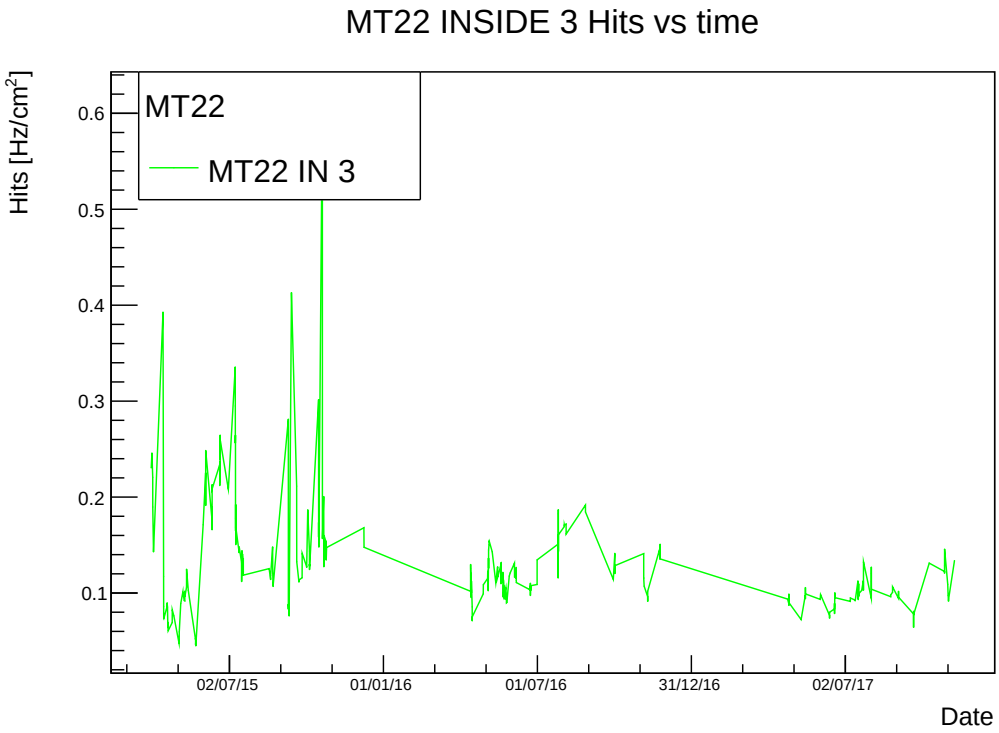

FIGURE 2.16 Dark rate trend for the FEERIC-equipped RPC. The y value is the average rate measured during a given run, while the x value is the timestamp which corresponds to the end of run.

The FEERIC-equipped RPC, located in MT22, shows a systematically smaller charge per hit. The slope of its correlation plot is much lower than that of the other RPCs of MT22 and results, as expected, in a lower deposed charge per hit.

2.8.5 Chambers efficiency

The new framework has been introduced for several reasons connected to the extension of the existing ALICE DCS Shuttle to more general use cases. The ALICE Shuttle is a framework capable of exporting data from the ALICE detectors and systems to the storage facilities. The conditions data may be parameters monitored and archived in the DCS and retrieved via a dedicated protocol, or outputs of dedicated detector-specific procedures [63]. One of the features that will be used in the future is the possibility to add other values to perform additional correlations. For example it is interesting to correlate aging effects to efficiency drops. The chambers efficiency measurements are not yet integrated in the framework presented here. It is however possible to show some efficiency studies to look for

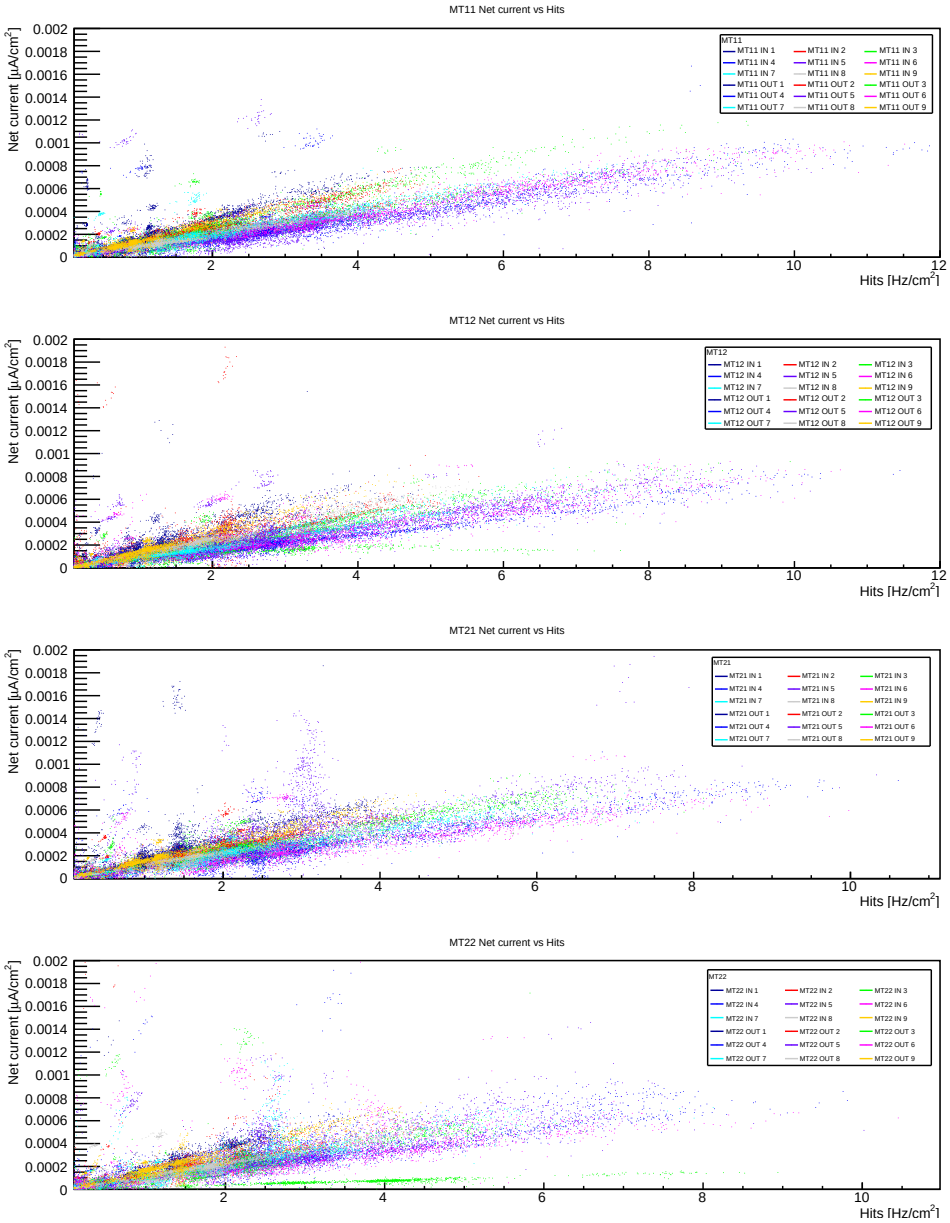

FIGURE 2.17 Correlation plot between net current and average rate within a given run. The 72 correlation plots are divided by plane (from top to bottom MT11, MT12, MT21, MT22). Each point corresponds to a run. The y value is the average rate during a given run, while the x value is the average net current value measured during the run.

an efficiency modification which could be qualitatively correlated with some of the aging indicators already presented. The efficiency trends from 2015 up to 2017 are shown in figures 2.18, 2.19, 2.20 and 2.21 for MT11, MT12, MT21 and MT22 respectively.

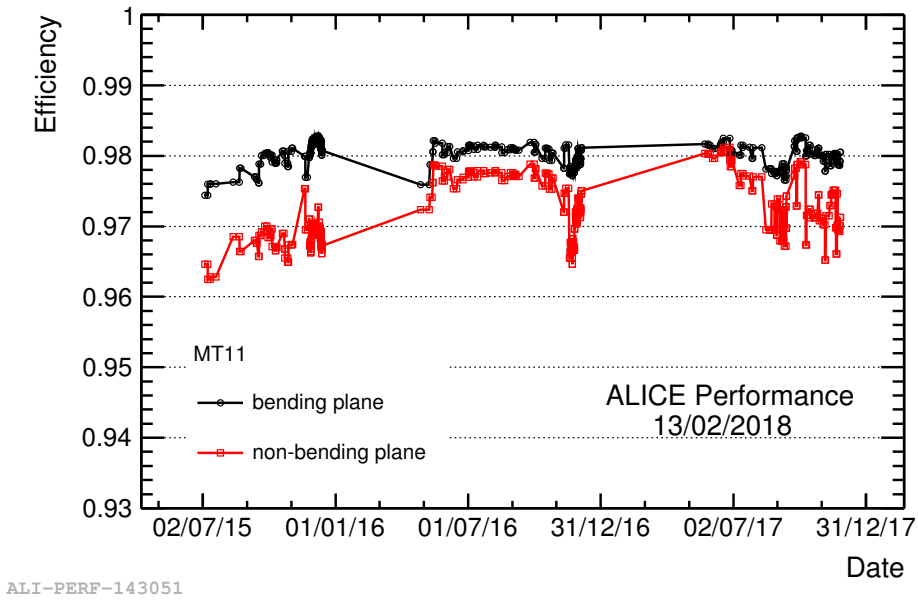

FIGURE 2.18 Average efficiency trend for MT11. Each point corresponds to a run. Bending and non bending planes are shown in black and red respectively.

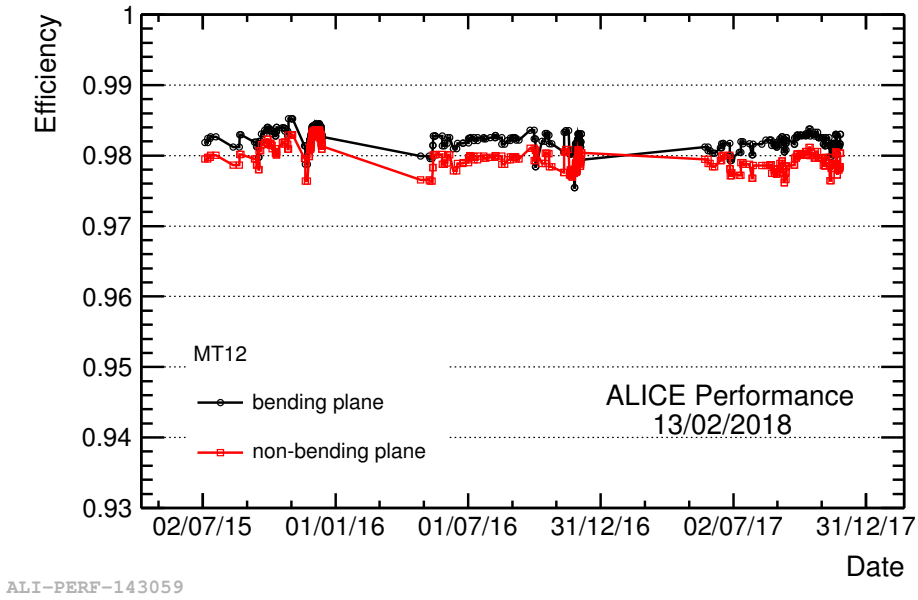

FIGURE 2.19 Average efficiency trend for MT12. Each point corresponds to a run. Bending and non bending planes are shown in black and red respectively.

The efficiency trend is generally stable over the whole period. The small variations observed (typically lower than 1%), are usually due either to the presence of (electronic) noise in the local boards of some of the RPCs or to the changes in the running conditions. The electronic noise seems to be mostly due to the connectors and can change with time, being often fixed with dedicated interventions on the local boards along the year. The drop of the efficiency of the non-bending plane of the FEERIC-equipped RPC is due to electronic noise in few local boards of this RPC appeared after the winter interventions between 2015 and 2016. Anyways, despite of these small fluctuations, no worsening of the performance has been observed moving from the "relaxed" conditions of RUN1 to the RUN2 higher luminosity levels.

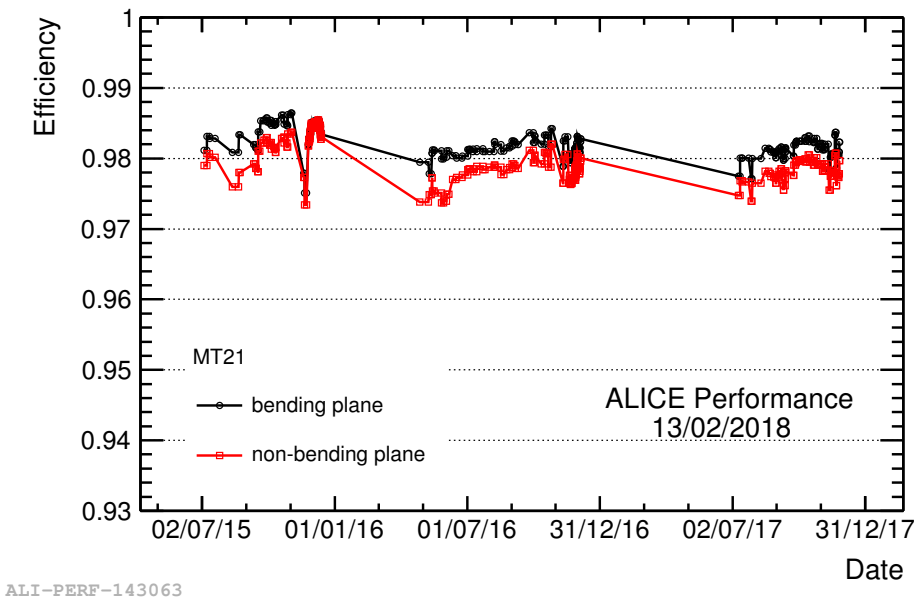

FIGURE 2.20 Average efficiency trend for MT21. Each point corresponds to a run. Bending and non bending planes are shown in black and red respectively.

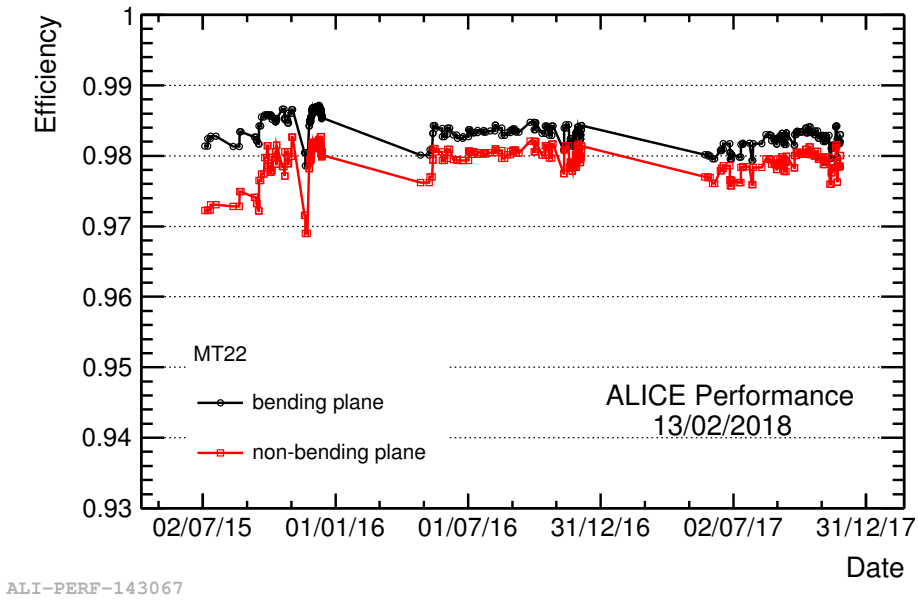

FIGURE 2.21 Average efficiency trend for MT22. Each point corresponds to a run. Bending and non bending planes are shown in black and red respectively.

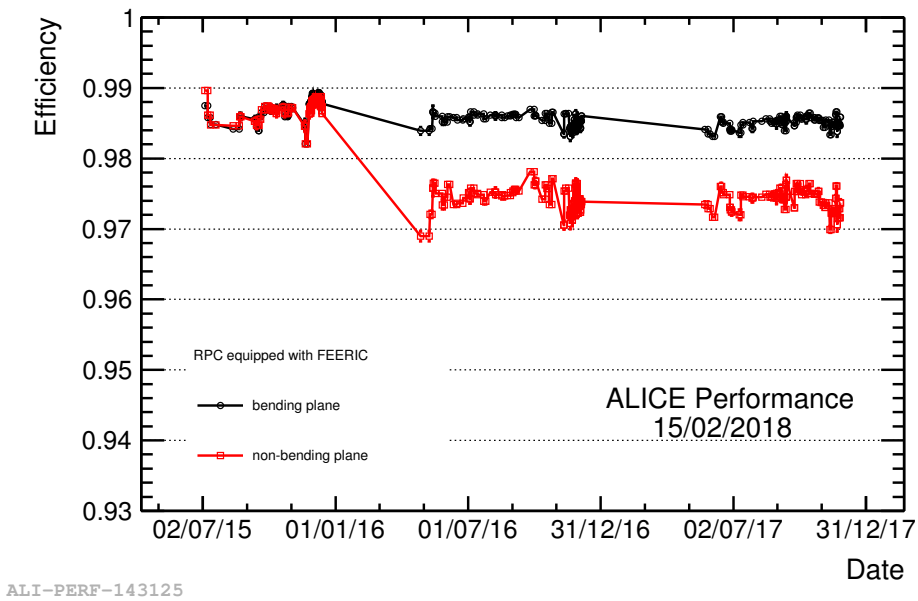

FIGURE 2.22 Efficiency trend for the FEERIC-equipped RPC. Each point corresponds to a run. Bending and non bending planes are shown in black and red respectively.

Chapitre 3

Study of bottomonium production in Pb-Pb collisions at $\sqrt{s_{NN}} = 5.02\text{TeV}$

3.1 Operational definition of nuclear modification factor

In order to study the modification of Υ production in Pb-Pb collisions at $\sqrt{s_{\text{NN}}} = 5.02$ TeV the evaluation of R_{AA} should be performed through an expression based on the one presented in 1.1.4 :

$$R_{\text{AA}} = \frac{N^{\Upsilon}}{\text{BR}_{\Upsilon\to\mu^+\mu^-} \cdot (A \times \varepsilon)_{\Upsilon\to\mu^+\mu^-} \cdot N_{MB} \cdot \sigma_{\text{pp}}^{\Upsilon} \cdot \langle T_{\text{AA}} \rangle} \tag{3.1}$$

where :

- N^{Υ} is the number of detected resonance decays to muon pairs, while $\text{BR}_{\Upsilon\to\mu^+\mu^-}$ is the branching ratio for the dimuon decay [64] ;
- The $(A \times \varepsilon)_{\Upsilon\to\mu^+\mu^-}$ factor is the product of acceptance and detection efficiency, specific for the Υ state under study ;
- N_{MB} is the equivalent number of minimum bias events used for the analysis, which will be extensively described in Section 3.2 ;
- $\sigma_{\text{pp}}^{\Upsilon}$ is the reference pp cross section and $\langle T_{\text{AA}} \rangle$ represents the nuclear overlap function, which is evaluated in different centrality classes using the Glauber model [3, 65].

3.2 Experimental apparatus and data sample

An extensive description of the ALICE apparatus can be found in section 1.4. This analysis is based on muons detected at forward rapidity ($2.5 < y < 4.0$) with a combination of detectors from the central barrel and the muon spectrometer [66].

In this analysis the reconstruction of the primary vertex has been performed using the Silicon Pixel Detector [8].

The Minimum Bias (MB) trigger is provided by the logical AND of the signals from the two scintillating array tiles of the V0 detector [67] and the signal in the beam counters.

The MB trigger is fully efficient for the studied 0–90% most central collisions. The V0 detector provides the centrality estimate through a Glauber model fit of the signal amplitudes [3, 65].

The Zero Degree Calorimeters (ZDC), given their capability of detection of spectator protons, neutrons and nuclear fragments, allowed for the rejection of events corresponding to an electromagnetic interaction of the colliding Pb nuclei [68].

The muon spectrometer covers the pseudorapidity range $-4 < \eta < -2.5$. The muon tracker and the muon trigger are the detectors devoted to the reconstruction and identification of the produced muons, respectively. The trigger condition used for data taking is a dimuon trigger. Thanks to the muon spectrometer geometry and to the presence of a dipole magnet, the electric charge sign of muons can be established at the trigger level, looking at the tracks bending direction. Further details are given in section 1.4.3 of this thesis. The adopted trigger is then formed by the logical AND of the MB trigger and the presence in the muon trigger of a pair of muons with opposite charge sign, each with a p_{T} larger than about 1 GeV/c ($\mu\mu - MB$ trigger). The number of equivalent Minimum Bias events can be then obtained as $N_{\mu\mu-MB} * F_{norm}$, where $N_{\mu\mu-MB}$ is the number of analyzed dimuon triggers and F_{norm} is the inverse of the probability to have an unlike-sign dimuon triggered sample in a MB event [37].

In addition, in order to perform the event mixing procedure by artificially combining uncorrelated unlike-sign muons into dimuons for background reduction, the single muon trigger has been recorded.

The data used for this analysis has been collected between October and November 2015, during the first Pb–Pb data taking campaign of the LHC RUN2. A total of 137 runs belonging to this period has been analyzed. In the present analysis the data sample corresponds to an integrated luminosity $L_{\mathrm{int}} \approx 225\ \mu\mathrm{b}^{-1}$ in the centrality interval 0–90%, that has been divided into four centrality classes : 0–10%, 10–30%, 30–50% and 50–90%.

3.3 Signal extraction

The signal yields are evaluated by performing fits to the $\mu^+\mu^-$ invariant mass distributions. In order to improve the purity of the dimuon sample a set of selection criteria has been applied to the muon tracks :

— Each track must have a transverse momentum $p_{\mathrm{T}} > 2$ GeV/c. The effect of this cut on the reconstruction efficiency is marginal ;

— Each track must exit the front absorber at a radial distance from the beam axis, R_{abs}, in the range $17.6 < R_{abs} < 89.5$ cm. This cut rejects tracks crossing the region of the absorber with the material of highest density, where multiple-scattering and energy-loss effects are large and affect the mass resolution ;

— A cut on product of the track momentum and the Distance of Closest Approach (DCA) between the track and the primary vertex. This additional selection reduces the contribution from fake tracks and tracks originated by beam gas collisions. This cut has been tuned to be $6 \times \sigma_{pDCA}$, where σ_{pDCA} is the resolution of this quantity.

An additional cut on the rapidity of each reconstructed μ pair is applied, rejecting the dimuons whose rapidity fell off the $2.5 < y < 4$ range, in order to remove dimuons at the edge of the acceptance region.

One of the most limiting factors for rare probes analysis is the signal-to-background ratio. The background affecting the bottomonium production measurement mainly consists of μ^+ and μ^+ pairs from the decay of uncorrelated particles (combinatorial background) and from the correlated decay of $c\bar{c}$ and $b\bar{b}$ pairs. Two approaches are then possible to extract the yields from the fit to an invariant mass spectrum :

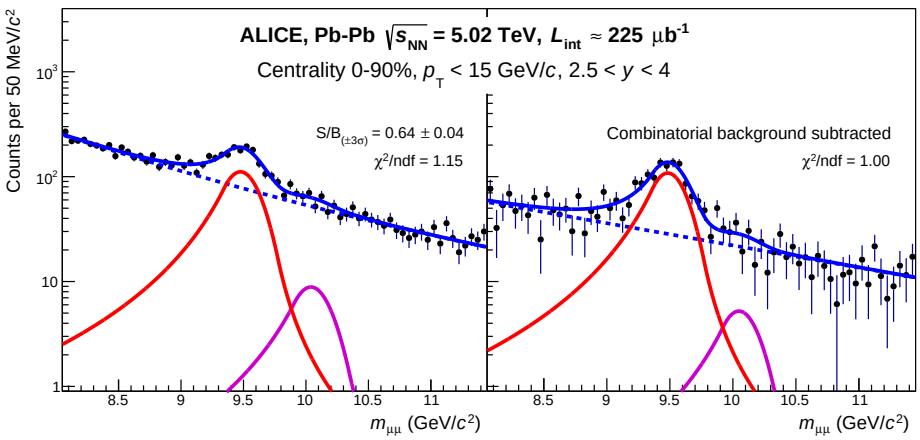

FIGURE 3.1 Dimuon invariant mass distribution (left) and combinatorial background subtracted distribution (right) in the mass region of bottomonium signals. Solid (dotted) lines correspond to signal (background) functions. The sum of the various functions is also shown as a solid line.

— Fit to the raw invariant mass spectrum obtained from data, where the background is modeled through a phenomenological function. In this case the fit has to be performed on the raw spectrum;

— Estimate the contamination of the combinatorial background through the event mixing method and subtract it from the raw yields. The remaining contribution is then fitted with a suitable function to extract the signal contribution. The event-mixing technique consists in filling a dimuon invariant mass spectrum with totally uncorrelated muons (*i.e.* from different events). Such procedure leads to an invariant mass spectrum that represents the combinatorial background of uncorrelated muons one should expect to lay under the measured dimuon invariant mass spectrum.

The signal component for Υ $(1S, 2S, 3S)$ in the invariant mass distribution are modeled using the sum of three extended Crystal Ball (CB2) functions [69]. The CB2 function consists of a Gaussian core with power-law tails, as shown in Eq. 3.2. The non-Gaussian tail in the low invariant mass region is due energy loss in the front absorber, while the high invariant mass one is due to residual alignment and calibration biases. Several parameterizations of the background have been adopted. When fitting the raw spectrum, the background has been modeled as both double exponential and double power law functions. In case the raw spectrum has been processed with the event mixing technique, the residual background has been taken into account using a single exponential shape.

$$f(x;N;\bar{x},\sigma,t_1,t_2,p_1,p_2) = N \cdot \begin{cases} A \cdot (B-t)^{p_1} & t < t_1, \\ -\exp\left(-\frac{1}{2}t^2\right) & t_1 < t < t_2, \\ C \cdot (D+t)^{p_2} & t < t_1 \end{cases} \tag{3.2}$$

$$\begin{aligned} t &= \frac{x-\bar{x}}{\sigma} \\ A &= \left(\frac{p_1}{|t_1|}\right)^{p_1} \cdot \exp\left(-\frac{|t_1|^2}{2}\right) \\ B &= \frac{p_1}{t_1} - t_1 \\ C &= \left(\frac{p_2}{|t_2|}\right)^{p_2} \cdot \exp\left(-\frac{|t_2|^2}{2}\right) \\ D &= \frac{p_2}{t_2} - t_2 \end{aligned} \tag{3.3}$$

Since the signal-to-background (S/B) ratio is low in the tail regions of the extended CB functions, the CB2 tails cannot be defined using a data driven approach. For this reason the tail parameters are fixed to values obtained from Monte-Carlo (MC) simulations. The mass position and the width parameters of the Υ(1S) are left as free parameters in the fit to the

integrated spectrum (*i.e.* centrality class 0–90%, $p_T < 15$ GeV/c and $2.5 < y < 4$). For the signal extraction as a function of centrality, the mass position and width of the Υ(1S) are fixed to the values obtained in the fit to the centrality-integrated (0–90%) mass spectrum. Some studies have been performed using the tail parameters obtained in pure MC simulation (GEANT 4) and embedded simulations (GEANT 3). Differential tails extraction has been performed using the simulated data, then the tails were adopted in the fits. The tail parameters were found to be quite stable with respect to y, p_T and centrality. The yield estimation variation has been measured to be of about 1% and 3% with respect to p_T and y respectively. Such uncertainty has been included in the signal extraction systematic uncertainty value. To perform studies as a function of p_T and y, the mass position and the width obtained for the centrality-integrated mass spectrum are scaled according to their evolution observed in the MC. Due to the even smaller S/B ratio for the excited states, the mass positions of the Υ(2S) and Υ(3S) are fixed to the PDG [70] mass differences with respect to the Υ(1S), and the ratio of Υ(2S) (Υ(3S)) to Υ(1S) widths is fixed to values from the MC simulation, *i.e.* 1.03 (1.06). In the fit shown in Fig. 3.1 only signals corresponding to the Υ(1S) and Υ(2S) are visible, since the Υ(3S) contribution turns out to be compatible with zero events.

3.4 Acceptance and efficiency correction

The extracted number of Upsilon must be corrected by the product of the acceptance and efficiency of the detector ($A \times \varepsilon$). This correction is needed to turn the raw spectrum into one that contains physics information. Acceptance and efficiency of each detector are evaluated through custom MC simulations. In particular the so called "embedded" simulations are used for this studies. In such MC simulations, the generated Υ is embedded in a real recorded event. This allows one to test the efficiency of detection of the simulated signal in a real event, with the full multiplicity observed in real data. This simulation can be used for efficiency studies as well as for the acceptance ones. Some inputs have to be provided to the MC generator. The simulation input consists of a parameterization of the bottomonium p_T and y distribution obtained by interpolating existing pp measurements [71–73] with the procedure described in [74]. The EKS98 nuclear shadowing parameterization [48] is used to include an estimate of CNM effects. Since available data favor a small or null polarization for Υ(1S) [75–77], an unpolarized production was assumed. The variations of the performance of the muon tracker and muon trigger systems throughout the data-taking period as well as the residual misalignment of the tracking chambers are taken into account in the simulation.

The $A \times \varepsilon$ values, for the range $p_T < 15$ GeV/c, $2.5 < y < 4$ and the 0–90% centrality class are 0.263 and 0.264 for the Υ(1S) and Υ(2S), respectively. A decrease of 0.02 is observed in

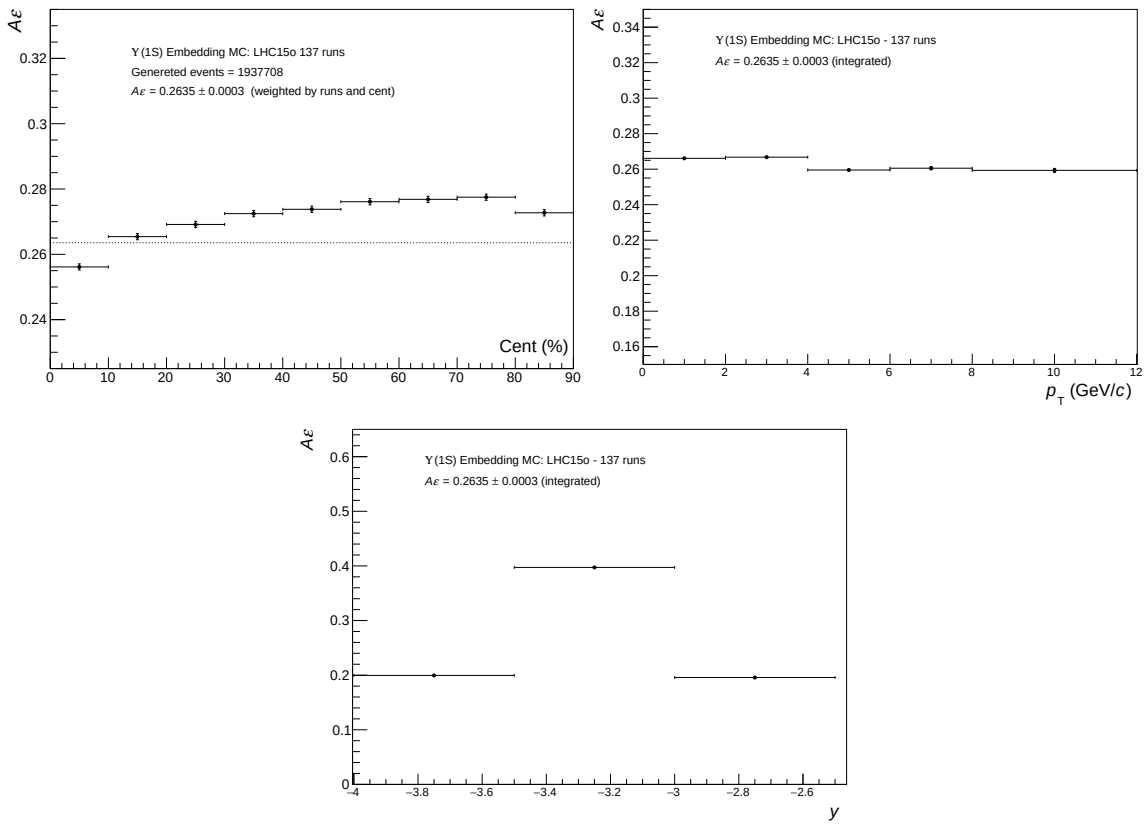

FIGURE 3.2 $A \times \varepsilon$ as a function of centrality (left), p_{T} (center), and y (right). The values have been computed using embedded Monte Carlo events.

$A \times \varepsilon$ for the 0–10% central collisions with respect to the 50–90%. This effect is due to a limitation of the Muon Trigger related to the higher occupancy in the most central events. In fact the Muon Trigger LBs can provide only one tracklet each, hence if two muons cross the same LB only one of the two particles is correctly reconstructed. Further details are given in section 4.5. Differential studies of $A \times \varepsilon$ are presented in the plots reported in figure 3.2.

3.5 Reference pp cross section

The evaluation of R_{AA}requires to divide the yield measured in Pb-Pb collisions by the cross-section measured in pp collisions at the same energy. The statistics of the ALICE measurement at $\sqrt{s} = 5.02$ in pp collisions was not sufficient to provide an estimate of the Υ cross section [37]. For this reason the reference proton-proton cross sections, for Υ(1S) and Υ(2S) production, have been computed by means of an interpolation procedure described below. The energy interpolation for the Υ cross section, as a function of rapidity and for the p_{T} and y integrated result, uses the measurements of Υ production cross sections in pp collisions at $\sqrt{s} = 7$ and 8 TeV by ALICE [78, 79] and at $\sqrt{s} = 2.76, 7$ and 8 TeV by LHCb [80, 81]. In order to obtain the reference cross section in the same p_{T} and y bins as the ones used for the analysis, measurements from LHCb in finer p_{T} and y bins have been combined. The obtained values for different p_{T} intervals, coming from LHCb data only, are reported in tables 3.1, 3.2 and 3.3. The obtained values in different y bins, obtained combining both ALICE and LHCb results, are reported in tables 3.4, 3.5, 3.7, 3.6 and 3.8.

$\sqrt{s_{pp}} = 2.76$ TeV, $2.5 < y < 4.0$						
p_{T} bin	$\sigma_{pp}^{\Upsilon \to \mu^+\mu^-}$	Stat.	uncorr. Syst.	fully corr. Syst.	Total	Relative
GeV/c	pb					%
$0.0 < p_{\mathrm{T}} < 2.0$	154,2	12,6	0,0	6,6	14,2	9,2
$2.0 < p_{\mathrm{T}} < 4.0$	192,6	12,8	0,0	9,6	16,0	8,3
$4.0 < p_{\mathrm{T}} < 6.0$	166,2	13,8	0,0	7,8	15,9	9,5
$6.0 < p_{\mathrm{T}} < 15.0$	153,0	12,4	0,0	6,6	14,0	9,2

TABLE 3.1 Reference cross sections and corresponding uncertainties in different p_{T} intervals. $\sigma_{pp}^{\Upsilon \to \mu^+\mu^-}$ values and uncertainties as obtained using LHCb pp data at $\sqrt{s_{pp}} = 2.76$ TeV.

The energy interpolation is performed fitting the experimental data using the empirical functions listed below :

— Linear function : $p_0 + p_1 \cdot \sqrt{s}$

— Parabola : $p_0 \cdot \sqrt{s} + p_1 \cdot (\sqrt{s})^2$

$\sqrt{s_{pp}} = 7$ TeV, $2.5 < y < 4.0$						
p_{T} bin	$\sigma_{pp}^{\Upsilon\to\mu^+\mu^-}$	Stat.	uncorr. Syst.	fully corr. Syst.	Total	Relative
GeV/c	pb					%
$0.0 < p_{\mathrm{T}} < 2.0$	278,750	0,917	1,078	8,641	8,756	3,141
$2.0 < p_{\mathrm{T}} < 4.0$	497,600	1,311	1,105	15,426	15,521	3,119
$4.0 < p_{\mathrm{T}} < 6.0$	385,600	1,068	1,054	11,954	12,047	3,124
$6.0 < p_{\mathrm{T}} < 15.0$	473,720	1,197	0,936	14,685	14,764	3,117

TABLE 3.2 Reference cross sections and corresponding uncertainties in different p_{T} intervals. $\sigma_{pp}^{\Upsilon\to\mu^+\mu^-}$ values and uncertainties as obtained using LHCb pp data at $\sqrt{s_{pp}} = 7$ TeV.

$\sqrt{s_{pp}} = 8$ TeV, $2.5 < y < 4.0$						
p_{T} bin	$\sigma_{pp}^{\Upsilon\to\mu^+\mu^-}$	Stat.	uncorr. Syst.	fully corr. Syst.	Total	%
GeV/c	pb					%
$0.0 < p_{\mathrm{T}} < 2.0$	337.680	0.811	0.967	9.455	9.539	2.825
$2.0 < p_{\mathrm{T}} < 4.0$	610.400	1.068	1.367	17.091	17.179	2.814
$4.0 < p_{\mathrm{T}} < 6.0$	481.000	0.906	1.010	13.468	13.536	2.814
$6.0 < p_{\mathrm{T}} < 15.0$	609.970	1.022	0.905	17.079	17.134	2.809

TABLE 3.3 Reference cross sections and corresponding uncertainties in different p_{T} intervals. $\sigma_{pp}^{\Upsilon\to\mu^+\mu^-}$ values and uncertainties as obtained using LHCb pp data at $\sqrt{s_{pp}} = 8$ TeV.

$\sqrt{s_{pp}} = 2.76$ TeV, $0 < p_{\mathrm{T}} < 15$						
y bin	$d(\sigma_{pp}^{\Upsilon\to\mu^+\mu^-})/dy$	Stat.	uncorr. Syst.	fully corr. Syst.	Total	%
GeV/c	pb					%
$2.5 < y < 3.0$	642	36	0	24	43	7
$3.0 < y < 3.5$	454	26	0	16	31	7
$3.5 < y < 4.0$	248	22	0	10	24	10
$2.5 < y < 4.0$	448	17	0	16	24	5

TABLE 3.4 y bins $d(\sigma_{pp}^{\Upsilon\to\mu^+\mu^-})/dy$ values and uncertainties as obtained using LHCb pp data at $\sqrt{s_{pp}} = 2{,}76$ TeV.

$\sqrt{s_{pp}} = 7$ TeV, $0 < p_{\mathrm{T}} < 15$						
y bin	$d(\sigma_{pp}^{\Upsilon\to\mu^+\mu^-})/dy$	Stat.	uncorr. Syst.	fully corr. Syst.	Total	%
GeV/c	pb					%
$2.5 < y < 3.0$	1291.40	2.96	2.08	40.20	40.36	3.1
$3.0 < y < 3.5$	1116.58	2.48	2.04	34.76	34.91	3.1
$3.5 < y < 4.0$	863.36	2.40	2.98	27.04	27.31	3.2
$2.5 < y < 4.0$	1090.45	4.55	4.17	33.80	34.36	3.2

TABLE 3.5 y bins $d(\sigma_{pp}^{\Upsilon\to\mu^+\mu^-})/dy$ values and uncertainties as obtained using LHCb pp data at $\sqrt{s_{pp}} = 7$ TeV.

$\sqrt{s_{pp}} = 8$ TeV, $0 < p_{\mathrm{T}} < 15$						
y bin	$d(\sigma_{pp}^{\Upsilon\to\mu^+\mu^-})/dy$	Stat.	uncorr. Syst.	fully corr. Syst.	Total	%
GeV/c	pb					%
$2.5 < y < 3.0$	1659.32	2.50	2.44	46.60	46.73	2.8
$3.0 < y < 3.5$	1370.82	2.04	2.66	38.52	38.67	2.8
$3.5 < y < 4.0$	1047.96	2.06	2.34	29.50	29.66	2.8
$2.5 < y < 4.0$	1359.37	3.83	4.30	38.06	38.50	2.8

TABLE 3.6 y bins $d(\sigma_{pp}^{\Upsilon\to\mu^+\mu^-})/dy$ values and uncertainties as obtained using LHCb pp data at $\sqrt{s_{pp}} = 8$ TeV.

$\sqrt{s_{pp}} = 7$ TeV, $0 < p_{\mathrm{T}} < 12$						
y bin	$d(\sigma_{pp}^{\Upsilon\to\mu^+\mu^-})/dy$	Stat.	uncorr. Syst.	fully corr. Syst.	Total	%
GeV/c	pb					%
$2.5 < y < 3.0$	1158.16	183.52	151.52	58.03	244.81	21.1
$3.0 < y < 3.5$	944.88	143.84	163.68	47.37	222.99	23.6
$3.5 < y < 4.0$	607.60	124.00	81.84	30.50	151.67	25.0
$2.5 < y < 4.0$	896.11	82.67	110.77	44.81	145.30	17.2

TABLE 3.7 y bins $d(\sigma_{pp}^{\Upsilon\to\mu^+\mu^-})/dy$ values and uncertainties as obtained using ALICE pp data at $\sqrt{s_{pp}} = 7$ TeV.

$\sqrt{s_{pp}} = 8$ TeV, $0 < p_{\mathrm{T}} < 12$						
y bin	$d(\sigma_{pp}^{\Upsilon\to\mu^+\mu^-})/dy$	Stat.	uncorr. Syst.	fully corr. Syst.	Total	%
GeV/c	pb					%
$2.5 < y < 3.0$	1669.04	270.32	143.84	83.45	317.38	19.0
$3.0 < y < 3.5$	1173.04	136.40	91.76	58.65	174.54	14.9
$3.5 < y < 4.0$	806.00	161.20	89.28	40.30	188.63	23.4
$2.5 < y < 4.0$	1173.87	99.20	115.73	58.69	163.34	13.9

TABLE 3.8 y bins $d(\sigma_{pp}^{\Upsilon\to\mu^+\mu^-})/dy$ values and uncertainties as obtained using ALICE pp data at $\sqrt{s_{pp}} = 8$ TeV.

— Positive exponential : $p_0 \cdot \sqrt{s} \cdot e^{\frac{\sqrt{s}}{p_1}}$

— Negative exponential : $p_0 \cdot (1 - e^{\frac{-\sqrt{s}}{p_1}})$

— Power law : $p_0 \cdot (\sqrt{s})^{p_1}$

The requirement for such functions is to be able to intercept the origin of the axes. This choice is driven by the convincing assumption that at $\sqrt{s} = 0$ TeV the cross-section drops to 0. The energy interpolation for the Υ(1S) cross section as a function of p_{T} is based on LHCb measurements only, since the p_{T} coverage of the results of this analysis ($p_{\mathrm{T}} < 15$ GeV/c) is more extended than that of the corresponding ALICE pp data ($p_{\mathrm{T}} < 12$ GeV/c). The plots representing the data points, the interpolation functions and the interpolated values are shown in figure 3.3.

The final cross section value is the weighted average of the whole set of interpolated values. The total uncertainty on the interpolated pp cross-section corresponds to the quadratic sum of two terms. One term represents the statistical uncertainty and reflects the uncertainties on the data samples used in the interpolation procedure. The second term represents the systematic uncertainty related to the interpolation procedure itself. It corresponds to the maximum spread between the final cross section value and each single interpolation. The numerical values obtained from the interpolation procedure are summarized in Table 3.9 for the various kinematic ranges used in the analysis. The result of the interpolation procedure gives $\mathrm{BR}_{\Upsilon(1\mathrm{S})\to\mu^+\mu^-} \cdot \sigma_{\mathrm{pp}}^{\Upsilon(1\mathrm{S})} = 1221 \pm 77(\mathrm{tot})$ pb and $\mathrm{BR}_{\Upsilon(2\mathrm{S})\to\mu^+\mu^-} \cdot \sigma_{\mathrm{pp}}^{\Upsilon(2\mathrm{S})} = 302 \pm 23(\mathrm{tot})$ pb assuming unpolarized quarkonia and integrating over the ranges $2.5 < y < 4$ and $p_{\mathrm{T}} < 15\ GeV/c$.

It should be noted that the integrals of the interpolated p_{T}-differential and y-differential cross sections differ by at most $\approx 3\%$ from the interpolated integrated cross sections. This indicates a good consistency of the interpolation procedure across various kinematical ranges,

also considering that the uncertainties on the obtained cross sections are not completely correlated.

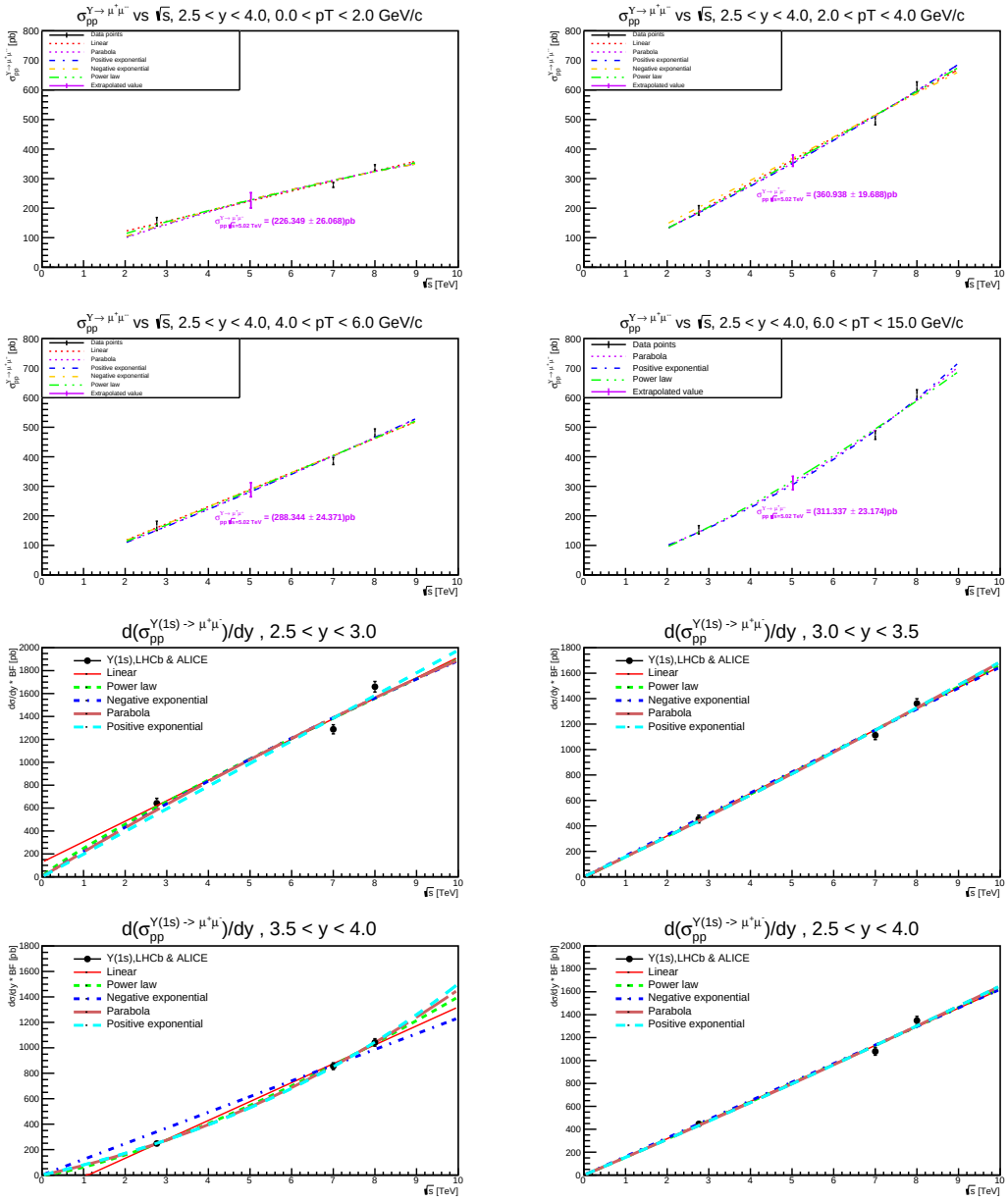

FIGURE 3.3 Interpolation of reference σ_{pp} in p_{T} (top 4 graphs) and y (bottom 4 graphs) bins. The measured points are reported with an error bar that is the quadratic sum of the statistical and systematic uncertainties.

p_T (GeV/c)	y	$BR_{\Upsilon(1S)\to\mu^+\mu^-} \cdot \sigma_{pp}^{\Upsilon(1S)}$ (pb)
[0-2]	[2.5-4]	226 ± 26
[2-4]		361 ± 20
[4-6]		288 ± 24
[6-15]		311 ± 23
[0-15]	[2.5-3]	506 ± 57
	[3-3.5]	415 ± 28
	[3.5-4]	288 ± 24

TABLE 3.9 The interpolated branching ratio times cross section of Υ(1S) for the p_T and y bins under study.

3.6 Uncertainties

The systematic uncertainty on R_{AA}has several contributions related to the various ingredients which constitute the nuclear modification definition in equation 3.1. The estimation of the systematic uncertainties will be detailed in the following.

The systematic uncertainty on the signal extraction is evaluated by considering the variations in the signal counts when using various functions for the description of the background for the invariant mass distribution, as well as adopting two fitting ranges, *i.e.* $(7-14)$ GeV/c^2 and $(7.5-14.5)$ GeV/c^2. As it has already been mentioned, the signal extraction procedure can be performed either on the raw mass spectrum or on the mass spectrum with applied event mixing subtraction. In both cases, the resulting distribution is fitted with the sum of three extended CB and a function to account for the residual background. The extended CB tail parameters have been varied using estimates provided by two MC transport models : GEANT4 [82] and GEANT3 [83]. Due to lack of statistics for the higher mass bottomonium resonances, the mass position and width of the Υ(2S) and Υ(3S) have been fixed to the Υ(1S) position and width obtained from the fit, using the ratio obtained from the PDG as scaling factor. To take in account for the statistical uncertainty on such choice, the ratio of Υ(2S) (Υ(3S)) to Υ(1S) widths is varied from 1 (1) to 1.06 (1.12). In the centrality, p_T or y differential studies, the mass position and width are also varied, by an amount which corresponds to the uncertainties on the mass position and the width returned by the fit to the integrated invariant mass spectrum. The central values of N^{Υ} and their statistical uncertainties are obtained by taking the weighted average of N^{Υ} and of the corresponding statistical uncertainties from the various fits. The systematic uncertainties are estimated as the root mean square of the distribution of N^{Υ} obtained from the various fits.

As already reported, a cut of $p_{\mathrm{T}} > 2$ GeV/c on single muons has been applied to filter out the contribution of muons from K and π decays. The impact of such cut on signal and background can be qualitatively evaluated from the scatter plots reported in figure 3.4.

The effect induced by that cut on Υ yields was estimated by varying that cut by $\pm 10\%$. A $\pm 2\%$ maximum variation on the number of detected Υ resonances, N^{Υ}, was observed and included in the systematic uncertainties.

Various sources contribute to the systematic uncertainties of $A \times \varepsilon$, such as input MC, the trigger efficiency, the track reconstruction efficiency and finally the matching efficiency between tracks in the muon tracking and triggering chambers.

To evaluate the systematic uncertainty induced by the MC input shapes, various sets of simulations have been produced with different Υ input p_{T} and y distributions, obtained from empirical parameterizations and/or extrapolations of available data sets, such as ALICE data in Pb–Pb collisions at $\sqrt{s_{\mathrm{NN}}} = 5.02$ TeV, $\sqrt{s_{\mathrm{NN}}} = 2.76$ TeV and pp collisions at $\sqrt{s} =$ 5.02 TeV and CDF data in Pb–Pb at $\sqrt{s_{\mathrm{NN}}} = 4$ TeV. The maximum relative difference of $A \times \varepsilon$ obtained using the various input shapes is taken as the systematic uncertainty due to the MC input. A summary of all the tests can be found in figure 3.5.

In order to calculate the systematic uncertainty on the trigger efficiency, the trigger response function for single muons is evaluated using either MC or data. The two response functions are then separately applied to simulations of a Υ sample and the difference obtained for the Υ reconstruction efficiency is taken as systematic uncertainty (see figure 3.6).

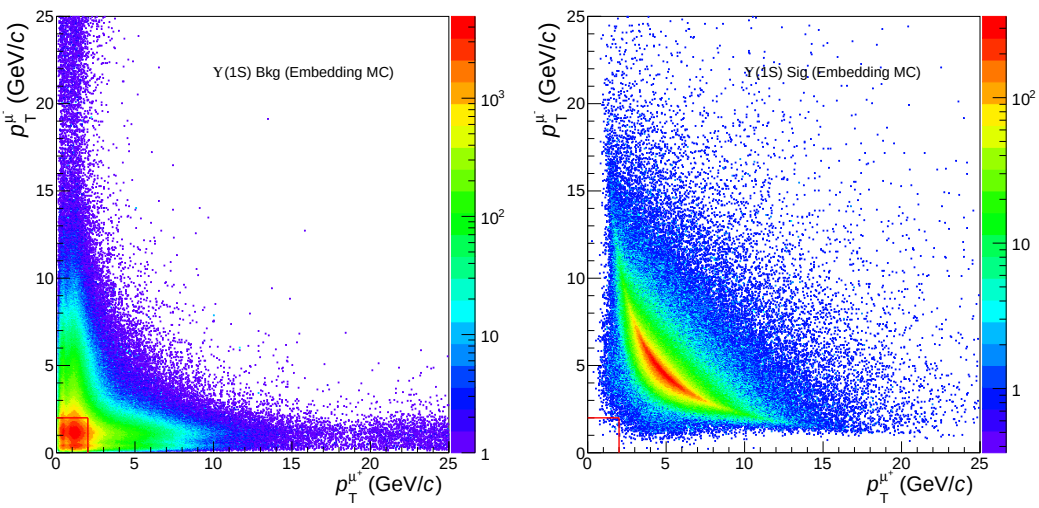

FIGURE 3.4 Scatter plot of muon pair candidates' p_{T} s for background candidates (left) and signal candidates (right). The cut at $p_{\mathrm{T}} = 2\mathrm{GeV/c}$ on both muons is represented as a red box.

The Muon Trigger chamber efficiency is estimated from real data and gets plugged on the Monte Carlo simulations. The uncertainty on the efficiency estimation leads to an uncertainty on the trigger efficiency. In order to evaluate such uncertainty, two Monte Carlo productions have been performed. The first simulation is performed using the efficiency value estimated using real data. In the second simulation, the efficiency is artificially modified within its uncertainties. The systematic uncertainty induced by this variation is then evaluated as the

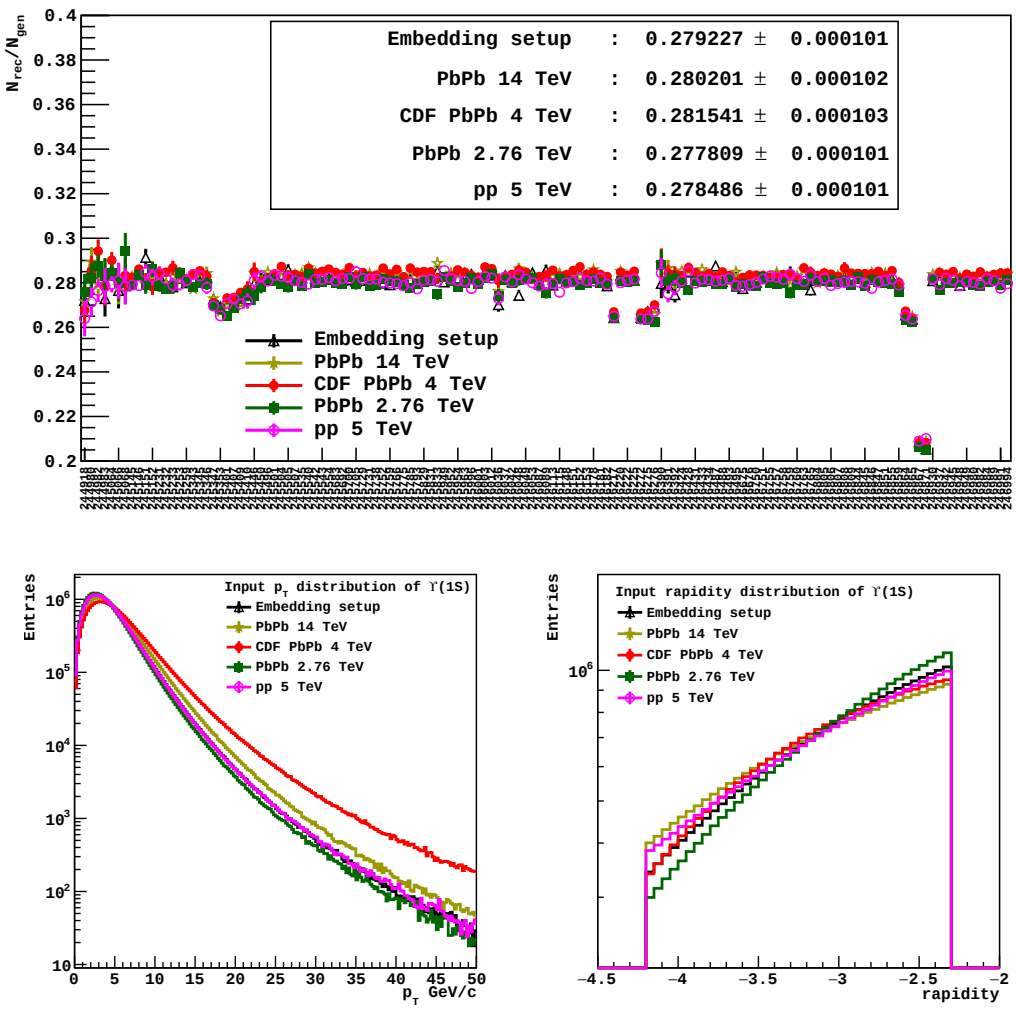

FIGURE 3.5 Evolution of the N_{rec}/N_{gen} ratio versus run number (top). Different colors refer to different input distributions for $\Upsilon(1S)$ p_T and y values, represented with the same color code in the bottom panel. Please note that the systematic study as a function of rapidity adopts an inverted convention for rapidity values, with respect to that adopted in this thesis, hence rapidity values are quoted as negative.

relative difference between the two. The values obtained with the two chamber efficiency sets are reported in figure 3.7.

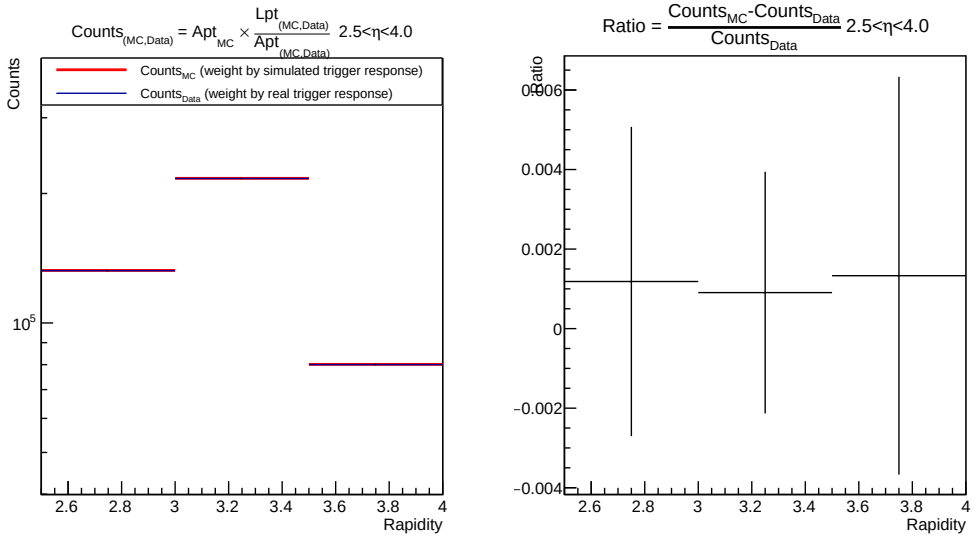

FIGURE 3.6 On left panel the muon trigger response function as a function of y is shown. Trigger response is reweighted using Monte Carlo data (red) or real data (blue). Right panel shows the ratio of the two series as a function of y.

The systematic uncertainty on the tracking efficiency is obtained starting from an evaluation of the single muon tracking efficiency in MC and data. This evaluation is performed via a procedure, detailed in [43], based on the redundancy of the tracking chamber information. The Υ reconstruction efficiency is then obtained by combining the single muon efficiencies of the two systems, namely muon trigger and muon tracker. The systematic uncertainty generated by the Υ reconstruction efficiency is taken as the relative difference of the values obtained with the procedure based on MC and data.

The muon tracks for data analysis are chosen based on a selection on the χ^2 of the matching between a track segment in the trigger system with the extrapolation of a track in the tracking chambers. The matching systematics is obtained by varying the χ^2 selection cut in data and MC and comparing the effects on the track reconstruction efficiency [37].

The systematic uncertainty on the centrality measurement is evaluated by varying by $\pm 0.5\%$ the V0 signal amplitude corresponding to 90% of the hadronic cross section in Pb–Pb collisions. This choice is driven by the fact that the 90% bin is used as anchor point to define the centrality classes [84].

The systematic uncertainty on the evaluation of σ_{Υ}^{pp} is detailed in section 3.5.

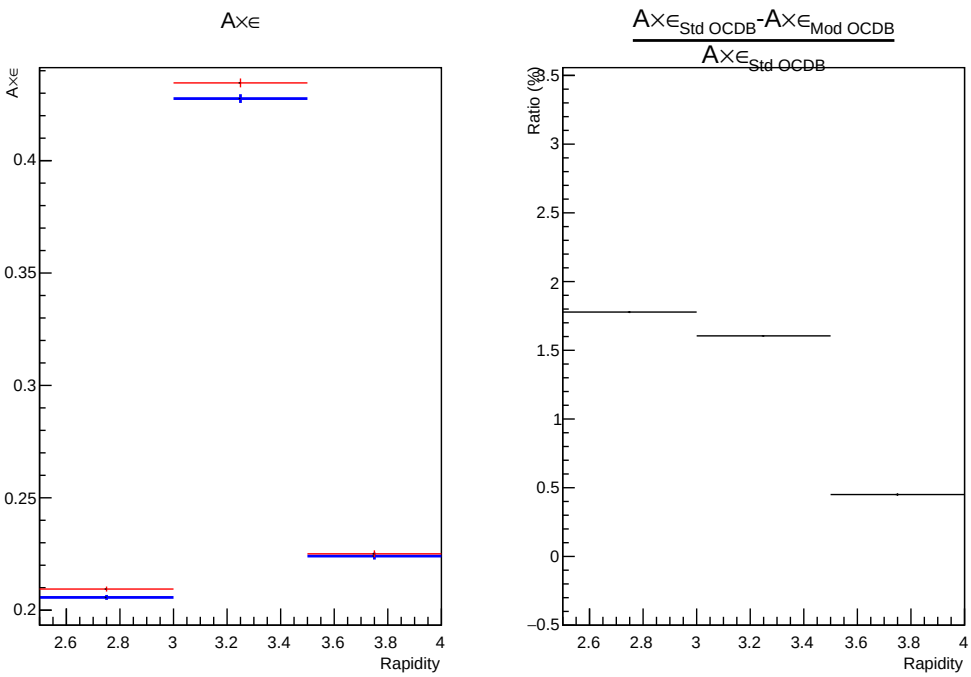

FIGURE 3.7 On left panel the muon trigger $A \times \varepsilon$ as a function of y is shown. Trigger efficiency is evaluated as the standard Monte Carlo set (red) or the real one (blue). Right panel shows the ratio of the two series as a function of y.

Finally, the systematic uncertainty evaluation of F_{norm} and $\langle T_{\text{AA}} \rangle$ are described in [37] and [3], respectively.

The different systematic uncertainty sources on the R_{AA} calculation are summarized in Table 3.10. The correlated systematic uncertainties as a function of centrality, y or p_{t} are indicated as type I. The uncorrelated ones as type II.

3.7 Results

The nuclear modification factors for inclusive Υ(1S) and Υ(2S) production in Pb–Pb collisions at $\sqrt{s_{\text{NN}}} = 5.02$ TeV with $p_{\text{T}} < 15$ GeV/c, $2.5 < y < 4$ and the 0–90% centrality class are $R_{\text{AA}}^{\Upsilon(1\text{S})} = 0.37 \pm 0.02(\text{stat}) \pm 0.03(\text{syst})$ and $R_{\text{AA}}^{\Upsilon(2\text{S})} = 0.10 \pm 0.04(\text{stat}) \pm 0.02(\text{syst})$, respectively. The quantities entering the $R_{\text{AA}}$for the Υ(2S) have been determined exactly in the same ways as those for the Υ(1S). The measurements show a strong suppression for both bottomonium states.

sources	Υ(1S)				Υ(2S)
	Centrality	y	p_T	Integrated	Integrated
Signal extraction	4.3-6.1%(II)	4.2-6.8%(II)	5.2-8.7%(II)	4.1%	21.7%
Muon p_T cut	0.3-2.4%(II)	0.1-1.2%(II)	0.1-2.4%(II)	0.7%	0.7%
Input MC	0.9%(I)	0.6-2.6%(II)	1-1.4%(II)	0.9%	0.9%
Tracker efficiency	3%(I) and 0-1%(II)	1%(I) and 3%(II)	1%(I) and 3%(II)	3%	3%
Trigger efficiency	3%(I)	1.4-3.7%(II)	0.4-2.6%(II)	3%	3%
Matching efficiency	1%(I)	1%(II)	1%(II)	1%	1%
Centrality	0.2-2.4%(II)	-	-	-	-
F_{norm}	0.5%(I)	0.5%(I)	0.5%(I)	0.5%	0.5%
$\langle T_{AA} \rangle$	3.1-5.3%(II)	3.2%(I)	3.2%(I)	3.2%	3.2%
$BR_{\Upsilon\to\mu^+\mu^-} \cdot \sigma_\Upsilon^{pp}$	6.3%(I)	6.6-11.3%(II)	5.5-11.5%(II)	6.3%	7.5%

TABLE 3.10 Summary of the systematic uncertainties for R_{AA} calculation. Type I (II) refers to correlated (uncorrelated) systematic uncertainties.

The value of the systematic uncertainties affecting the R_{AA} is comparable to those of the statistical ones. To reduce the contribution of systematic uncertainties the ratio of the two R_{AA} can be computed. However the dominant contributions to the systematic uncertainties, namely those related to signal extraction and the pp cross section, are not simplified by the computation of the ratio. The integrated ratio $R_{AA}^{\Upsilon(2S)}/R_{AA}^{\Upsilon(1S)}$ is $0.28 \pm 0.12(\text{stat}) \pm 0.06(\text{syst})$. An indication of a stronger suppression for Υ(2S) around 4.7σ is present.

A comparison between Υ(1S) nuclear modification factor values at different energies might highlight a suppression dependence on the center of mass energy of the colliding system. The ratio between the Υ(1S) R_{AA} at $\sqrt{s_{NN}} = 5.02$ TeV and 2.76 TeV is $1.23 \pm 0.21(\text{stat}) \pm 0.19(\text{syst})$. The sources of systematic uncertainties entering the calculation of the ratio are considered uncorrelated, except for the $\langle T_{AA} \rangle$ component, whose uncertainty cancels out. The ratio is compatible with unity within uncertainties, hence no energy dependence is observed within the present uncertainties.

The centrality, p_T and y-dependences of the Υ(1S) R_{AA} at forward rapidity at $\sqrt{s_{NN}} = 5.02$ TeV are shown in figure 3.8. A decrease of R_{AA} with increasing centrality is observed down to $R_{AA}^{\Upsilon(1S)} = 0.33 \pm 0.03(\text{stat}) \pm 0.03(\text{syst})$ for the 0–10% most central collisions. The p_T-dependence is observed to be compatible within uncertainties with a flat behaviour up to $p_T = 15$ GeV/c. The y-dependence shows a R_{AA} compatible within uncertainties with a flat distribution, as already observed in the measurements at $\sqrt{s_{NN}} = 2.76$TeV [6]. However, since the uncertainties are large especially at low p_T, further data are needed in order to have a stronger conclusion on the rapidity dependence of the R_{AA}.

The inclusive Υ(1S) R_{AA} measurements are compared to several theoretical predictions in Fig. 3.9. The set of models used for comparison is composed by two transport models (TM1 and TM2)[13, 14] and one hydro-dynamical model [15]. While transport models follow the propagation of the free quarks in the medium, the hydro-dynamical models approach the

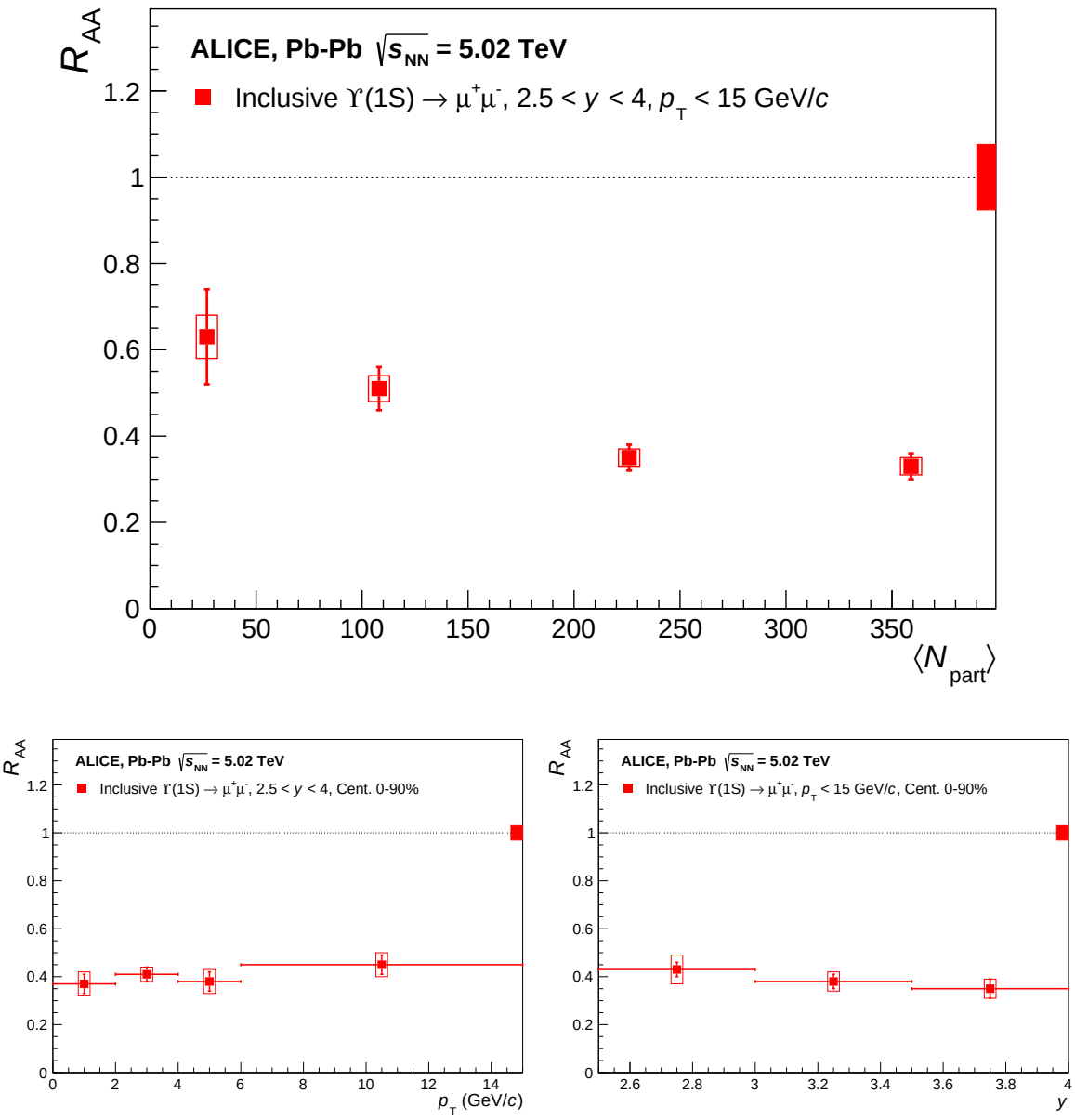

FIGURE 3.8 Inclusive ϒ(1S) R_{AA} as a function of centrality (top), p_T (left) and y (right) at forward rapidity at $\sqrt{s_{NN}} = 5.02$ TeV. The vertical error bars and the boxes represent the statistical and uncorrelated systematic uncertainties, respectively. The relative correlated uncertainty is shown as boxes at unity.

QGP as a macro state. Transport models use a rate-equation approach which accounts for both suppression and (re)generatio mechanisms in the QGP. In hydro-dynamical models, the macro state "decays" in micro states (*e.g* quarkonium states, open heavy flavor hadrons) at the freeze-out.

In the model quoted as TM1 [13], the evolution of the thermal medium is based on a thermal-fireball expansion. The feed-down contribution is taken into account based on measurements from ALICE and LHCb [78, 85, 86]. TM1 predictions are shown as bands, obtained varying the magnitude of nuclear shadowing effects, as described in [87]. The upper limit shown in Fig. 3.9 corresponds to the extreme case of the absence of shadowing while the lower limit reflects a reduction of 30% due to shadowing.

TM2 [14] uses a 2+1 dimensional version of ideal hydrodynamic equations. The uncertainties on these predictions are given by the spread caused by two sets of feed-down fractions to $\Upsilon(1S)$ ground state :

— 27% from χ_b ; 11% from $\Upsilon(2S+3S)$

— 37% from χ_b ; 12% from $\Upsilon(2S+3S)$

In TM2, the shadowing parameterization is based on EKS98 [48].

Finally, the $\Upsilon(1S)$ production cross section in pp collisions at $\sqrt{s} = 5.02$ TeV in the rapidity range $2.5 < y < 4$ is taken as $d\sigma_{pp}^{\Upsilon(1S)}/dy = 28.8$ nb in TM1 and $d\sigma_{pp}^{\Upsilon(1S)}/dy = 30$ nb in TM2. Those values deviate by about 2σ (TM1) and 1.4σ (TM2) from the result obtained using the pp interpolation method reported in the previous section.

In the hydro-dynamical model [15], a thermal suppression of the bottomonium states is calculated using a lattice QCD-vetted complex-potential approach through a description of the medium evolution based on the 3+1d anisotropic hydro-dynamical model. In this recent study, no significant variation of the R_{AA} has been observed with respect to the plasma shear viscosity-to-entropy density ratio ($4\pi\eta/s$) parameter of the hydro evolution. Therefore, it is set to $4\pi\eta/s = 2$, which is consistent with particle spectra fits. The uncertainties of the model come from the heavy-quark potential uncertainty that was estimated by including a $\pm 15\%$ variation of the Debye mass of the QCD medium. The latter is tuned by a fit to the real-part of the lattice in-medium heavy-quark potential. The uncertainty of the Debye mass of the heavy-quark potential implies $\sim 15\%$ uncertainty on the expected bottomonium R_{AA}. Furthermore, the predictions shown in figure 3.9 are referring to the initial momentum-space anisotropy parameter $\xi_0 = 0$, which corresponds to a perfectly isotropic QGP at the starting point of the hydrodynamic evolution at $\tau_0 = 0.3$ fm/c. Finally, this model accounts for feed-down contributions but it includes neither a regeneration mechanism nor CNM effects.

The centrality dependence of the $\Upsilon(1S)$ R_{AA} is fairly reproduced by the model calculations, as shown in the top panel of Fig. 3.9. The data is best described by TM1 when regeneration is included and by TM2 when regeneration is not taken into account. The uncertainties on the measured point do not allow for a discrimination between the two models, hence a firm conclusion on whether the regeneration is present or not is not possible. The hydro-dynamical model describes the trend of the data, even if the measurements systemati-

cally lie on the upper edge of the uncertainty band for $N_{\text{part}} > 70$. This can be interpreted as a hint of a larger heavy-quark potential than assumed in the model.

As a function of p_{T} (bottom left panel of Fig. 3.9), the data favor the regeneration scenario of the TM1 model. As for the centrality dependence, the hydro-dynamical model is in agreement with measurements even if the data points are systematically at the top edge of the uncertainty band.

For what concerns the y-dependence of the Υ(1S) R_{AA} only the hydro-dynamical model provides an estimation of the expected trend. Even if the data points are compatible within uncertainties with the model estimation and with a flat distribution, some tension can be observed between the model-suggested trend and the trend shown by measurements (bottom right panel of Fig. 3.9).

3.8 Summary

The nuclear modification factors of inclusive Υ(1S) and Υ(2S) production was measured with the ALICE detector at forward rapidity ($2.5 < y < 4.0$) and for $p_{\text{T}} < 15$ GeV/c in Pb–Pb collisions at $\sqrt{s_{\text{NN}}} = 5.02$ TeV.

The double ratio of the Υ(1S) and Υ(2S) $R_{\text{AA}}$was computed as well. The observed value of $0.28 \pm 0.12(stat.) \pm 0.06(syst.)$ is compatible with the hypothesis of a larger suppression for the higher-energy (more weakly bound) states.

Finally, the double ratio of the Υ R_{AA}measured in Pb-Pb collisions at $\sqrt{s_{\text{NN}}} = 5.02$ and 2.76 TeV was computed as well. The result shows no significant energy dependence at the LHC.

The results have been compared with transport and hydrodynamic models. The transport models are able to provide prediction with and without including recombination effects. The comparison between the measurements with the different predictions lead to no clear conclusion on whether recombination effects play a role. Further measurements with larger statistics will be needed to improve the precision and to better constrain the models.

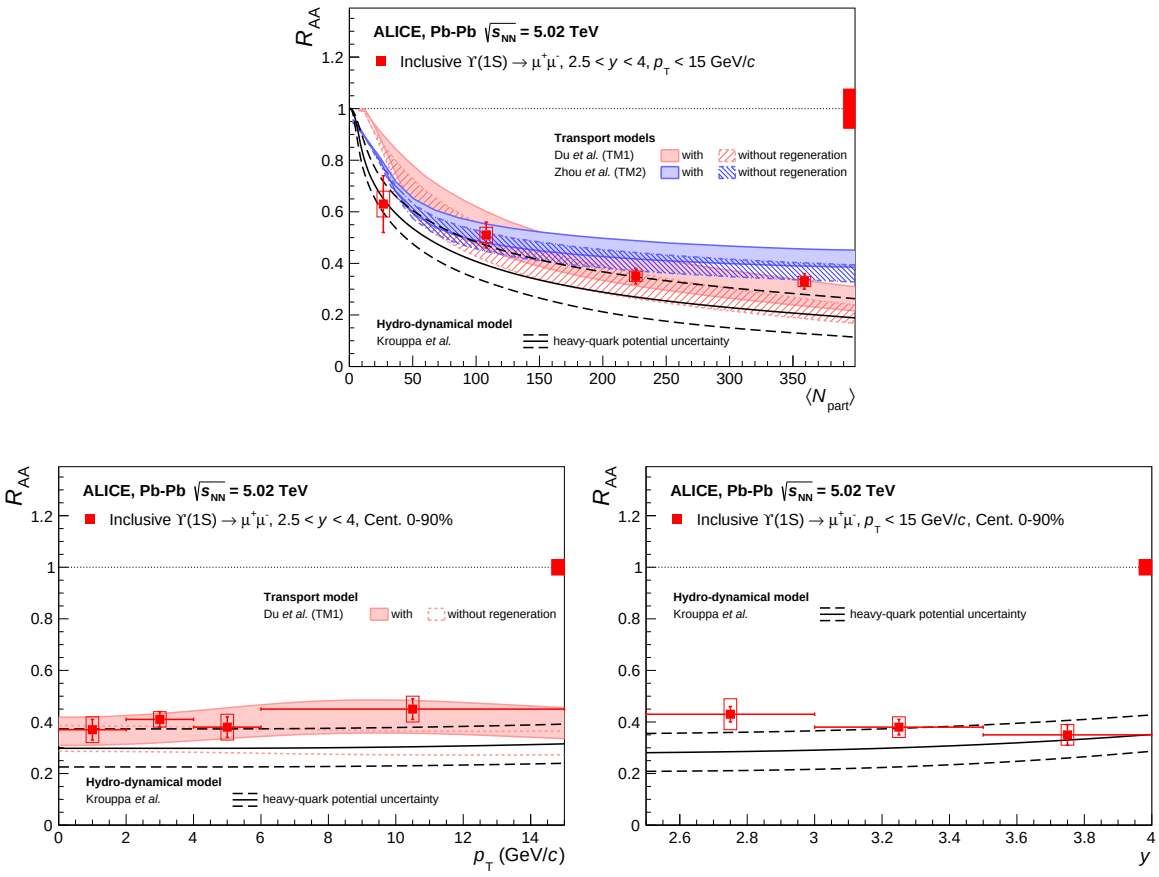

FIGURE 3.9 Inclusive ϒ(1S) R_{AA} compared to predictions from two transport models [13, 14] and one hydro-dynamical model [15] as a function of centrality (top), p_T (left) and y (right). See text for details on the models. While all models provide centrality dependence predictions, some of them do not provide p_T and/or y estimations. The plots report all the available information at the moment of writing.

Chapitre 4

Development of a Muon Identification acquisition and reconstruction framework for ALICE RUN3

4.1 Motivation

The second LHC run (RUN2) is over at the time of writing this thesis. After that, the LHC will stop for two years (second long shutdown), during which an upgrade that will increase the luminosity reach in $Pb-Pb$ from ≈ 1 Hz/mb to ≈ 6 Hz/mb will be performed. At the same time, ALICE will undergo its major upgrade of detectors, electronics and readout that will allow the experiment to cope with the increased Pb-Pb interaction rate, and to also take pp interactions up to ≈ 1 MHz [88–91, 16]. In addition to the machine development of the LHC, a massive upgrade of the acquisition logic for the whole ALICE apparatus will increase by a factor of ≈ 50 the read-out rate. In order to fit in the throughput limitations of the permanent storage the read-out events will be trimmed down to a value similar to the current 1 kHz. Such selection will be performed online using specific algorithms, rather than hardware triggers and flat down-sampling.

A requirement of a total integrated luminosity of 13 nb^{-1} in Pb-Pb collisions was formulated with the ALICE Letter Of Intent (LOI) [92], split in 10 nb^{-1} at nominal solenoid magnetic field and 3 nb^{-1} at a reduced field of 0.2 T. These requirements are related to specific physics goals, concerning open heavy flavours, low mass dileptons and quarkonium measurements. In particular the plans for J/ψ ($\psi(2S)$) foresee to measure R_{AA} down to $p_T = 0$ with statistical precision higher than 1% (10%) over the whole rapidity interval and

the elliptic flow, quantified through the v_2 coefficient [93], down to $p_{\mathrm{T}} = 0$ with an absolute precision of 0.05.

Most of the physics topics addressed by ALICE concern low p_{T} physics probes characterized by very small signal-to-background ratios, which require the read-out of all Pb-Pb collisions. In order to obtain significant measurements it is important to collect very large statistics. The upgrade of the LHC builds up in this direction. The foreseen increase of the luminosity provided by the LHC will cause an increase of collected data rate. The upgrade of the electronics will allow one to increase the data to a value of about two orders of magnitude larger than the one that ALICE experienced during LHC RUN1 and RUN2. As mentioned above, one of the main goals of the new data campaign is the study of rare probes down to low transverse momenta, a region where the large background makes the triggering techniques very inefficient or even impossible in many situations. Such increase of data size, combined with the high collision and acquisition rates, makes standard approaches difficult to apply without enormous (technical and economical) efforts for the upgrade of computing capabilities. Since the required scaling of computing infrastructure cannot cope with the data throughput increase, a new acquisition and processing paradigm had to be developed. The basic idea is to reduce the data size as early as possible in the stream that goes from the detector to the storage and reconstruction (Fig. 4.1). This goal can be achieved adding pre-processing and reconstruction layers close to the detector acquisition logic. For example some detectors will be equipped with a zero suppression algorithm to reduce the volume of data without losing useful information. Such fast reconstruction will be performed synchronously with the data acquisition and will be based on preliminary calibration and alignment information.

Thanks to this fast and partial reconstruction the amount of stored data will be reduced. This procedure will replace the hardware trigger, allowing one to perform precise selections focused on getting the maximum signal for rare and otherwise non-triggerable observables. A finer reconstruction will be performed offline to provide the best resolution possible. For this finer step the merging of data coming from different detectors will be possible and needed. Despite an upgraded private computing facility, during Pb-Pb collisions the reconstruction will be performed asynchronously and part of the data processing load will be shared between Tier 0 and Tier 1 computing sites of the WLCG (Worldwide LHC Computing GRID). Independently from the colliding system type the archival of data will be performed by Tier 0 and Tier 1 facilities.

The combination of synchronous and asynchronous computing and reconstruction steps is well summarized by the name of the software/hardware upgrade project of ALICE. The Online Offline (O^2) project concerns the creation of a common computing system shared

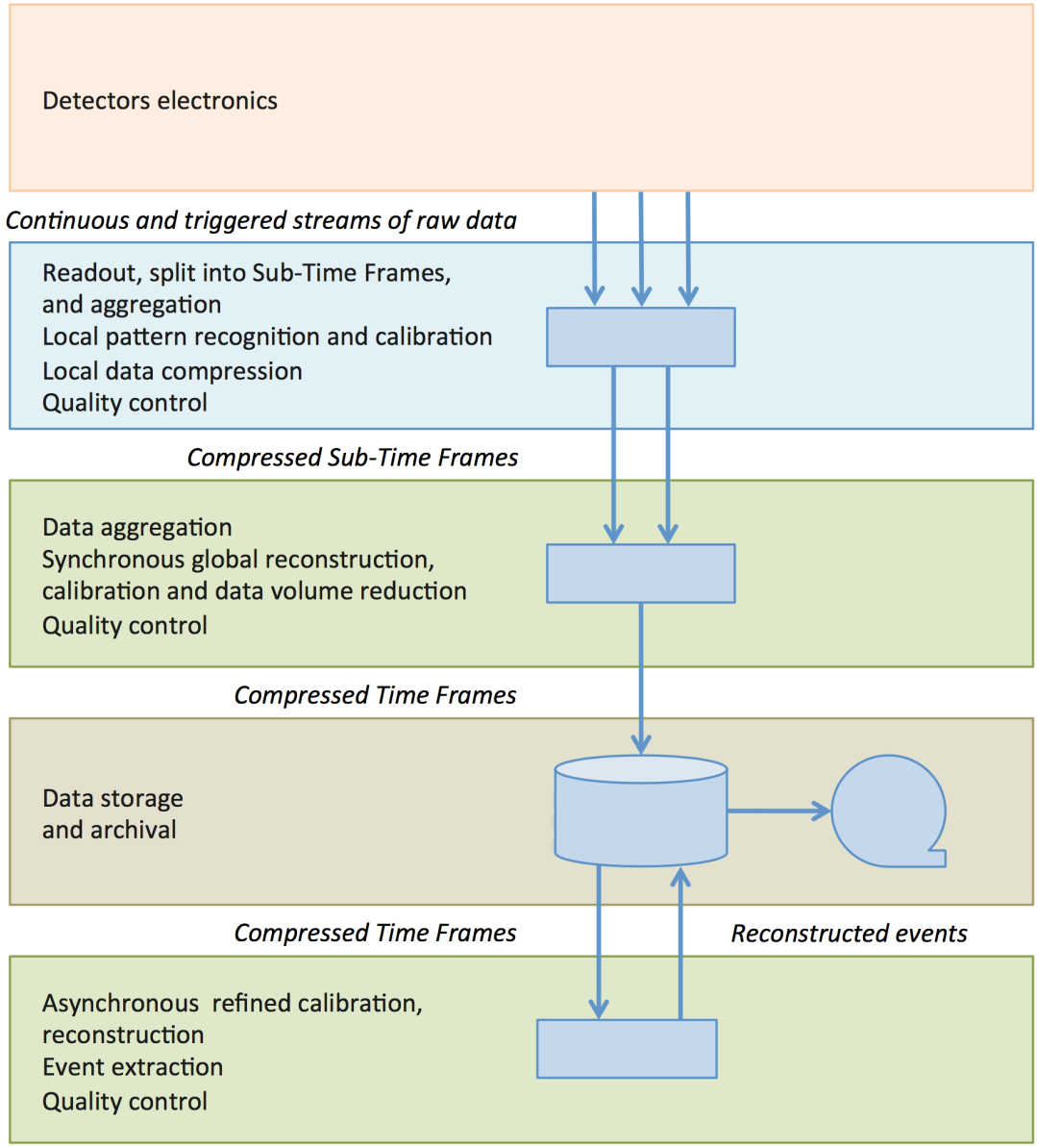

FIGURE 4.1 Sketch of the conceptual structure of the O^2 framework. The detector electronics provides a continuous stream of raw data which is compressed, pre-processed and packed by the read-out logic. Partial information coming from different detectors and systems is aggregated. The full set of data is processed and reconstructed. Up to this step all the computation is performed synchronously. The processed data is then stored and retrieved later for the asynchronous reconstruction. From [16]

by all the ALICE systems and will include a definition of a common computing model, the development of a software framework and the planning and realization of new computing facilities. The O^2 computing facility will be a high-throughput system equipped with heterogeneous computing nodes similar to platforms currently used in several High Performance Computing (HPC) and cloud computing contexts. The computing nodes will integrate several hardware acceleration technologies, spanning from FPGAs to GPUs. The O^2 software framework will grant an adequate abstraction level so that common code can deliver the same functionality across various platforms. This characteristic hides part of the complexity deriving from different hardware choices and specializations of machines devoted to particular tasks, in fact the framework layer allows one to make use of multi-core processors (CPUs) in a way almost transparent to the programmer. Due to fundamental differences between GPU (Graphics Processing Units) and FPGA (Field-Programmable Gate Array) models, the code which is intended to be executed on such accelerators will still require some deep customization. In order to take full advantage of HPC-like infrastructures, as well as of several laptops or standard desktops connected together, the O^2 framework will introduce a concurrent computing model. While the current WLCG is a distributed computing framework, ideally made of lots of single instruction thread machines, the future development of the ALICE computing framework requires some more tuning to take full advantage of parallel processors. Since the first era of the HPC the Message Passing Interface has been used as a standard interconnection protocol for computing nodes in computer clusters. The ALICE computing effort follows a similar approach. The introduction of such MPI [1]-like process-based framework allows for dynamic spawning of workers, which is baked up with a message passing interface capable of using system buses and network interfaces seamlessly and constitutes the backbone of the new infrastructure. The O^2 project will make ALICE able to tackle the next running conditions without modifying the funding model followed during RUN1 and RUN2.

4.2 Common software efforts

The O^2 project stands on a framework commonly developed by the joint scientific community of several experiments. O^2 aims at reducing the complexity of software deployment and to simplify the exploitation of multi- and many-cores architectures and accelerators, minimizing the development effort to be put. The O^2 software does not rely only on general libraries such as Boost, ROOT and CMake, but also on other two frameworks (Fig. 4.2).

1. Message Passing Interface. It is the standard communication protocol between machines belonging to a cluster and working is a shared-memory fashion.

ALFA [94] and FairROOT [95] are actively developed by ALICE at CERN and CMB and PANDA at GSI.

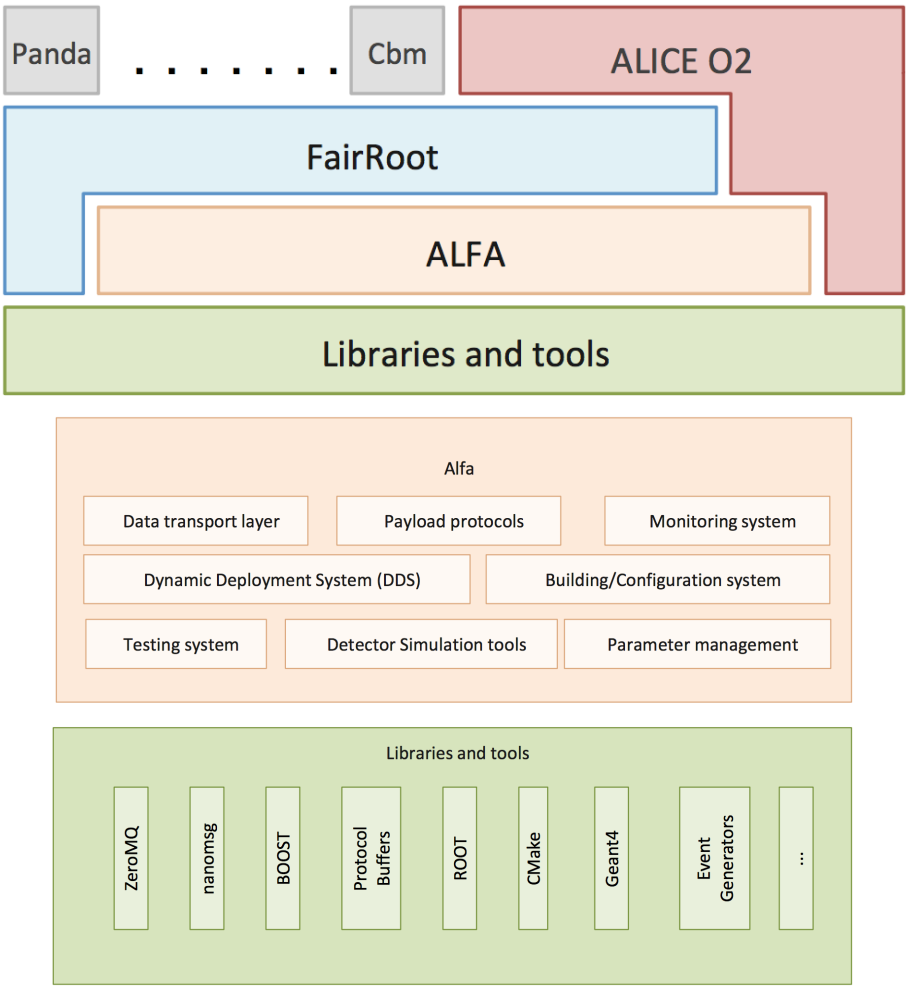

FIGURE 4.2 Software topology of the O^2 project. O^2 stands on several software, sets of libraries and tools. The green boxes represents the low level libraries which constitutes the basis of the software. Some of them are ZeroMQ as message passing protocol, CMake as project build and test manager, Geant4 as particles propagation engine. The orange boxes represents ALFA, developed between ALICE and FAIR. This tool contains a set of high level tools, such as data transportation routines and the dynamic deployment system for the dynamic devices management. The blue box represents FairROOT, an evolution of ROOT focused on improved usability for the end-users. It allows for easy data visualization, storage, offline analysis and more. The ALICE O^2 stands on all these elements alongside other collaborations software (Panda, Cbm). From [16]

ALFA is a communication and concurrent computing framework. The handling of an heterogeneous computing system requires two fundamental aspects : communication and coordination. ALFA provides both aspects and has been developed with high throughput and low latency in mind. The communication layer is based on the ZeroMQ [96] library and allows the passing of binary messages either across network interfaces or between threads within the same machine, by passing memory references. ZeroMQ is a lightweight message passing interface which is based on a POSIX [2] socket back-end, extending the socket characteristics to make them able to concatenate several messages to optimize transfer rates and to unfold them at destination. The messages transferred via ZeroMQ have to be serialized as binary buffers. The available serialization methods are based on Boost, Google's Protocol buffers [97] and ROOT streamers, while the ability to use user defined methods is still left as an option.

The FairROOT framework is an object oriented simulation, reconstruction and data analysis framework developed for the FAIR project at GSI. It provides core services for Monte Carlo simulations, physics analysis, event visualization and other fundamental tasks. All the provided functions are accessible in a simple way, in order to simplify the detectors description as well as the creation of analysis workflows.

4.3 Data format

The O^2 project introduces a modern approach to the packing of data. The storage and acquisition model is aimed at reaching the highest rate capability. Each storage system packs, with the useful data, a bunch of metadata which constitute a overhead. Such overhead becomes important for both the transmission and for the storage of data, since part of the bandwidth and/or of the storage capacity is consumed by that.

The solution introduced by O^2 is the so called Time Frame (TF). The TF is a container defined by two temporal boundaries which define its validity interval (Fig. 4.3). It packs the data collected by the detectors within the validity interval. The format chosen for the TF comprehends a header which works as a summary, in order to ease the access to the contained data, and the detector data itself. The only constraints on the TF content regard the data header specification, while it was chosen to keep as much freedom as possible for what concerns the payload. For this reason the header must provide a complete description of

2. Portable Operating System Interface for uniX. Is a family of standards specified by the IEEE Computer Society for maintaining compatibility between operating systems. POSIX defines the application programming interface (API), along with command line shells and utility interfaces, for software compatibility with variants of Unix and other operating systems.

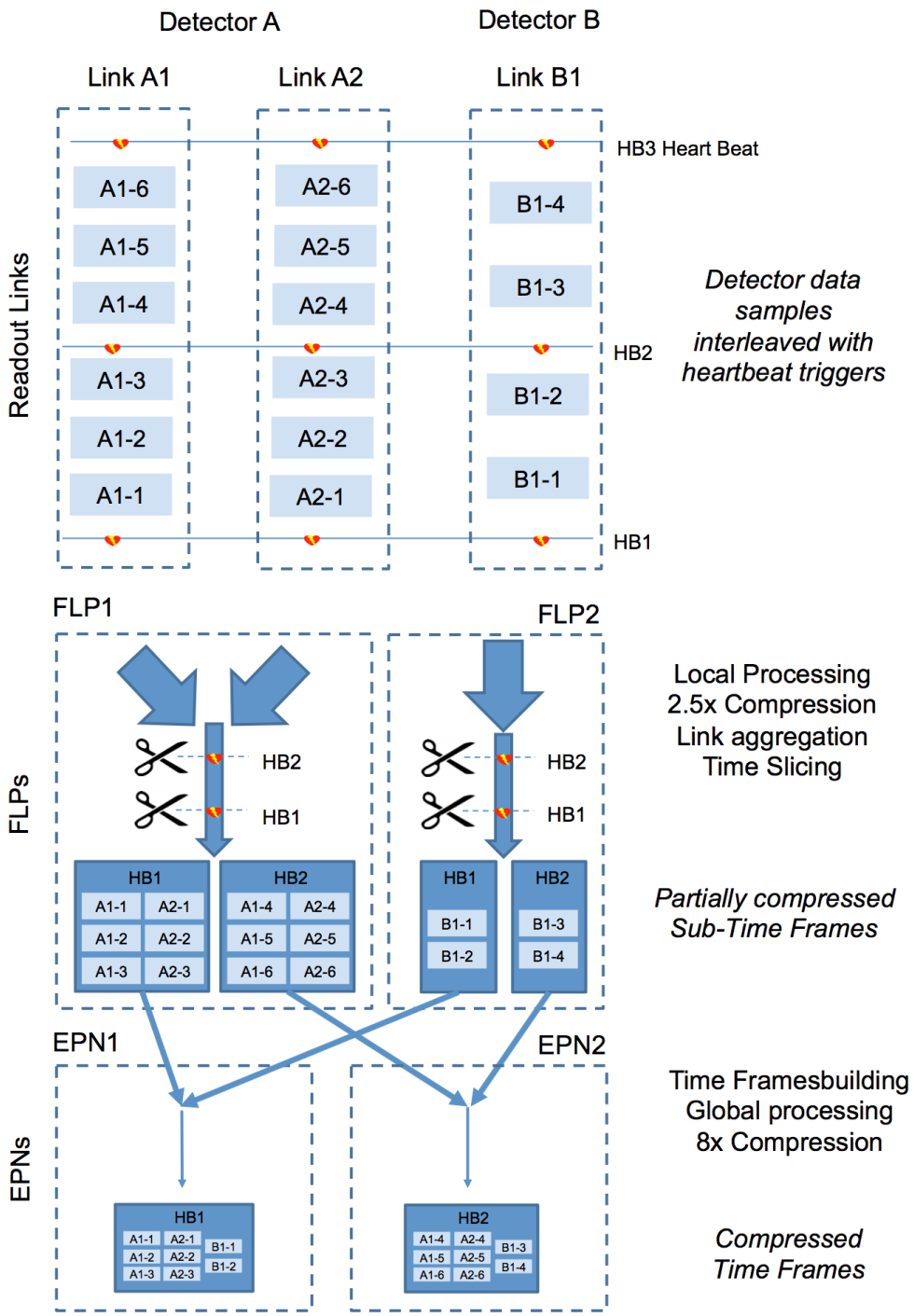

FIGURE 4.3 Sketch representing the acquisition flow with two detectors, A and B. The detector data samples are retrieved by the read-out logic in a continuous fashion, with the addition of heartbeat triggers interleaving for time stamping purposes. At the FLP level each data stream is time sliced, obtaining several patches which are compressed by fast processing and packed in sub TFs. The sub TFs are sent to the EPN farm and then aggregated into global TFs. Each TF has a full set of information regarding a given time interval. A global compression of around $\times 14$ is achieved in the process. From [16]

the whole data structure. The raw data format cannot be made persistent during acquisition, therefore the raw data flow will be converted in the much more compressed TF format.

The data stream of each detector are sent to the First Level Processor (FLP). At this level, only the information of one single detector or even part of it is available. The data format is therefore called Sub-Time Frame (STF). The processed data are then sent to the Event Processing Node (EPN), which collects the information of all detectors and aggregates them in the TF. The processing schema is shown in Fig. 4.4.

The TF data format requires all the data to be correctly time flagged, in order to be able to correctly aggregate data within the TF they belong to. For this reason the detectors raw data flows are interleaved with an heartbeat clock that can be used to attribute a time stamp to the detector data samples.

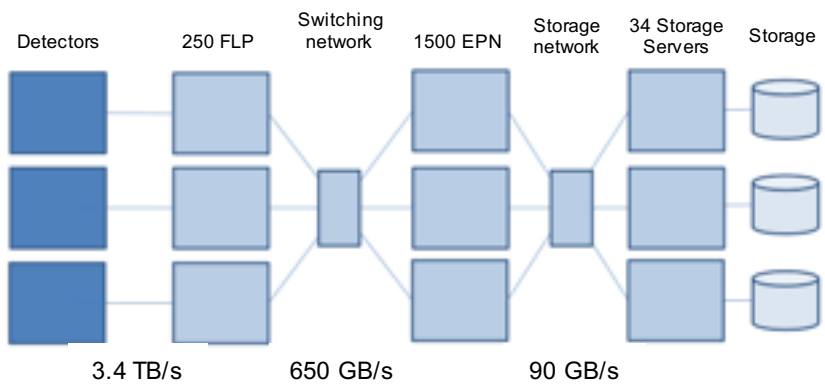

FIGURE 4.4 Computing infrastructure layers with quoted required input and output bandwidths. An overall factor of compression of ≈ 14 is to be achieved in the process. The network topology is not yet defined by the O^2 Technical Design Report since the technology growth is fast enough to require a shorter term planning later during the upgrade. From [16]

A total compression of around ≈ 14 [98] will be possible from the raw data to the storage elements and the first persistent format.

The validity interval of the TF, also called duration, has to be tuned taking into account several criteria :

— the TPC drift time causes a loss of $0.1/t_{TF}$, with t_{TF} expressed in ms, therefore a longer TF is better in this respect ;

— the TF should be a multiple of the shortest calibration update period. This value should be the TPC Space Charge Distortion one, scheduled each 5 ms ;

— in order to better balance the processing at the EPN level a shorter TF would be better. For the EPNs a buffer of at least three TFs (one receiving, one processing, one sending) is required to avoid dead times.

Given these requirements, the current understanding is that the TF will be limited to $\approx$ 23ms which corresponds to 256 beam orbits. The number of events packed inside a single TF will reach 1000 interactions in normal running conditions (Pb-Pb 50 kHz). The resulting TF size will be of $10GB$ on the EPN before compression and the unusable data because of the TPC drift time will be the 0.5% of the total. Since the EPN farm will be composed by 1500 machines, each EPN will receive a new TF to process every 30 s.

4.4 Data Processing Layer

The tools provided by the default O^2 project are intended to be used by experts and require coding skills which are not typical for the physicists community. In particular the tasks are wrappers of part of a bigger algorithm and from now on they will be referred to as devices. They are fully described by a bunch of specifications, summarized below :

1. The specification of inputs is composed of the indication of the channel of delivery and the kind of data. It is necessary to correctly connect and feed the algorithmic item wrapped in the device. Some devices could be input-less (e.g. MC wrappers, clock generators). A complete set of inputs will be referred as "work item" ;
2. The internal state of the device, a set of variables capable of keeping information across several work items. This can be useful for distributed pseudo-random number generators, event counters, histograms and in general any kind of accumulation of results. The initialization of the internal state can be complex without affecting the online performances of the device. In addition some devices, for example those involved in pipeline computations, are "stateless devices", namely devices which do not need to keep a memory of previous computations. Such devices have no internal state ;
3. The computation specification is the algorithm that is called and executed on each complete set of inputs. Any optimization effort has to be put to this part of the device specification, since it represents the main bottleneck being executed in a loop-like fashion. This element is required for any device ;
4. The specification of outputs is similar to that of the inputs and consists of the indication of the channel on which the data has to be sent as well as the type of data.

In this approach each device has to implement one and only one basic function. The devices are intended to be self contained and atomic. This opens up the possibility to spawn device clones or to kill unused devices to free resources for other tasks. For example if a given device (or a group of homologous devices) starts starving (*e.g.* the CPU set waits for data since the computation is too fast with respect to the data flow) and a loss of computing efficiency is measured, it might be killed by a manager process. Similarly if a group of devices cannot cope with the input rate, the manager process can add some more in order to improve the throughput of the whole set of devices using the resources freed up by the killing of starving devices.

Within the FairROOT framework, several utilities and libraries have already been implemented to simplify the configuration of new devices. In O^2 the description of the devices is even more trasparent to the end user thanks to an additional framework called Data Processing Layer (DPL). The DPL hides much of the complexity required by the MPI-like FairROOT devices. After some development efforts, the residual complexity left to the programmer by the DPL is negligible. Using advanced C++ techniques, available in the 11, 14 and 17 standards, the description of input and output channels is similar to the initialization of a list, while implementing the initialization and data processing functions is as complex as the required algorithm itself. The typical complexity of concurrent computing software framework is almost completely hidden, leaving much of the coding focus to the algorithmic part. During my thesis, I also participated in the effort of writing high level routines that can be easily adopted by the DPL framework to simplify the serialization of the messages. Such routines, based on `boost`, were extensively tested and are currently used many detector and subsystem-specific code and are requested to be included in the FairROOT core by its developers team.

The DPL approach is being adopted by most part of the detectors and the systems included in the O^2 upgrade project, and the upgraded muon trigger software follows this schema.

4.5 Muon tagging algorithm

The pre-upgrade offline muon tagging algorithm was intended to be executed during reconstruction, in an asynchronous computing model. Within the O^2 upgrade this algorithm will be modified to be fed with information computed synchronously, thus strongly improving the muon tagging capabilities of the system. It is based on the matching between tracks reconstructed in the muon tracker and the tracklets (straight tracks) reconstructed in the MTR. The tracks reconstructed within the muon chambers are obtained using a Kalman Filter algorithm. Since the five stations of muon chambers are placed upstream, inside and

downstream of the dipole magnet, the reconstructed tracks are curved. The reconstructed tracks are extrapolated towards the muon trigger system. These pieces of information are then matched with the tracklets generated using the MTR data. The muon identification criteria is based on the fact that only the muon chamber tracks which are found to correspond to a muon trigger one are to be considered muons, since it is unlikely for other particles to cross the 1.2 m thick iron wall between the two stations of the muon trigger (Fig. 4.5).

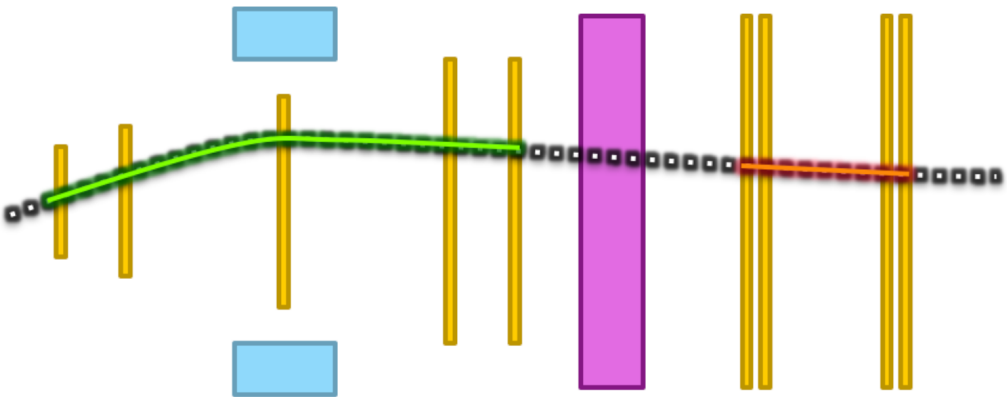

FIGURE 4.5 In this picture the muon chamber and muon trigger planes are represented in yellow, the iron wall in purple and the dipole is shown in blue. The dashed line represents the true trajectory of the muon. The green line is the reconstructed track within the muon chambers, while the orange line is the tracklet reconstructed in the muon trigger.

The generation of the tracklets in MTR was based on the MTR trigger algorithm, which is in turn based on the Local Boards, which collect the information of the fired strip in a projective region in the four detection plane. When a particle fires a strip in the first chamber, the local board searches for aligned strips in the other chambers, combining the information of the adjacent local boards in the bending plane. From this information the algorithm computes a hit position in the first chamber and a deviation, i.e. a tracklet. This algorithm, however, provides at most one response (and therefore one tracklet) per local board. In the case where more than one track crosses the same local board, the algorithm is tuned to chose the combination of hits providing the minimum deviation (i.e. largest p_{T}) in order to keep the highest trigger efficiency. This however might result in a reconstruction of just one track, as shown in figure 4.6, or of a fake track that does not match any of the two real tracks. This limitation affects the most central heavy-ion collisions, where the large particle multiplicity results in a larger probability of having two muons crossing the same LB. The inefficiency was then caused by an algorithmic feature more than by the detector itself.

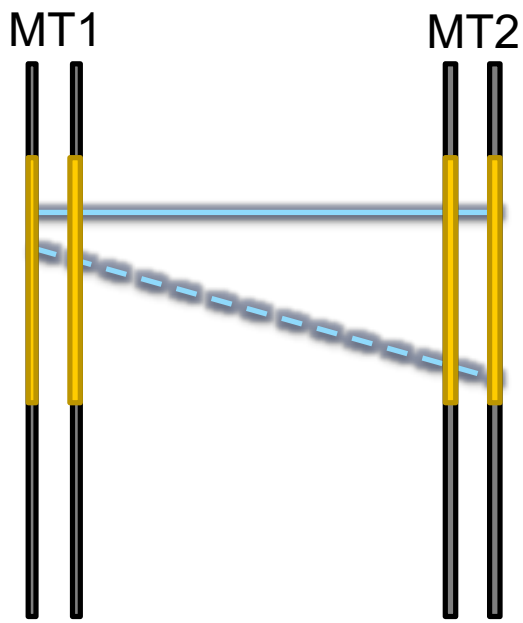

FIGURE 4.6 The MTR planes are shown in grey, while the hit local board is highlighted in yellow. Two real trajectories are represented by the lines. The algorithm is tuned to select the less sloped track in case of ambiguity, hence only the solid blue track would be recorded.

Some development of an algorithm capable of recovering the performance loss in the most central events was performed but never put in the production code. The complex solution of implementing a tracking algorithm in using the former MTR, excluded for RUN2, was indeed the proposed solution for RUN3 running conditions.

4.6 From Muon TRigger to Muon IDentifier

In the Run3, the MTR will lose its functionality of a triggering detector [3], and it will only be used to provide muon identification. Its name will be changed accordingly to reflect the change of functionality, thus passing from Muon TRigger to Muon IDentifier (MID). The muon identification (and hadron rejection) task will be performed combining data coming from the MCH and MID detectors. The addition of the Muon Forward Tracker (MFT) [90] will improve the tracks resolution closer to the interaction point and make it possible to resolve secondary vertexes. The tracks reconstructed with MCH data will be identified as

3. although the possibility of providing a very basic trigger was kept in the electronics, mainly for studying muon production in ultra-peripheral Pb-Pb collisions

muons if a compatible track in the MID detector is present. Even if the original idea at the base of the O^2 project was to perform an online reconstruction for all detectors and systems, the paradigm has been changed since the efforts needed for such implementation were difficult to sustain. Nowadays the common approach is to perform online computations only if they can lead to a compression of output data. Given the MID is a fast detector, the presence (absence) of detected particles could be evaluated online and used to decide to keep (discard) MCH data. Such decision would both avoid the CPU-heavy task of performing the tracking algorithm on MCH data and reduce the throughput of the MCH. For obvious reasons this MCH data rejection technique must be hot-plugable, in order to allow to perform systematic tests without this selection at the beginning of the data taking. The acquisition/reconstruction workflow is represented in figure 4.1. Data recorded by the FEE will be acquired via several GBTx link by the Common Readout Units (CRU), each one processing one half of the MID (inside and outside). The CRUs are implemented as PCI express boards equipped with two external GBTx ports and an on-board Altera Arria X FPGA. The CRUs will be installed in two dual CPU machines called First Level Processors (the FLPs) which will be placed in the counting rooms placed over the ALICE cavern, as close as possible to the detectors. The CRUs will perform the coding of the input stream in a binary format which can be sent and processed by the FLP (Fig. 4.7). Zero suppression and noisy/dead channels detection/suppression will be performed by the CRU. Finally, at the EPN level, the combination of MID data with data coming from other detectors will be possible.

4.7 MID raw data format

The MID data format follows the directives of O^2 for what concerns the description of the payload by means of headers. A top level header defines the binary intervals at which what kind of information is found and constitutes a constant size overhead. The management of data inside the binary payload follows a tree pattern. At each branching of the pattern a description (header) describes the positions of the following branches. In turn each branch provides a self description needed to deserialize and decode the content. The data format requires a sequential access in order to correctly map its content to meaningful variables and structures. The data format has an implicit zero suppression, since only the hit strips are coded in a bit pattern which is then sent.

Each side of the MID serializes the information using as top level header the number of fired RPCs, which corresponds to the number of following branches. Each branch representing an RPC provides an header which quotes the RPC ID and the number of columns fired within that RPC (see Fig. 4.8). Another branch level represents each of the fired columns and for

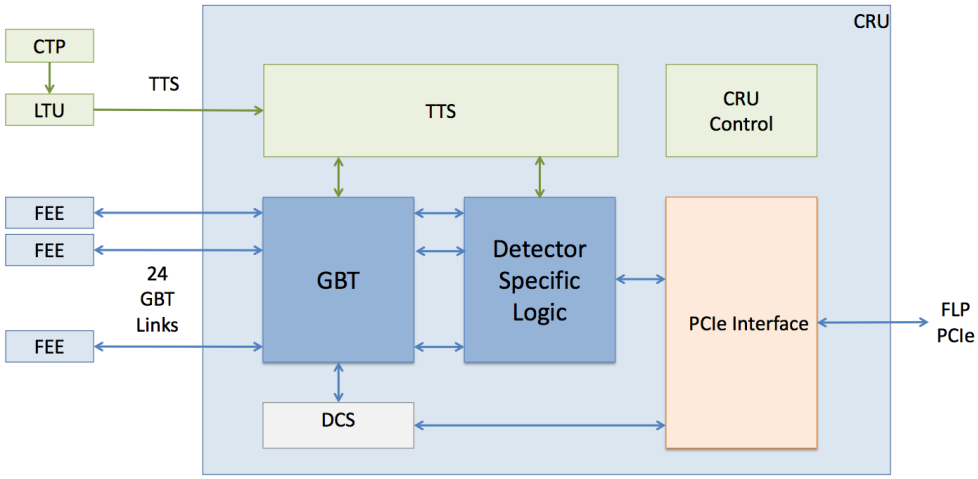

FIGURE 4.7 Detailed sketch of a generic Common Readout Unit (CRU). The Front End Electronics (FEE) are connected to the CRU through 24 embedded GBT links. The green boxes are connected to the Central trigger Processor (CTP) and deliver timing information to time tag the raw data flow, performed by the detector specific logic. The raw data is translated in a binary format which can be processed by the FLP CPUs. The ouput of the CRU is performed by a standard PCI Express link. From [16]

each column both the column ID and the number of fired Local Boards (LB). The deepest branch level represents the LBs by giving the LB ID and the bit patterns of the LB. The patterns correspond to strip in the bending and non-bending direction. It is worth noting that the non-bending strip can cross several local boards, so each pattern is a copy, in that local board, of the non-bending information. In an alternative proposal, the non-bending information is stored only once per column (see Fig. 4.8 bottom). The advantage is that the information is not replicated, but in this case any mismatch in the local copy of the NB strip needs to be monitored at the CRU level. It is also worth noting that all of the patterns are coded in 16 bits, although some LBs are equipped with only 8 strips in the NB direction. In that case the pattern gets filled accordingly to the hits and the exceeding bits are set to 0.

As already stated, the MID RPCs require to perform two kinds of calibration events in order to detect problematic channels. The issues can be either channels which starts to count continuously because of a discharge in the chamber or channels which stops counting because of detector or electronics failures. The characteristics of the two kinds of calibration events are intended to address the detection of both issues. In one case the read-out of the detector is triggered asynchronously with respect to an interaction. In the absence of a cosmic

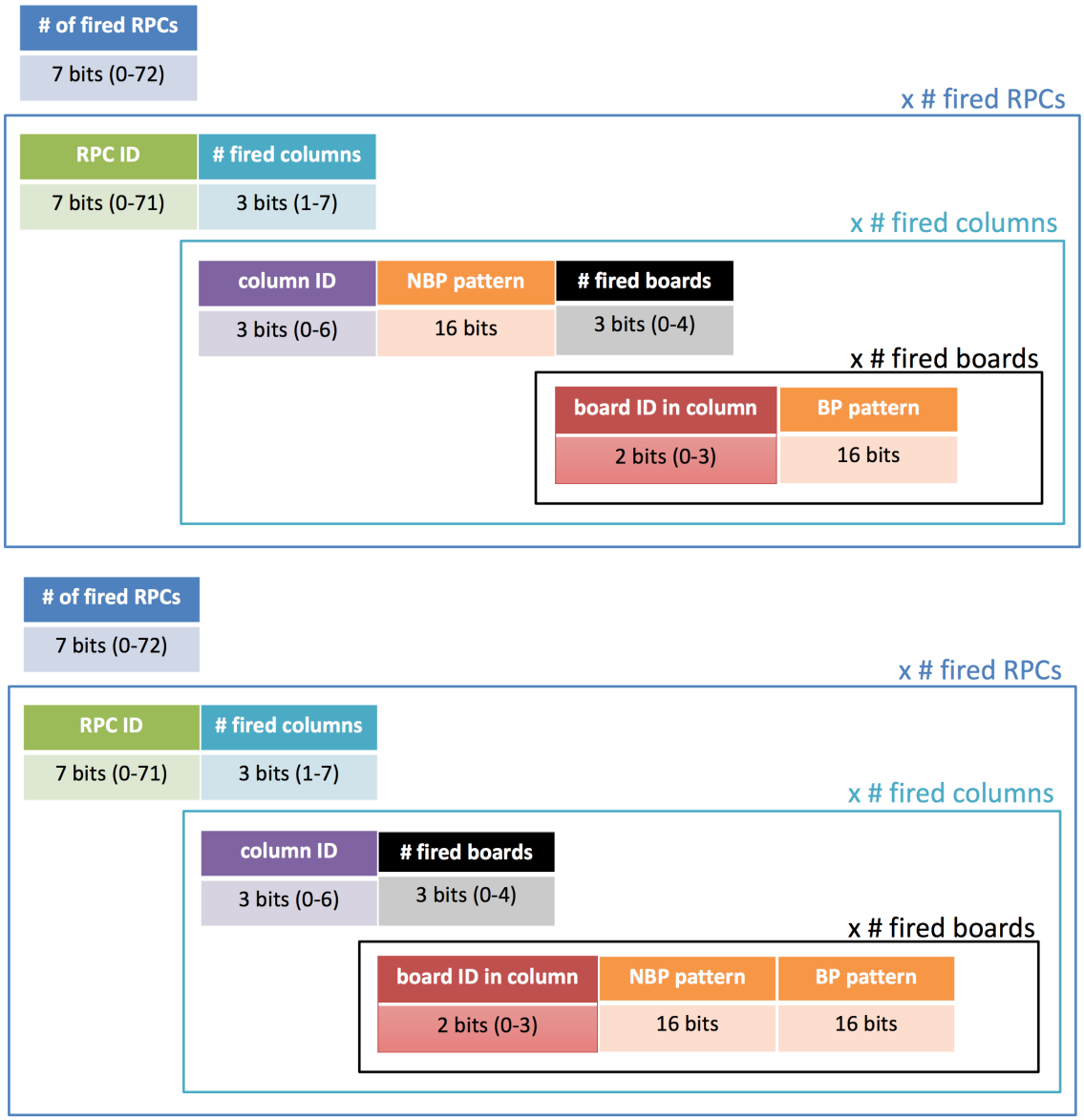

FIGURE 4.8 Two CRU data format proposals. In the first option only one non bending pattern is sent from the CRU to the FLP, while the FEE sends to the CRU several copies of the same pattern since the horizontal strips are read by several local boards each. The CRU has to perform some operation in order to combine the multiple non bending plane patterns into a single one. The second format foresees to send to the FLP several non bending plane patterns, which are combined by the FLP itself.

event, only noisy channel will respond in this case. In a second case, the FEE injects charge above the threshold in all channels to check whether they are responsive or not. During this calibration event all the strips are stimulated, therefore expected to be counting. This allows one to detect the presence of dead channels. The chosen MID raw data format is not efficient for the second kind of calibration event. In fact, since the dead channels are expected to be a small part of the total, during such events the bit patterns of almost the whole detector should be transferred. In order to optimize the data delivery process, by reducing the amount of useless information being sent, an additional bit can be delivered in order to flag the message payload as "straight" or "inverted". In the first case nothing changes and the overhead of the data format would be increased of 1 bit. In the second case only the dead channels are sent as if they would have been the only channels switched on. Thanks to the additional bit, the decoder will be able to invert the message to obtain the correct information.

4.8 MID reconstruction pipeline

The MID reconstruction pipeline is an algorithm which, from a global point of view, should convert the digits streams obtained from the CRUs to a stream of 3D tracks representing the detected muons. The digits stream coming from the CRU is decoded and, in case of the special software trigger, the noisy and dead channels are computed. The detection of noisy channels will allow for the generation of a mask that will have to be transferred to the local boards. This is fundamental because the presence of noise increases the bandwidth from the detector readout to the CRU, eventually leading to a saturation. The details of the transfer, however, are still under investigation. The information on dead channels and masks needs to be permanently stored so that it will become available for simulation and efficiency evaluation purposes. This will most likely be done in the Condition DataBase (CDB). Moreover, the detection of dead and noisy channels will be the first step of the Quality Control (QC) of the detector, since it allows one to pinpoint hot spots and dead zones of the RPC chambers. The reconstruction steps for the MID are intended to be mainly (if not globally) executed on the detector FLPs. The MID will be equipped with one FLP per side (inside and outside) which won't be equipped with a cross connection, hence won't be able to exchange data. For this reason the MID has to be considered as a pair of independent detectors. Only at the EPN level data coming from both sides will be merged and combined.

Regarding the acquisition, some logic steps to perform the conversion have been defined, in order to provide atomic computation items able to be packed in deployable and modular devices :

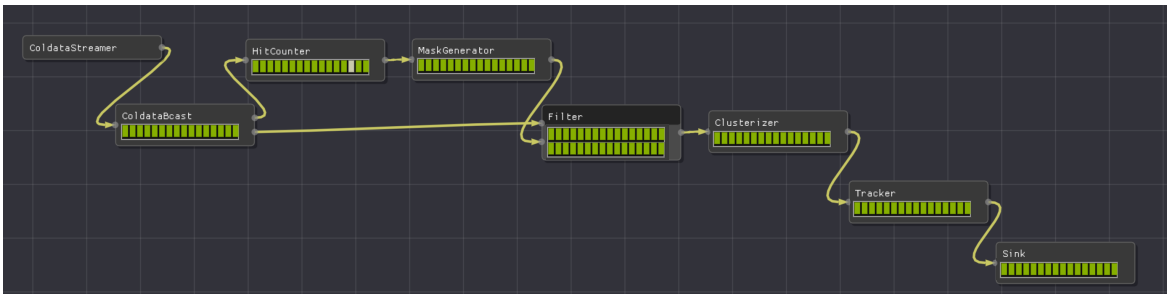

FIGURE 4.9 Schema of the MID reconstruction workflow obtained from the DPL Graphic User Interface (GUI). This workflow is intended to be executed in the FLP. Each box represents a device and the arrows represent a data stream. The first device, called ColDataStreamer, is a random generator of fake CRU messages able to emulate the CRU behaviour for testing purposes. The upper branch represents the asynchronous mask computing stage of the workflow. The last device, called sink, represents the connection to the EPN nodes and the second online processing step.

— the digits coming from the CRU are cloned towards two branches. The first branch leads to the mask generation and can be asynchronous with respect to the input data flow. The second branch has to present limited latency to avoid starvation of the following reconstruction devices ;
— the mask generation branch begins with a rate computer, namely a device with an internal state which works as a per-strip counter. Two counter sets are available, one for the noisy and the other for the dead channels, incremented during the corresponding special events ;
— a mask generator devices reads the recorded counters and spots dead and noisy channels by looking at the scalers incremented during calibration runs. The mask is sent to a filter device ;
— a filter device is capable of applying the mask to the incoming digits. The application of the mask is the logic AND between the incoming patterns and the corresponding mask. In case no mask is present, or the mask is empty, the digits should simply be passed through as fast as possible. Achieving the lowest latency on this device is crucial ;
— the stream of masked digits is then processed by a clusterizer device. The binary digits are here converted to 2D clusters, computing the centroids of the hits clusters. This computing step is a typical high throughput stateless computation ;

— the 2D clusters in the local RPC reference frame are passed to a device that converts it in 3D clusters in the global reference frame and preforms the tracking through a Kalman Filter algorithm. The generated tracks are sent to the following reconstruction steps executed by the EPNs.

The MID reconstruction pipeline has been developed within the DPL framework. A schema of this pipeline, as provided by the DPL Graphical User Interface (GUI) itself, is shown in 4.9.

4.9 MID reconstruction performances

The MID reconstruction algorithm is new compared with what was used for MTR, which was entirely based on the trigger algorithm. Both the clustering and the tracking algorithms need to be validated in Monte Carlo (MC) simulations. The framework for MC simulation for MID is work in progress, but, since the detector geometry and segmentation did not change with respect to MTR, the Run2 simulation can be used for the validation of the algorithms. In particular, a custom MC production using a J/ψ parametrization as input is used. The crossing points of the tracks in the RPCs are used by the MID digitizer algorithm to generate the digits on which the MID reconstruction chain is applied. The reconstructed clusters and tracks are then compared to the MC impact point and track parameters to estimate the residuals. The final aim is to study :

— the resolution of the algorithm in four variables :
  — the cluster residuals (along x and y) ;
  — the track resolution, i.e. the resolution on the track position (mainly along x and y) and slopes along the bending and non bending plane ;
— the muon reconstruction efficiency ;
— the fraction of fake tracks, i.e. tracks reconstructed with the wrong parameters by mixing real hits from different particles or noise. The study should be performed as a function of the particle multiplicity in the MID chambers.

Some of these quantities have already been studied in details and the results will be presented in the following. The methodology for the studies that are not accomplished yet will be discussed as well.

4.9.1 Cluster residuals

The MID electronics does not provide any information on the deposited charge. For this reason, a charge centroid cannot be computed and the cluster centroid is purely geometrical.

The centroids coordinates are computed as the average of the coordinates of the strips. Since a flat distribution of crossing probability has to be assumed within the cluster extension, the resolution is directly proportional to the cluster extension via the relation $\frac{CS}{\sqrt{12}}$ where CS is the cluster size.

The performance of the algorithm has been evaluated running the reconstruction on simulated data. The cluster residuals between the reconstructed clusters and the generated clusters have been computed and represented in form of a distribution. The residuals distributions are generated as a function of the detection element ID (i.e. the RPC). Such distributions present some square shaped structures which are artifacts caused by the different strips pitches. In fact, while the RPCs closer to the beam line are equipped with strips 1, 2 and 4 cm wide, other RPCs are equipped only with 2 and 4 cm or only with 4 cm strips. The residuals distribution is symmetric with respect to the 0 and the x (y) RMS is 0.9 (0.8) cm. The distribution plots of the residuals are reported in figure 4.10.

4.9.2 Track residuals

Another set of residuals has been computed comparing the generated information to the reconstructed tracks. In this case all the tracks are described by three spatial coordinates for the crossing point in the first chamber and two deviations, one along x, the other along y. The residuals between such parameters have been computed and shown as a function of the position within the RPCs as well as from the kinematic parameters of the track. This test can be performed using simulated muon tracks for RUN2.

The tracking algorithm is applied to the set of digits and the reconstructed tracks are recorded in the form of a 3D crossing point on the first MID station and a 2D slope. The residuals distributions of cluster positions and tracks comparison are generated as a function of the detection element (i.e. the RPC) and of the generated total momentum p of the particle.

The spatial resolution along x and y are shown in figures 4.11 and 4.12 respectively, as a function of the generated total momentum of the particle. The residuals normalized on the residual uncertainty are shown in figure 4.13. Most of the measurements are within 3 sigmas as expected, except for extremely low momenta particles. The distribution gets narrower moving to higher p particles. It is worth noting that the binning of the histogram varies versus p, in particular going from 1 GeV/c to 2 GeV/c for $p = 20$ GeV/c. Both distributions are centered at 0 cm. As expected, considering the detector morphology, the vertical resolution (0.4 cm) is better than the horizontal one (0.7 cm). The spatial resolutions are reflected in the slope resolutions. In order to better understand the angular resolution, the distribution is shown as the residual divided by the uncertainty that is automatically calculated by the

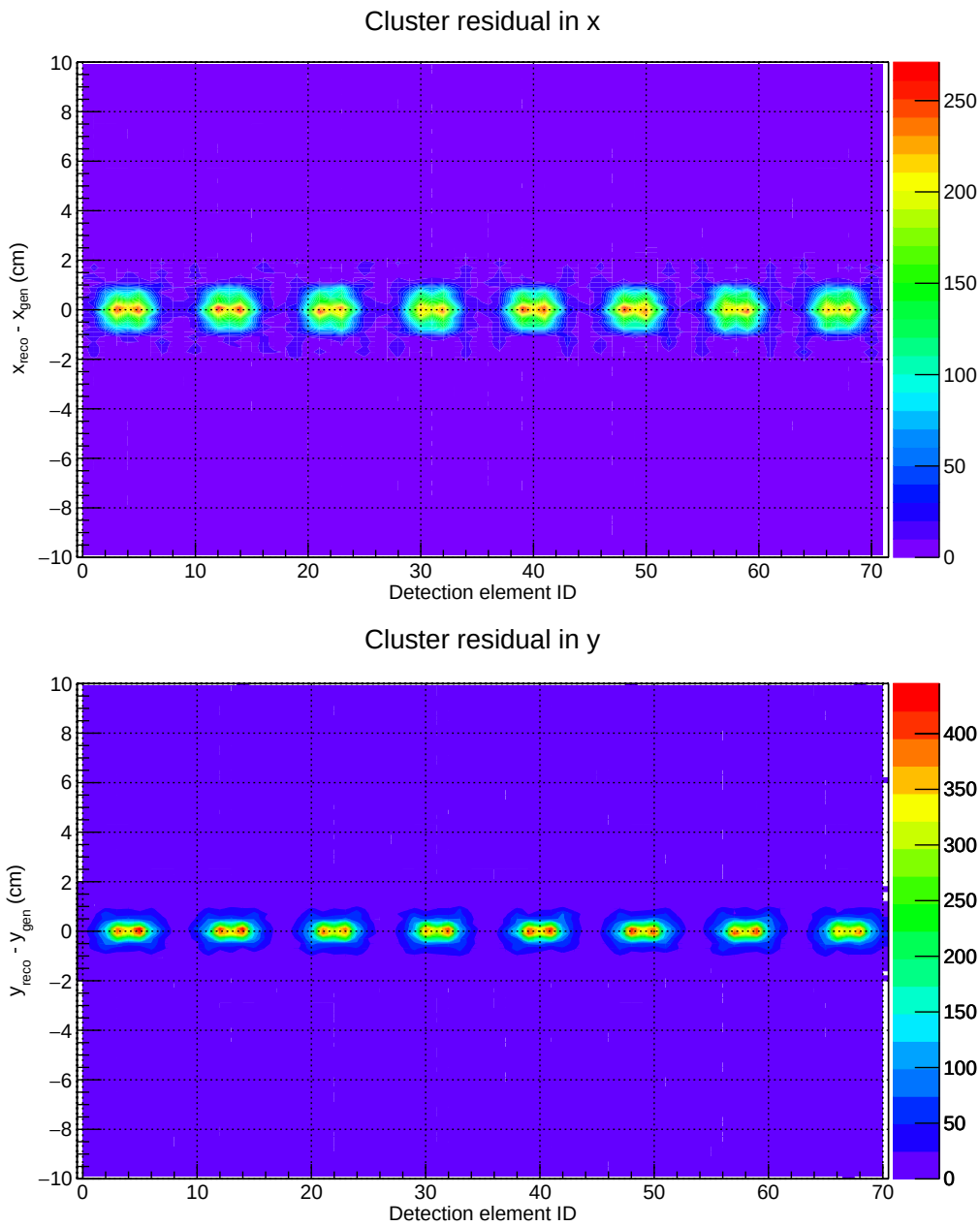

FIGURE 4.10 Cluster residuals distribution as a function of the RPC ID. The y bins are continuous values, while each x axis bin represents a single RPC. The square shaped artifacts are related to the different strip pitches each RPC is equipped with. The RPCs equipped with strips down to 1 cm wide present the hot spots due to the superposition of the residuals distributions of 1, 2 and 4 cm wide strips. The y distribution presents smaller structures since the average strip size is smaller. Each RPC distribution is not normalized on its irradiation hence the colour palette is the same for all the RPCs.

Kalman filter. Up to the 95% of the distribution is within the ± 1.96 band in the vertical slope distribution. The distribution gets physiologically broader at lower p_T.

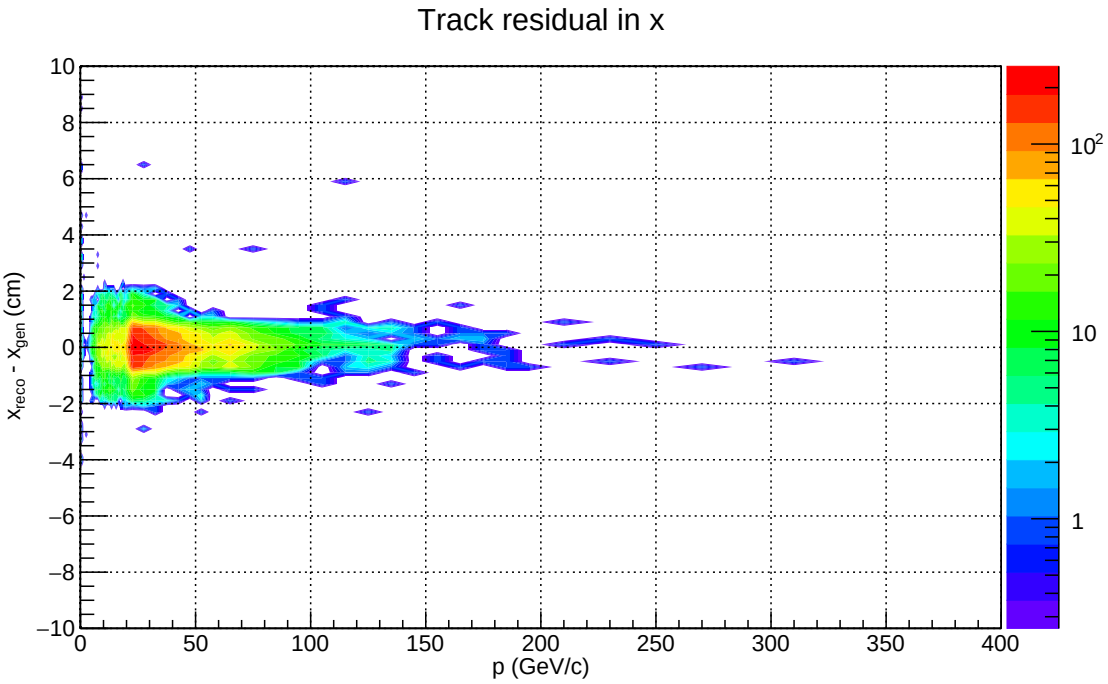

FIGURE 4.11 Track residuals distribution of the horizontal coordinate. The y axis represents the residual expressed in centimeters, while the x axis is the generated momentum of the particle. The colour palette is in logarithmic scale. The core of the distribution is about 1 cm wide and very few outliers cross the ± 2 cm band.

The overall resolution presents a clear dependence with respect to the particle momentum. The result is already rather good, but it is worth noting that the algorithm is not yet fine tuned and the resolution at very low p_T could be further improved. The fine tuning of the algorithm has not yet been performed and such optimization could help solving the issue.

4.9.3 Tracking efficiency

The measurement of the algorithm resolution is not the only crucial test for a new tracking method. An algorithm might present exceptional resolution on a negligible fraction of the processed tracks. For this reason the evaluation of the tracking efficiency, defined as the ratio between processed particles and reconstructed ones, is crucial. The tracking efficiency was estimated using the same MC as the one used for the residuals. The results of this study are reported in figure 4.14. The measured efficiency is very close to unity. Some bins at very

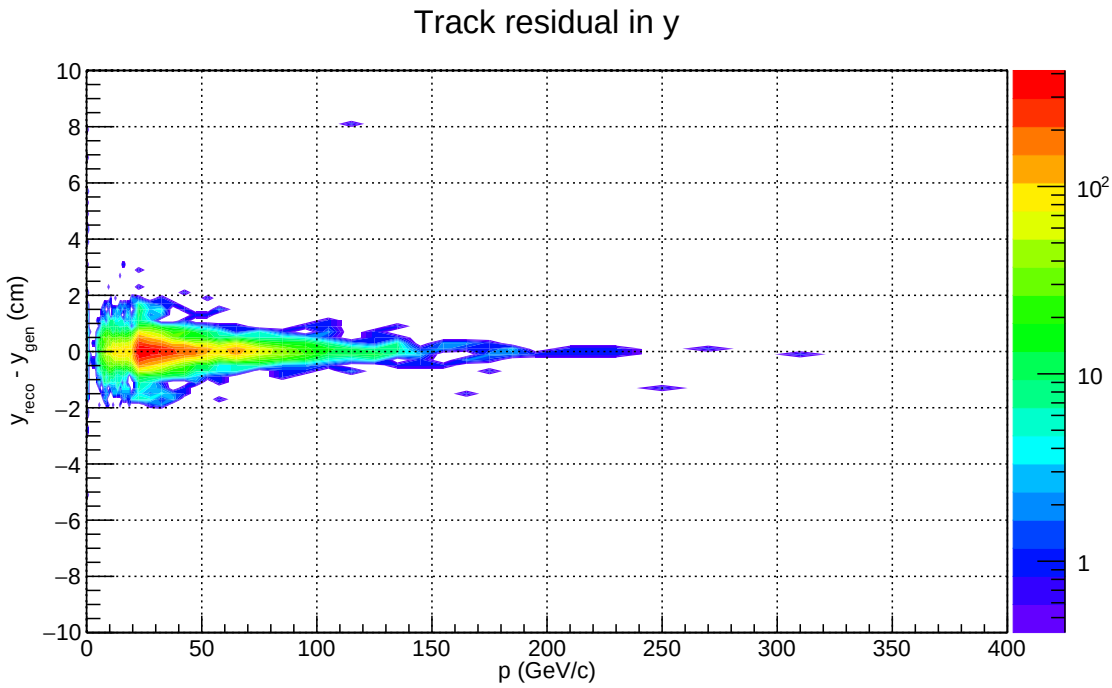

FIGURE 4.12 Track residuals distribution of the vertical coordinate. The y axis represents the residual expressed in centimeters, while the x axis is the reconstructed momentum of the particle. The colour palette is in logarithmic scale. The core of the distribution is about 0.5 cm wide and like for the horizontal coordinate, very few outliers cross the ± 2 cm band.

high p_T and/or at the edge of the muon spectrometer η acceptance, show an efficiency drop [4]. The study should be repeated in the future with simulations embedded in real events in order to assess the efficiency of the algorithm at high particle multiplicity.

4.9.4 PID characterization

The PID performance of the new algorithm has to be evaluated.

First of all the PID efficiency has to be computed. This characteristic of the algorithm corresponds to its matching probability. Such measurement can be performed evaluating how many true muons are matched with muon tracker data, hence correctly flagged. Using Monte Carlo simulations one can measure such fraction computing the ratio between reconstructed muons and reconstructible muons. A reconstructible is a muon which has been generated within the muon spectrometer acceptance and produced hits in both MCH and MID. For

4. Entries at zero efficiency mostly correspond to p_T and y bins where no generated muon fell in.

what concerns MID the requirement is that a hit (both x and y) in at least $3/4$ planes was detected. In case of missing bending or non-bending information on more than $1/4$ planes the tracking resolution will drop considerably. Concerning MCH the requirements will stay the same as in RUN2 : at least $1/2$ plane hit in each of the three inner stations (1, 2, 3) and at least $3/4$ planes hit for the two remaining stations (4, 5).

Secondly the fraction of mis-identified particles should be computed as well. Some particles which are not muons are detected and reconstructed in the MCH. If they get matched with some MID tracklets then become wrongly flagged as muons. In order to evaluate this mis-identification probability one should compute the ratio between the number of non-muons matched in the MID and the number of non-muons reconstructed in the MCH.

Both these characterizations have not been performed yet.

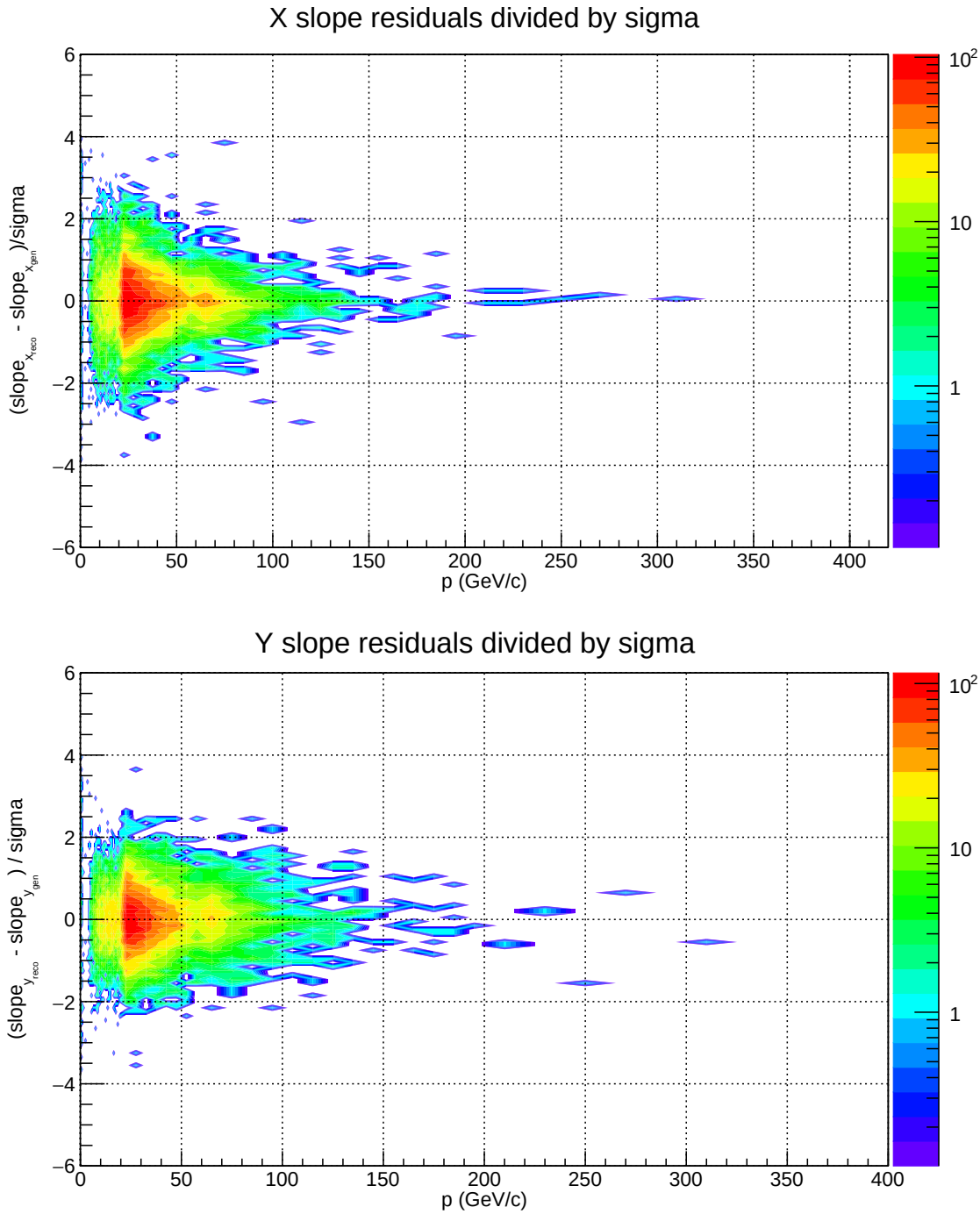

FIGURE 4.13 Residuals of the vertical and horizontal slopes evaluation between the old MTR's algorithm and the new MID's one. The values are represented as residuals (y) divided by sigma as a function of the reconstructed particle momentum. The colour pallette is represented in logarithmic scale.

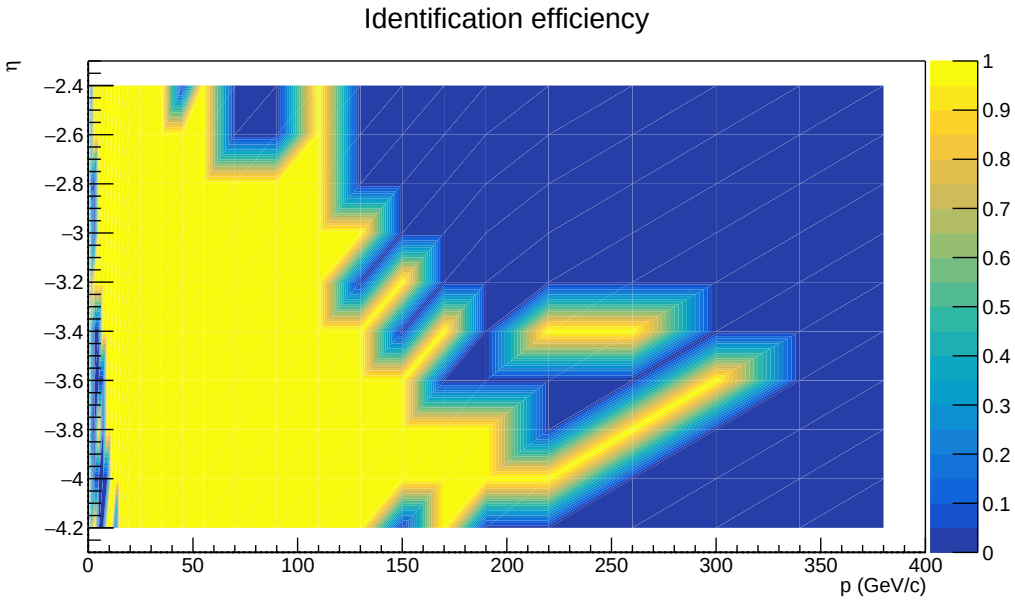

FIGURE 4.14 Tracking efficiency computed as the ratio between the numbers of reconstructed and generated tracks.

Chapitre 5

Conclusions

The aim of this thesis is the study of quarkonium production in heavy-ion collisions, as performed with the muon spectrometer of the ALICE experiment at the Large Hadron Collider. Three different aspects have been tackled within the thesis. First, a study has been performed of the long-term evolution during the LHC RUN1 and RUN2 of a few relevant parameters for aging effects in the muon trigger detectors (Resistive Plate Chambers) : the integrated charge, the dark current and the dark rate. In order to do this, a new framework was developed, able to combine several sources of data. It has been developed as an extension of the AliROOT `Shuttle`, which is in charge of transferring parameters related to the detector and the accelerator to the Offline Condition Database (OCDB). The new tool, called `MTRShuttle`, allows one to combine the OCDB information with the data from the Detector Control System (DCS). The main result of the study is that an increasing trend of dark current is observed for a non-negligible fraction of detectors. Although this effect is not accompanied by a decrease of the efficiency, the status of these chambers shall be monitored and replacement may be considered. Further studies to understand the origin of the dark current are also recommended. In view of the increased luminosity of the LHC RUN3, one RPC has been equipped with a prototype for an amplified front-end electronics, allowing for low-gain operation of the RPC. The study of its parameters has shown a more stable dark rate and dark current, and a much smaller integrated charge, which is a promising result. The functionalities of the developed framework may be extended to other ALICE systems in the future. Second, the study of bottomonium production at forward rapidity in Pb-Pb collisions at $\sqrt{s_{\mathrm{NN}}} = 5.02$ TeV, in the dimuon decay channel, has been performed. Data collected during the LHC RUN2 were analysed, and the nuclear modification factor of the $\Upsilon(1S)$ and $(2S)$ were measured, showing a clear suppression with respect to the properly scaled reference obtained in pp collisions. The suppression is larger for the $\Upsilon(2S)$, as expected in the hypothesis of a binding-energy dependent sequential suppression in a

Quark Gluon Plasma. For the $\Upsilon(1S)$, the measurement was also performed as a function of centrality, rapidity and transverse momentum. While the suppression increases with the collision centrality, no significant trend as a function rapidity and transverse momentum is observed within the present uncertainties. The measured nuclear modification factors are also compatible with those measured during the LHC Run1 at $\sqrt{s_{\mathrm{NN}}} = 2.76$ TeV. The results were compared to transport and dynamical model calculations, which qualitatively reproduce the centrality, rapidity and transverse momentum dependence. This thesis work led to an article, titled "Υ suppression at forward rapidity in Pb-Pb collisions at $\sqrt{s_{\mathrm{NN}}} = 5.02$ TeV"[99], that is currently submitted for publication to Physics Letter B journal. Third, a new muon identification software has been developed in light of the RUN3 upgrade of ALICE, and the associated software upgrade program called O^2. With this upgrade the data rate will go from 8 kHz to 50 kHz of minimum bias events in Pb-Pb collisions. The ALICE muon trigger (MTR) system will undergo a big upgrade process, involving the read out electronics and the whole software apparatus, allowing it to efficiently serve as a muon identifier (MID). In the context of this work a big effort has been put to develop a fast, precise and resilient software capable of coping with the LHC RUN3 conditions. As a result the ALICE MTR/MID will be able to retain most of its features and performances along with a highly improved rate capability. The development is still work in progress, but the boost given by this work is an important fraction of the planned tasks. A library, which allows for the transport of `C++` types and structures (and contiguous containers of such objects) using the ZeroMQ transport framework at the basis of O^2, has been implemented. These serialization routines, based on Boost have been widely tested and are currently used in many detector- and subsystem-specific code, and was requested to be included in FairROOT core by its developers team. The development of the O^2 software for the MID involved several work items. An algorithm capable of de-serializing the CRU data format in a `C++` structure has been implemented. Such algorithm will be probably implemented directly on the CRU FPGA for timing constraints. In addition, the development of a full stack of devices, capable of performing an online rejection of MID noisy channels and detection of dead channels, has been accomplished. This chain of devices has been implemented on top of the Data Processing Layer (DPL) framework. The interaction with DPL developers allowed for an improvement of the whole framework by looking to the real use case of the MID detector. Finally, preliminary tests of the performance of the new muon reconstruction algorithm for MID have been carried out, with promising results.

Bibliographie

[1] A. Jain, "Symmetries in particle physics," 07 2015.

[2] M. L. Miller, K. Reygers, S. J. Sanders, and P. Steinberg, "Glauber modeling in high energy nuclear collisions," *Ann. Rev. Nucl. Part. Sci.*, vol. 57, pp. 205–243, 2007.

[3] B. Abelev *et al.*, "Centrality determination of Pb-Pb collisions at $\sqrt{s_{\mathrm{NN}}}$ = 2.76 TeV with ALICE," *Phys. Rev.*, vol. C88, no. 4, p. 044909, 2013.

[4] D. Caffarri, "Open heavy-flavour and quarkonium production in Pb-Pb and p-Pb collisions measured by the ALICE detector at the LHC," in *Proceedings, 51st Rencontres de Moriond on QCD and High Energy Interactions : La Thuile, Italy, March 19-26, 2016*, pp. 273–276, 2016. [,273(2016)].

[5] J. P. Lees *et al.*, "Bottomonium spectroscopy and radiative transitions involving the $\chi_b J(1P, 2P)$ states at BABAR," *Phys. Rev.*, vol. D90, no. 11, p. 112010, 2014.

[6] B. B. Abelev *et al.*, "Suppression of Υ(1S) at forward rapidity in Pb-Pb collisions at $\sqrt{s_{\mathrm{NN}}} = 2.76$ TeV," *Phys. Lett.*, vol. B738, pp. 361–372, 2014.

[7] K. Oyama, "Reference cross section measurements with ALICE in pp and Pb-Pb collisions at LHC," in *LHC Lumi Days 2012 Geneva, Switzerland, February 29-March 1, 2012*, 2013.

[8] K. Aamodt *et al.*, "Alignment of the ALICE Inner Tracking System with cosmic-ray tracks," *JINST*, vol. 5, p. P03003, 2010.

[9] J. Alme *et al.*, "The ALICE TPC, a large 3-dimensional tracking device with fast readout for ultra-high multiplicity events," *Nuclear Instruments and Methods in Physics Research A*, vol. 622, pp. 316–367, Oct 2010.

[10] J. Adam *et al.*, "Determination of the event collision time with the alice detector at the lhc," *The European Physical Journal Plus*, vol. 132, 02 2017.

[11] W. A. Wenzel, "Recent developments in spark chambers," *IEEE Transactions on Nuclear Science*, vol. 13, pp. 34–45, June 1966.

[12] e. a. Arnaldi, "R&d on rpc for the muon trigger system for the alice experiment in view of p-p data taking," vol. 2, pp. 1265 – 1269 Vol. 2, 11 2004.

[13] X. Du, R. Rapp, and M. He, "Color Screening and Regeneration of Bottomonia in High-Energy Heavy-Ion Collisions," *Phys. Rev.*, vol. C96, no. 5, p. 054901, 2017.

[14] K. Zhou, N. Xu, and P. Zhuang, "Υ Production in Heavy Ion Collisions at LHC," *Nucl. Phys.*, vol. A931, pp. 654–658, 2014.

[15] B. Krouppa, A. Rothkopf, and M. Strickland, "Bottomonium suppression using a lattice QCD vetted potential," *Phys. Rev.*, vol. D97, no. 1, p. 016017, 2018.

[16] P. Buncic, M. Krzewicki, and P. Vande Vyvre, "Technical Design Report for the Upgrade of the Online-Offline Computing System," Tech. Rep. CERN-LHCC-2015-006. ALICE-TDR-019, Apr 2015.

[17] N. Cabibbo and G. Parisi, "Exponential Hadronic Spectrum and Quark Liberation," *Phys. Lett.*, vol. 59B, pp. 67–69, 1975.

[18] R. Hagedorn, "Statistical thermodynamics of strong interactions at high-energies," *Nuovo Cim. Suppl.*, vol. 3, pp. 147–186, 1965.

[19] M. G. Alford, A. Schmitt, K. Rajagopal, and T. Schäfer, "Color superconductivity in dense quark matter," *Rev. Mod. Phys.*, vol. 80, pp. 1455–1515, 2008.

[20] A. S. Kapoyannis and A. D. Panagiotou, "Particle states of Lattice QCD," *Eur. Phys. J.*, vol. C77, no. 11, p. 736, 2017.

[21] A. Dumitru and S. A. Bass, "Collective evolution of hot QCD matter from the QGP to freezeout," *AIP Conf. Proc.*, vol. 549, no. 1, pp. 359–362, 2000.

[22] A. Chodos, R. L. Jaffe, K. Johnson, C. B. Thorn, and V. F. Weisskopf, "New extended model of hadrons," *Phys. Rev. D*, vol. 9, pp. 3471–3495, Jun 1974.

[23] A. Chodos, R. L. Jaffe, K. Johnson, and C. B. Thorn, "Baryon structure in the bag theory," *Phys. Rev. D*, vol. 10, pp. 2599–2604, Oct 1974.

[24] S. Mukherjee, "Freeze-out Conditions from Lattice QCD," *Nucl. Phys.*, vol. A904-905, pp. 873c–876c, 2013.

[25] K. Aamodt *et al.*, "First proton-proton collisions at the LHC as observed with the ALICE detector : Measurement of the charged particle pseudorapidity density at s**(1/2) = 900-GeV," *Eur. Phys. J.*, vol. C65, pp. 111–125, 2010.

[26] T. Matsui and H. Satz, "J/ψ Suppression by Quark-Gluon Plasma Formation," *Phys. Lett.*, vol. B178, pp. 416–422, 1986.

[27] N. Brambilla *et al.*, "Heavy quarkonium : progress, puzzles, and opportunities," *Eur. Phys. J.*, vol. C71, p. 1534, 2011.

[28] A. Andronic *et al.*, "Heavy-flavour and quarkonium production in the LHC era : from proton-proton to heavy-ion collisions," *Eur. Phys. J.*, vol. C76, no. 3, p. 107, 2016.

[29] S. Digal, P. Petreczky, and H. Satz, "Quarkonium feed down and sequential suppression," *Phys. Rev.*, vol. D64, p. 094015, 2001.

[30] M. C. Abreu *et al.*, "J/ψ, ψ' and Drell-Yan production in S-U interactions at 200 GeV per nucleon," *Phys. Lett.*, vol. B449, pp. 128–136, 1999.

[31] B. Alessandro *et al.*, "A New measurement of J/ψ suppression in Pb-Pb collisions at 158-GeV per nucleon," *Eur. Phys. J.*, vol. C39, pp. 335–345, 2005.

[32] R. Arnaldi *et al.*, "J/ψ production in indium-indium collisions at 158-GeV/nucleon," *Phys. Rev. Lett.*, vol. 99, p. 132302, 2007.

[33] A. Adare *et al.*, "J/ψ suppression at forward rapidity in Au+Au collisions at $\sqrt{s_{\mathrm{NN}}} = 200$ GeV," *Phys. Rev.*, vol. C84, p. 054912, 2011.

[34] B. I. Abelev *et al.*, "J/ψ production at high transverse momentum in p+p and Cu+Cu collisions at $\sqrt{s_{\mathrm{NN}}} = 200$ GeV," *Phys. Rev.*, vol. C80, p. 041902, 2009.

[35] B. Abelev *et al.*, "J/ψ suppression at forward rapidity in Pb-Pb collisions at $\sqrt{s_{\mathrm{NN}}} = 2.76$ TeV," *Phys. Rev. Lett.*, vol. 109, p. 072301, 2012.

[36] S. Chatrchyan *et al.*, "Suppression of non-prompt J/ψ, prompt J/ψ, and Υ(1S) in PbPb collisions at $\sqrt{s_{\mathrm{NN}}} = 2.76$ TeV," *JHEP*, vol. 05, p. 063, 2012.

[37] J. Adam *et al.*, "J/ψ suppression at forward rapidity in Pb-Pb collisions at $\sqrt{\mathbf{s}_{\mathrm{NN}}} = \mathbf{5.02}$ TeV," *Phys. Lett.*, vol. B766, pp. 212–224, 2017.

[38] P. Braun-Munzinger and J. Stachel, "(Non)thermal aspects of charmonium production and a new look at J / psi suppression," *Phys. Lett.*, vol. B490, pp. 196–202, 2000.

[39] R. L. Thews, M. Schroedter, and J. Rafelski, "Enhanced J/ψ production in deconfined quark matter," *Phys. Rev.*, vol. C63, p. 054905, 2001.

[40] X. Zhao and R. Rapp, "Medium Modifications and Production of Charmonia at LHC," *Nucl. Phys.*, vol. A859, pp. 114–125, 2011.

[41] K. Zhou, N. Xu, Z. Xu, and P. Zhuang, "Medium effects on charmonium production at ultrarelativistic energies available at the CERN Large Hadron Collider," *Phys. Rev.*, vol. C89, no. 5, p. 054911, 2014.

[42] B. B. Abelev *et al.*, "Centrality, rapidity and transverse momentum dependence of J/ψ suppression in Pb-Pb collisions at $\sqrt{s_{\mathrm{NN}}}$=2.76 TeV," *Phys. Lett.*, vol. B734, pp. 314–327, 2014.

[43] J. Adam *et al.*, "Differential studies of inclusive J/ψ and ψ(2S) production at forward rapidity in Pb-Pb collisions at $\sqrt{s_{\mathrm{NN}}} = 2.76$ TeV," *JHEP*, vol. 05, p. 179, 2016.

[44] A. Mocsy, "Potential Models for Quarkonia," *Eur. Phys. J.*, vol. C61, pp. 705–710, 2009.

[45] B. Krouppa, R. Ryblewski, and M. Strickland, "Bottomonia suppression in 2.76 TeV Pb-Pb collisions," *Phys. Rev.*, vol. C92, no. 6, p. 061901, 2015.

[46] M. Martinez and M. Strickland, "Measuring QGP thermalization time with dileptons," *Phys. Rev. Lett.*, vol. 100, p. 102301, 2008.

[47] Y. Burnier, O. Kaczmarek, and A. Rothkopf, "Static quark-antiquark potential in the quark-gluon plasma from lattice QCD," *Phys. Rev. Lett.*, vol. 114, no. 8, p. 082001, 2015.

[48] K. J. Eskola, V. J. Kolhinen, and C. A. Salgado, "The Scale dependent nuclear effects in parton distributions for practical applications," *Eur. Phys. J.*, vol. C9, pp. 61–68, 1999.

[49] K. J. Eskola, H. Paukkunen, and C. A. Salgado, "EPS09 : A New Generation of NLO and LO Nuclear Parton Distribution Functions," *JHEP*, vol. 04, p. 065, 2009.

[50] F. Arleo and S. Peigne, "Heavy-quarkonium suppression in p-A collisions from parton energy loss in cold QCD matter," *JHEP*, vol. 03, p. 122, 2013.

[51] B. B. Abelev *et al.*, "Production of inclusive $\Upsilon(1S)$ and $\Upsilon(2S)$ in p-Pb collisions at $\sqrt{\mathbf{s}_{\mathrm{NN}}} = \mathbf{5.02}$ TeV," *Phys. Lett.*, vol. B740, pp. 105–117, 2015.

[52] R. Aaij *et al.*, "Study of Υ production and cold nuclear matter effects in pPb collisions at $\sqrt{s_{\mathrm{NN}}}$=5 TeV," *JHEP*, vol. 07, p. 094, 2014.

[53] M. Aaboud *et al.*, "Measurement of quarkonium production in proton–lead and proton–proton collisions at 5.02 TeV with the ATLAS detector," *Eur. Phys. J.*, vol. C78, no. 3, p. 171, 2018.

[54] R. Rapp and X. Du, "Theoretical Perspective on Quarkonia from SPS via RHIC to LHC," *Nucl. Phys.*, vol. A967, pp. 216–224, 2017.

[55] S. Chatrchyan *et al.*, "Observation of sequential Υ suppression in Pb-Pb collisions," *Phys. Rev. Lett.*, vol. 109, p. 222301, 2012.

[56] V. Khachatryan *et al.*, "Suppression of $\Upsilon(1S), \Upsilon(2S)$ and $\Upsilon(3S)$ production in PbPb collisions at $\sqrt{s_{\mathrm{NN}}}$ = 2.76 TeV," *Phys. Lett.*, vol. B770, pp. 357–379, 2017.

[57] G. Chikovani, V. Roinishvili, and V. Mikhailov, "Operation mechanism of the track spark chamber," vol. 29, pp. 261–269, 10 1964.

[58] R. Santonico and R. Cardarelli, "Development of Resistive Plate Counters," *Nucl. Instrum. Meth.*, vol. 187, pp. 377–380, 1981.

[59] M. Marchisone, "Performance of a resistive plate chamber equipped with a new prototype of amplified front-end electronics in the ALICE detector," *J. Phys. Conf. Ser.*, vol. 889, no. 1, p. 012011, 2017.

[60] P. Dupieux, "A new front-end for better performances of RPC in streamer mode," *Nucl. Instrum. Meth.*, vol. A508, pp. 185–188, 2003.

[61] R. Arnaldi *et al.*, "A low-resistivity RPC for the ALICE dimuon arm," *Nucl. Instrum. Meth.*, vol. A451, pp. 462–473, 2000.

[62] R. Arnaldi *et al.*, "Beam and ageing tests with a highly-saturated avalanche gas mixture for the ALICE p-p data taking," *Nucl. Phys. Proc. Suppl.*, vol. 158, pp. 149–153, 2006. [,149(2006)].

[63] C. Zampolli, F. Carminati, and A. Colla, "The shuttle : the alice framework for the extraction of the conditions data," 01 2010.

[64] K. A. Olive *et al.*, "Review of Particle Physics," *Chin. Phys.*, vol. C38, p. 090001, 2014.

[65] J. Adam *et al.*, "Centrality dependence of the charged-particle multiplicity density at midrapidity in Pb-Pb collisions at $\sqrt{s_{\rm NN}}$ = 5.02 TeV," *Phys. Rev. Lett.*, vol. 116, no. 22, p. 222302, 2016.

[66] K. Aamodt *et al.*, "Rapidity and transverse momentum dependence of inclusive J/ψ production in pp collisions at $\sqrt{s} = 7$ TeV," *Phys. Lett.*, vol. B704, p. 442, 2011.

[67] E. Abbas *et al.*, "Performance of the ALICE VZERO system," *JINST*, vol. 8, p. P10016, 2013.

[68] B. Abelev *et al.*, "Measurement of the Cross Section for Electromagnetic Dissociation with Neutron Emission in Pb-Pb Collisions at $\sqrt{s_{\rm NN}}$ = 2.76 TeV," *Phys. Rev. Lett.*, vol. 109, p. 252302, 2012.

[69] "Quarkonium signal extraction in ALICE," 2015. ALICE-PUBLIC-2015-006.

[70] C. Patrignani *et al.*, "Review of Particle Physics," *Chin. Phys.*, vol. C40, no. 10, p. 100001, 2016.

[71] D. Acosta *et al.*, "Υ production and polarization in $p\bar{p}$ collisions at $\sqrt{s} = 1.8$-TeV," *Phys. Rev. Lett.*, vol. 88, p. 161802, 2002.

[72] R. Aaij *et al.*, "Measurement of Υ production in pp collisions at $\sqrt{s}$ = 7 TeV," *Eur. Phys. J.*, vol. C72, p. 2025, 2012.

[73] V. Khachatryan *et al.*, "Upsilon Production Cross-Section in pp Collisions at $\sqrt{s} = 7$ TeV," *Phys. Rev.*, vol. D83, p. 112004, 2011.

[74] F. Bossu, Z. C. del Valle, A. de Falco, M. Gagliardi, S. Grigoryan, and G. Martinez Garcia, "Phenomenological interpolation of the inclusive J/ψ cross section to proton-proton collisions at 2.76 TeV and 5.5 TeV," 2011.

[75] V. M. Abazov *et al.*, "Measurement of the polarization of the Υ1S and Υ2S states in $p\bar{p}$ collisions at $\sqrt{s}$ = 1.96-TeV," *Phys. Rev. Lett.*, vol. 101, p. 182004, 2008.

[76] T. Aaltonen *et al.*, "Measurements of Angular Distributions of Muons From Υ Meson Decays in $p\bar{p}$ Collisions at $\sqrt{s} = 1.96$ TeV," *Phys. Rev. Lett.*, vol. 108, p. 151802, 2012.

[77] S. Chatrchyan *et al.*, "Measurement of the Υ(1S), Υ(2S) and Υ(3S) polarizations in pp collisions at $\sqrt{s} = 7$ TeV," *Phys. Rev. Lett.*, vol. 110, no. 8, p. 081802, 2013.

[78] B. B. Abelev *et al.*, "Measurement of quarkonium production at forward rapidity in pp collisions at $\sqrt{s} = 7$ TeV," *Eur. Phys. J.*, vol. C74, no. 8, p. 2974, 2014.

[79] J. Adam *et al.*, "Inclusive quarkonium production at forward rapidity in pp collisions at $\sqrt{s} = 8$ TeV," *Eur. Phys. J.*, vol. C76, no. 4, p. 184, 2016.

[80] R. Aaij *et al.*, "Measurement of Υ production in pp collisions at $\sqrt{s} = 2.76$ TeV," *Eur. Phys. J.*, vol. C74, no. 4, p. 2835, 2014.

[81] R. Aaij *et al.*, "Forward production of Υ mesons in pp collisions at $\sqrt{s} = 7$ and 8 TeV," *JHEP*, vol. 11, p. 103, 2015.

[82] S. Agostinelli *et al.*, "GEANT4 : A Simulation toolkit," *Nucl. Instrum. Meth.*, vol. A506, pp. 250–303, 2003.

[83] R. Brun, F. Bruyant, F. Carminati, S. Giani, M. Maire, A. McPherson, G. Patrick, and L. Urban, *GEANT : Detector Description and Simulation Tool; Oct 1994*. CERN Program Library, Geneva : CERN, 1993. Long Writeup W5013.

[84] B. Abelev *et al.*, "Centrality determination of pb-pb collisions at $\sqrt{s_{NN}} = 2.76$ tev with alice," *Phys. Rev. C*, vol. 88, p. 044909, Oct 2013.

[85] R. Aaij *et al.*, "Study of χ_b meson production in p p collisions at $\sqrt{s} = 7$ and 8 TeV and observation of the decay $\chi_b(3P) \to \Upsilon(3S)\gamma$," *Eur. Phys. J.*, vol. C74, no. 10, p. 3092, 2014.

[86] R. Aaij *et al.*, "Measurement of the $\chi_b(3P)$ mass and of the relative rate of $\chi_{b1}(1P)$ and $\chi_{b2}(1P)$ production," *JHEP*, vol. 10, p. 88, 2014.

[87] K. Tuchin, "Breakdown of kT-Factorization and J/ψ Production in dA Collisions," *Nucl. Phys.*, vol. A854, pp. 198–203, 2011.

[88] B. Abelev *et al.*, "Technical Design Report for the Upgrade of the ALICE Inner Tracking System," Tech. Rep. CERN-LHCC-2013-024. ALICE-TDR-017, Nov 2013.

[89] "Upgrade of the ALICE Time Projection Chamber," Tech. Rep. CERN-LHCC-2013-020. ALICE-TDR-016, Oct 2013.

[90] "Technical Design Report for the Muon Forward Tracker," Tech. Rep. CERN-LHCC-2015-001. ALICE-TDR-018, Jan 2015.

[91] P. Antonioli, A. Kluge, and W. Riegler, "Upgrade of the ALICE Readout Trigger System," Tech. Rep. CERN-LHCC-2013-019. ALICE-TDR-015, Sep 2013.

[92] B. Abelev *et al.*, "Upgrade of the alice experiment : Letter of intent," *Journal of Physics G : Nuclear and Particle Physics*, vol. 41, 08 2014.

[93] S. Acharya *et al.*, "J/ψ elliptic flow in Pb-Pb collisions at $\sqrt{s_{\mathrm{NN}}} = 5.02$ TeV," *Phys. Rev. Lett.*, vol. 119, no. 24, p. 242301, 2017.

[94] M. Al-Turany, P. Buncic, P. Hristov, T. Kollegger, C. Kouzinopoulos, A. Lebedev, V. Lindenstruth, A. Manafov, M. Richter, A. Rybalchenko, P. V. Vyvre, and N. Winckler, "Alfa : The new alice-fair software framework," *Journal of Physics : Conference Series*, vol. 664, no. 7, p. 072001, 2015.

[95] M. Al-Turany, D. Bertini, R. Karabowicz, D. Kresan, P. Malzacher, T. Stockmanns, and F. Uhlig, "The fairroot framework," *Journal of Physics : Conference Series*, vol. 396, no. 2, p. 022001, 2012.

[96] iMatix Corporation, *ZeroMQ*.

[97] G. Inc., *Google Protocol Buffer*.

[98] M. Richter and A. Collaboration, "Online data compression in the alice o 2 facility," *Journal of Physics : Conference Series*, vol. 898, no. 3, p. 032049, 2017.

[99] S. Acharya *et al.*, "Υ suppression at forward rapidity in Pb-Pb collisions at $\sqrt{s_{\mathrm{NN}}}$ = 5.02 TeV," 2018.

Acknowledgements

Questo lavoro è frutto di tre anni di grande crescita professionale e personale, ma sarebbe stato impossibile senza il supporto di tante persone.

Voglio ringraziare i miei genitori, per avermi ascoltato per ore, per avermi consigliato per altrettanto tempo e per avermi spronato quando le energie scarseggiavano. Li ringrazio per tutto quello che hanno sempre fatto.

Voglio ringraziare i miei amici e colleghi Ennio, Luca, Antonio, Mohammad, Guillaume, Stefano, Alessandro e Carlo per esserlo, e per tutto il resto. Ringrazio profondamente chi da molto più di tre anni ha ricambiato il mio profondo rispetto con altrettanta umanità e attenzione. Grazie a Ermanno e Mauro.

Je tiens à remercier de tout cœur le group du Subatech, qui m'a permis de faire face à la distance et aux défis continus avec la sérénité nécessaire. Vous m'avez appris ce que signifie faire équipe et j'essaierai d'apporter une partie de votre esprit dans toutes les équipes où je travaillerai.

Un ringraziamento particolare va a Giorgio(ne) perchè è stato capace di regalarmi un po' della sua forza, dandomi i migliori consigli che abbia mai ricevuto, permettendomi di misurarmi riguadagnando qualcosa che da anni non avevo più.

Diego e Martino sono le due persone più responsabili per i risultati che questo percorso ha portato. Li voglio ringraziare per l'enorme quantità di informazioni, spiegazioni, traning, dati, riferimenti e confronti che mi hanno offerto in questi tre anni. Grazie a Diego e Sara e Gines e Inma per tutte le cose che mi hanno offerto, cose senza nome di cui puoi percepire l'assenza stando lontano da casa.

Der letzte Wort meiner Doktorarbeit muss einer Person werder. Diese Person hatte die Kraft mich zu ertragen und zu unterstützen. Jetzt ist unsere Zeit gekommen und Ich kann's kaum erwarten es zusammen zu verbringen, Enrica !

UNIVERSITE BRETAGNE LOIRE / MATIERE MOLECULES ET MATERIAUX

UNIVERSITA DEGLI STUDI DI TORINO

IMT Atlantique
Bretagne-Pays de la Loire
École Mines-Télécom

Titre : Étude de la production de quarkonia pendant collisions nucléaires avec ALICE à LHC et optimization de l'algorithme de identification des muons

Mots clés : ALICE, LHC, Upsilon, muons, Pb-Pb, optimisation, algorithmes

ALICE est dédié à l'étude d'un état de la matière nucléaire dans lequel les quarks et les gluons ne sont plus confinés dans les hadrons, qui est appelé Quark Gluon Plasma (QGP). La production de bottomonia (états liés beauté anti-beauté) est sensible au QGP parce-que les états du bottomonium sont formés avant la formation du QGP et traversent le plasma pendant son évolution. L'objectif principal de cette thèse est la mesure des modification des mésons Upsilon dans le canal de désintégration en deux muons en collisions Pb-Pb à $\sqrt{s_{NN}} = 5.02$ TeV.

En outre, un nouveau framework pour l'analyse des performances des détecteurs utilisés pour l'identification des muons a été realisé et utilisé pour l'analyse des données du RUN1 et RUN2 du LHC. Enfin, et avec l'objectif d'optimiser des résultats de l'analyse, un nouvel algorithme d'identification de muons a été développé. Cet algorithme deviendra nécessaire pour faire face aux nouvelles conditions de prise de données du RUN3, pendant lequel une reconstitution quasi-en ligne du détecteur est prévue.

Title : Study of quarkonium production in ultra-relativistic nuclear collisions with ALICE at the LHC and optimization of the muon identification algorithm

Keywords : ALICE, LHC, Upsilon, muon, Pb-Pb, optimization, algorithm

ALICE is devoted to the study of a deconfined state of nuclear matter called Quark Gluon Plasma (QGP), in which quarks and gluons behave as free particles. The bottomonium (bound states of beauty-anti beauty quark) production is affected by the presence of the QGP, since bottomonium states are produced sooner than the QGP and witness the whole evolution of the plasma. In this analysis the data coming from Pb-Pb collisions have been analysed in order to detect possible modifications of the production rates in the dimuon decay channel, with respect to the rates observed in proton-proton collisions.

Furthermore, the performances of the detectors involved in the muon identification during the LHC RUN1 and RUN2 has been tested using a new analysis framework implemented as part of this thesis. Finally, in order to optimize the results of future analyses, a new muon identification algorithm has been developed and tested. This algorithm will become necessary in the LHC RUN3 running conditions, when the much higher luminosity will require a quasi-online reconstruction of data.